

On the Application of Rapid Prototyping Technology for the Fabrication of
Flapping Wings for Micro Air Vehicles

by

Kurtis Leigh Kraemer

A thesis submitted to the Faculty of Graduate and Postdoctoral
Affairs in partial fulfillment of the requirements
for the degree of

Master of Applied Science

in

Aerospace Engineering

Carleton University
Ottawa, Ontario

© 2012

Kurtis Leigh Kraemer



Library and Archives
Canada

Published Heritage
Branch

395 Wellington Street
Ottawa ON K1A 0N4
Canada

Bibliothèque et
Archives Canada

Direction du
Patrimoine de l'édition

395, rue Wellington
Ottawa ON K1A 0N4
Canada

Your file Votre référence

ISBN: 978-0-494-93623-8

Our file Notre référence

ISBN: 978-0-494-93623-8

NOTICE:

The author has granted a non-exclusive license allowing Library and Archives Canada to reproduce, publish, archive, preserve, conserve, communicate to the public by telecommunication or on the Internet, loan, distribute and sell theses worldwide, for commercial or non-commercial purposes, in microform, paper, electronic and/or any other formats.

The author retains copyright ownership and moral rights in this thesis. Neither the thesis nor substantial extracts from it may be printed or otherwise reproduced without the author's permission.

AVIS:

L'auteur a accordé une licence non exclusive permettant à la Bibliothèque et Archives Canada de reproduire, publier, archiver, sauvegarder, conserver, transmettre au public par télécommunication ou par l'Internet, prêter, distribuer et vendre des thèses partout dans le monde, à des fins commerciales ou autres, sur support microforme, papier, électronique et/ou autres formats.

L'auteur conserve la propriété du droit d'auteur et des droits moraux qui protègent cette thèse. Ni la thèse ni des extraits substantiels de celle-ci ne doivent être imprimés ou autrement reproduits sans son autorisation.

In compliance with the Canadian Privacy Act some supporting forms may have been removed from this thesis.

While these forms may be included in the document page count, their removal does not represent any loss of content from the thesis.

Conformément à la loi canadienne sur la protection de la vie privée, quelques formulaires secondaires ont été enlevés de cette thèse.

Bien que ces formulaires aient inclus dans la pagination, il n'y aura aucun contenu manquant.

Canada

Abstract

Micro air vehicles (MAV) are a class of small uninhabited aircraft with dimensions less than 15 cm (6 in) and mass less than 500g (1.1 lbs). The aim of this research was to develop a fast, accurate, low-cost, and repeatable fabrication process for flapping MAV wings. Through the use of the RepRap Mendel open-source fused-deposition modeling (FDM) rapid prototyping machine (“3-D printer”), various wing prototypes were designed and fabricated using a bio-inspired approach. Testing of the aerodynamic performance of both real locust wings and the 3-D printed wing prototypes was performed through axial spin testing. Bending stiffness measurements were also performed on the 3-D printed wings. Through the use of open-source rapid prototyping technology, a fast and low-cost fabrication process for flapping MAV wings has been developed, out of which further understanding of flapping wing design and fabrication has been gained.

Acknowledgements

This work would not have been possible without the guidance, support, and seemingly limitless patience of my thesis supervisor, Dr. Jeremy Laliberté. Jeremy, along with the many professors and colleagues I have been taught by and worked with throughout my education and my young engineering career have been instrumental in making me both the engineer and the person I am today, and will become in the future.

I must also acknowledge the open-source community around the world, whose self-less and innovative work is truly inspiring, and makes this technology accessible and affordable to the masses. In particular, I am thankful to the global RepRap users who have been willing to share their information and troubleshooting advice for the RepRap Mendel 3D printer.

I also want to thank my parents for their love and support throughout my University education. Last, and certainly not least, I want to thank Carmen for her love and patience; for motivating me and supporting me throughout this research; and for always being an inspiration to do great things.

This research has been funded by a Discovery Grant from the Natural Sciences and Engineering Research Council of Canada (NSERC).

Table of Contents

Abstract.....	ii
Acknowledgements	iii
Table of Contents.....	iv
List of Figures	viii
List of Tables	xiv
1 Introduction	1
1.1 Motivation.....	2
1.2 Outline	4
2 Micro Air Vehicles.....	6
2.1 Background	6
2.2 Fixed-wing MAVs.....	8
2.2.1 <i>Naval Research Laboratory MITE</i>	8
2.2.2 <i>Aerovironment</i>	8
2.2.3 <i>University of Florida</i>	9
2.2.4 <i>MLB Company</i>	11
2.3 Rotary wing MAVs	12
2.3.1 <i>Stanford University Mesicopter</i>	13
2.3.2 <i>Seiko Epson Micro Flying Robot</i>	13
2.3.3 <i>Prox Dynamics</i>	14
2.4 Flapping wing MAVs	17
2.4.1 <i>MicroBat</i>	18
2.4.2 <i>Tamkang University, Taiwan</i>	19
2.4.3 <i>Mentor MAV</i>	19
2.4.4 <i>Delfly</i>	20
2.4.5 <i>Muren Ornithopter</i>	21
2.4.6 <i>Entomopter</i>	22
2.4.7 <i>Harvard Microrobotic Fly</i>	23
2.4.8 <i>Aerovironment</i>	24
2.5 Summary	26

3	Insect Flight	28
3.1	Bio-inspiration.....	28
3.2	Flapping-wing flight.....	30
3.3	Birds versus insects	31
3.4	Aerodynamics of flapping.....	33
3.4.1	<i>Scaling and Reynolds number</i>	33
3.4.2	<i>Wing kinematics</i>	34
3.4.3	<i>Unsteady lift mechanisms</i>	37
3.4.4	<i>Dynamic stall</i>	39
3.4.5	<i>Other unsteady mechanisms</i>	39
4	Wing Design Considerations	41
4.1	Forces affecting deformation	41
4.2	Venation pattern	42
4.3	Locust wing morphology	44
4.4	Flexibility of wings.....	47
4.5	Surface roughness and corrugation.....	48
4.6	Applications to wing design.....	49
5	MAV Manufacturing.....	50
5.1	Wing manufacturing	51
5.2	Current methods	51
5.2.1	<i>Simple frame and membrane</i>	52
5.2.2	<i>MEMS Technologies</i>	54
5.2.3	<i>Rapid prototyping</i>	58
6	Rapid Prototyping Technology	61
6.1	Overview.....	63
6.2	Fused Deposition Modeling	64
6.3	Selective Laser Sintering	66
6.4	Stereolithography	68
6.5	3-Dimensional Printing	69
6.6	Inkjet-Based Printing	70
6.7	Jetted Photopolymer	70
6.8	Laser Engineered Net Shaping (LENS).....	71
6.9	Laminated Object Manufacturing.....	72

6.10	Process selection.....	73
7	Scope of Research	76
7.1	Literature review conclusions	76
7.2	Research Scope.....	77
8	RepRap Mendel.....	79
8.1	RepRap history	79
8.2	Specifications	80
8.3	Open-source technology	82
8.4	Principle of operation	84
8.5	Hardware.....	87
8.5.1	<i>Mechanical hardware</i>	88
8.5.2	<i>Electronic hardware</i>	89
8.6	Heated build platform	92
8.7	Software.....	94
8.7.1	<i>Computer-Aided Design (CAD) Software</i>	94
8.7.2	<i>G-code generator</i>	95
8.7.3	<i>Printer GUI</i>	99
8.7.4	<i>Printer firmware</i>	101
8.8	Printer setup	102
8.8.1	<i>Calibration</i>	102
8.8.2	<i>Test parts</i>	105
9	Prototype Wing Design and Manufacture	107
9.1	Fabrication process	107
9.2	Materials	109
9.2.1	<i>Veins</i>	109
9.2.2	<i>Membrane</i>	110
9.3	First wing prototypes	111
9.3.1	<i>PLA / PVDC</i>	113
9.3.2	<i>PLA/ PEEK</i>	114
9.3.3	<i>ABS / PVDC</i>	114
9.4	Simplified wing design	116
10	Wing Testing	119
10.1	Spin Testing	119

10.1.1	<i>Determination of Vertical Lift Coefficient</i>	120
10.1.2	<i>Experimental Set-up</i>	122
10.1.3	<i>Modifications to the test setup</i>	125
10.1.4	<i>Effect of rotational frequency</i>	127
10.1.5	<i>Error analysis</i>	129
10.1.6	<i>Locust wings</i>	132
10.1.7	<i>3D printed prototype wings</i>	138
10.1.8	<i>Scaled wings</i>	153
10.2	Stiffness distribution.....	154
10.3	Conclusions.....	160
11	Conclusions and Recommendations	162
11.1	Manufacturing process.....	163
11.1.1	<i>Overall process</i>	163
11.1.2	<i>Hardware</i>	165
11.1.3	<i>Materials</i>	166
11.1.4	<i>Alternative manufacturing processes</i>	167
11.2	Wing testing.....	167
11.3	Recommendations for further research.....	171
12	Contributions	172
	References	174

List of Figures

Figure 2-1. Black Widow MAV developed by Aerovironment, Inc.....	9
Figure 2-2. University of Florida MAV with flexible wings.....	10
Figure 2-3. Prioria Maveric small UAS.....	11
Figure 2-4. MLB Trochoid, 15cm version and Bat MAV, 60cm version.....	12
Figure 2-5. Stanford University Mesicopter.....	13
Figure 2-6. Seiko Epson's μ FR-II.....	14
Figure 2-7. Pixelito and Proxflyer Micron, both weighing 6.9 grams.....	15
Figure 2-8. Prox Dynamics' Nanoflyer, Picoflyer and Mosquito Twin-tail.....	16
Figure 2-9. Lithium-ion battery-powered Microbat with radio-control system.....	19
Figure 2-10. Mentor MAV with internal combustion engine.....	20
Figure 2-11. Delfly I and Delfly Micro.....	21
Figure 2-12. Muren's 1g ornithopter.....	22
Figure 2-13. Michelson's Entomopter MAV.....	23
Figure 2-14. Harvard's Microrobotic Fly, weighing just 60 mg.....	24
Figure 2-15. Aerovironment's Phase I demonstrator and Phase II Nano Hummingbird.....	26
Figure 3-1. African migratory locust, <i>locusta migratoria</i>	30
Figure 3-2. Size relationship between flapping (unsteady state regime) and soaring (steady state regime).....	33
Figure 3-3. Typical wing stroke cycle comprising of upstroke, pronation, downstroke, and supination.....	34

Figure 3-4. Wing tip path for a bumblebee in flight, showing the generated force vectors for the upstroke and downstroke	36
Figure 3-5. Illustration of the clap-fling mechanism. The wings clap together and the end of the upstroke and fling apart at the beginning of the downstroke, creating a vortex around the wing to generate additional lift	38
Figure 3-6. Increase in thrust-to-power ratio when using clap-fling.....	39
Figure 3-7. Unsteady lift mechanism during flapping flight	40
Figure 4-1. Insect wings show an evolutionary trend towards simple vein structures	43
Figure 4-2. Forewings and hindwings of the African migratory locust <i>Locusta migratoria</i>	44
Figure 4-3. The hind wing of a desert locust, showing scanning electron micrographs of the wing structure	45
Figure 4-4. Cross sectional view of a locust wing vein, which is more resistant to upward bending than downward bending	46
Figure 4-5. Illustration of wing deformation of the desert locust in flight.....	47
Figure 5-1. Fabrication of the Delfly's tail surfaces by gluing carbon fibre rods to Mylar film.....	52
Figure 5-2. Dragon fly-like wing fabricated by the University of Delaware.....	53
Figure 5-3. MEMS-based fabrication process used by Caltech	54
Figure 5-4. MEMS fabricates wings with silicon structure	55
Figure 5-5. MEMS fabricated wings with titanium structure	56
Figure 5-6. MEMS fabrication process using PVDF	57
Figure 5-7. Cornell University's 3-D printed flapping MAV	58

Figure 5-8. University of Southampton’s UAV fabricated using selective laser sintering	59
Figure 6-1. Anisotropy of material properties of parts produced using fused deposition modeling	62
Figure 6-2. Illustration of the fused deposition modeling process.....	65
Figure 6-3. Selective laser sintering set-up and process.....	67
Figure 6-4. Examples of parts fabricated using stereolithography.....	68
Figure 6-5. Illustration of the jetted photopolymer process used by Objet.....	71
Figure 8-1. Evolution of RepRap: Darwin, Mendel, Prusa Mendel, and Huxley.	80
Figure 8-2. RepRap Mendel 3D printer.....	85
Figure 8-3. Extruder assembly, showing exploded view, assembled view and cross section of filament drive system.	86
Figure 8-4. Cross section view of the extruder barrel.	86
Figure 8-5. Schematic of the RepRap's electronic hardware.	90
Figure 8-6. Simple wings designed using OpenSCAD.	95
Figure 8-7. Skeinforge screenshots, including the user interface, as well as 2-D and 3-D representations of the extruder tool paths.....	97
Figure 8-8. Tool paths of two layers deposited in sequence for a typical part, showing the border and infill pattern	98
Figure 8-9. Tool path for a wing with thin veins, showing two path lines for each vein in order to maintain a closed loop around the part.....	99
Figure 8-10. RepSnapper graphical user interface, showing a rendering of the G-code tool paths.....	100

Figure 8-11. Example test parts used for calibrating and optimizing printer settings.....	106
Figure 9-1. Wing fabrication process.	108
Figure 9-2. Printed prototype wing and rigid wing	112
Figure 9-3. Comparison of a real locust hind wing and a 3-D printed prototype wing...	112
Figure 9-4. Warped wing resulting from shrinkage of the ABS during cooling.....	115
Figure 9-5. OpenSCAD model and wing printed from ABS onto PVDC film	116
Figure 9-6. Wing prototypes based on simplified planform	117
Figure 10-1. Schematic of spin test set-up.....	124
Figure 10-2. Spin test set-up	124
Figure 10-3. Spinner with optoelectronic-switch for frequency measurement.....	125
Figure 10-4. Screenshot of oscilloscope showing frequency measurement	125
Figure 10-5. Variation in motor rotation frequency over time	127
Figure 10-6. Lift coefficient over a range of spin frequencies at constant angle of attack	128
Figure 10-7. Lift generated over a range of Reynolds numbers	129
Figure 10-8. Repeatability of experimental set-up.....	132
Figure 10-9. Comparison of locust A and locust B wing size	133
Figure 10-10. Wing tip damage to locust hind wing	133
Figure 10-11. Folded locust hind wing.....	134
Figure 10-12. Close up of folded hind wing with trailing edge highlighted	135
Figure 10-13. Lift generated by individual locust wings.....	136
Figure 10-14. Coefficient of vertical lift results for individual locust wings	136

Figure 10-15. Vertical lift coefficients for various wings tested by Usherwood & Ellington.....	137
Figure 10-16. Coefficient of vertical lift for locust wing pairs	138
Figure 10-17. Examples of 3-D printed wing prototypes tested, showing various vein angles	139
Figure 10-18. Comparison of peak vertical lift coefficient for each wing design	140
Figure 10-19. Comparison of single artificial wings versus real locust wings	141
Figure 10-20. Lift coefficient versus angle of attack for wing pairs with various vein configurations.....	141
Figure 10-21. Results for wings with veins at 10°	142
Figure 10-22. Results for wings with veins at 30°	143
Figure 10-23. Comparison of single vs pair of wings - no veins	144
Figure 10-24. Comparison of single vs pair of wings -10 degree vein	144
Figure 10-25. Comparison of single vs pair of wings -20 degree vein	145
Figure 10-26. Comparison of single vs pair of wings - 30 degree vein.....	145
Figure 10-27. Percent difference in lift between single and pair of wings	146
Figure 10-28. Vein clipped at wing root for increased flexibility.....	147
Figure 10-29. Effect of wing camber on wings with 30° vein angle.....	147
Figure 10-30. Effect of wing camber on wings with 20° vein angle.....	148
Figure 10-31. Effect of wing camber on wings with multiple veins	148
Figure 10-32. Wing with clipped wing vein, with trailing edge highlighted to show camber.....	149
Figure 10-33. Rough texture applied to wing membrane using cyanoacrylate	150

Figure 10-34. Corrugation in the locust hind wing	151
Figure 10-35. Effect of vein orientation and roughness - 30 degree vein	152
Figure 10-36. Effect of vein orientation and roughness - multiple veins	152
Figure 10-37. Effect of roughness on wing with no veins.....	152
Figure 10-38. Effect of surface roughness on lift performance at various Reynolds numbers.....	153
Figure 10-39. Lift coefficient values for insect-scale printed wings and real locust wings	154
Figure 10-40. Schematic of bending test setup	155
Figure 10-41. Relationship between spanwise and chordwise stiffness with wing span and chord length	157
Figure 10-42. Spanwise stiffness versus wing span for 3-D printed wing prototypes, showing trendline observed in nature.....	157
Figure 10-43. Chordwise stiffness versus chord length for 3-D printed wing prototypes, showing trendline observed in nature.....	158
Figure 10-44. Comparison of chordwise and spanwise stiffness for each wing design. .	159
Figure 10-45. Cross sectional view of a locust wing vein, which is more resistant to upward bending than downward bending	159
Figure 10-46. Comparison of upward and downward bending stiffness.....	160

List of Tables

Table 2-1. Summary of flapping-wing MAVs.....	27
Table 6-1 - Summary of Rapid Prototyping Processes.....	64
Table 8-1. RepRap Mendel specifications compared to commercial 3-D printers	82
Table 8-2. Example of G-code used by the RepRap printer	96
Table 9-1. Properties of materials used in prototype wings.....	111
Table 10-1. Locust wing dimensions.....	135
Table 10-2. Peak vertical lift coefficient values and stall angles for artificial wings with various vein configurations	140
Table 10-3. Spanwise and chordwise stiffness measurements	156

1 Introduction

Over the past century of manned aviation, numerous technical challenges have been overcome by engineers and scientists, including supersonic flight and space travel. Now, as autonomous unmanned aerial vehicles (UAVs) and uninhabited aircraft systems (UAS) play a growing role in a wide variety of missions, there are a host of new challenges to overcome. These challenges include integration into civil airspace, sense and avoid capabilities, miniaturization, and increased range and endurance. Nevertheless, UAVs have emerged as extremely useful tools for dull, dirty, and dangerous missions, particularly for surveillance and reconnaissance in hostile territories. Their relative low cost, long range and endurance capabilities as compared to manned aircraft have resulted in numerous UAV development programs around the world. According to the New York Times, the United States military operated approximately 7,000 unmanned aircraft in 2011, as compared to only 50 a decade earlier (Bumiller & Shanker, 2011), which highlights the rapid growth of the unmanned systems industry. Today, UAVs are being used or actively developed for a wide range of civilian applications such as search and rescue, infrastructure protection, forest fire monitoring, wildlife tracking, and geophysical surveys.

While the majority of fixed-wing UAVs have a wingspan greater than 1m (3.3 ft) and a gross takeoff weight (GTOW) of over 5kg (11 lbs) (Pines, 2006), a class of much smaller and lighter UAVs has also emerged. These aircraft, called Micro Air Vehicles (MAVs), have been defined as having no length dimension greater than 15 cm (6 inches) , having a gross takeoff weight less than 200g (7 oz) (Pines, 2006), and capable of operating at

flight speeds less than 15 m/s (34 mph) (Murphy, 2008). Intended to be low-cost and expendable, MAVs may carry various small payloads, such as optical, acoustic, chemical, or biological sensors, while operating with low visual and acoustic signatures. Furthermore, they are also very portable, allowing them to be easily transported into remote areas, or carried by individual soldiers for military applications.

While MAVs are well-suited for military operations such as intelligence, surveillance and reconnaissance, there are various potential civil applications for these micro aircraft. For example, a “swarm” of MAVs equipped with sensors could be released in order to map chemical or radiation levels in an area of interest such as around a nuclear reactor. These small, inconspicuous aircraft may be used for crowd control, disaster relief, police investigations, or unobtrusive wildlife monitoring. The small size of these vehicles could also allow them to fly within pipes, mines or into collapsed buildings. The major challenge, however, is how to design and build these aircraft with the necessary flight capabilities to accomplish such missions.

1.1 Motivation

The design of small fixed- and rotary-wing aircraft draws upon knowledge gained over the last century of flight; however, at the MAV scale, we find that the aerodynamic principles change significantly. The low Reynolds number unsteady air flows experienced by MAVs result in a loss of airfoil efficiency for conventional fixed-wing and rotary-wing aircraft. As nature demonstrates, flapping wings are able to take advantage of these aerodynamic effects by extracting energy from the unsteady flows. This major departure from “conventional” aerodynamics presents many new challenges for the design and fabrication of MAVs. Consequently, a great deal of research effort has

been applied to understanding the fundamental physics behind wing flapping; however, few researchers have concentrated on the manufacturing and production of small scale flapping wings that not only meet the aerodynamic and structural requirements for flapping wing flight, but can be made efficiently, quickly, and affordably.

As researchers attempt to push the limits of micro- and nano-scale aircraft, there exists a need to accelerate the rate of learning in order to more rapidly understand the underlying principles of flight at this scale, as well as to develop the necessary air vehicle technologies to advance the technology readiness level (TRL) of MAVs from mere laboratory demonstrations to real products. Researchers in the field of flapping wing MAVs would have much to gain from a process that allows them to quickly design and fabricate wings, and thus accelerate research in the field of flapping wing design. Furthermore, a process that would allow mass production with the ability to rapidly incorporate design improvements at low cost is essential to the feasibility of MAVs as useful tools. The research presented in this thesis aims to accelerate the evolution of MAV design by identifying and developing a manufacturing process that allows researchers, engineers, and scientists to gain a more thorough understanding of MAV-scale flight by producing component prototypes, such as wings, in a low-cost and repeatable manner. The primary focus of this work was to develop an integrated design and manufacturing process for prototype micro air vehicle wings. The secondary focus of this work was the application of this process to study the effects of wing features on lift performance. The results and findings of this research are given in this thesis, as well as recommendations for future work in this field.

1.2 Outline

In order to put this work into context, the past and present state-of-the-art in micro air vehicle technology is given in Chapter 2, including some examples of fixed-wing, rotary-wing, and flapping-wing MAVs that have been developed to date. The research presented in this thesis focuses on flapping-wing flight, to which a *bio-inspired* approach is taken; therefore, bio-inspiration and bio-mimicry as approaches to MAV design are described in Chapter 3, along with an overview of the principles of insect flight. Continuing on the bio-inspired philosophy, the structural morphology of insect wings is reviewed in Chapter 4, which highlights some of the major design and manufacturing considerations that can be learned from insects. Since the primary focus of this research is on manufacturing processes for flapping MAV wings, the various methods currently employed by researchers for the fabrication of flapping-wing prototypes are reviewed in Chapter 5. Next, several rapid prototyping technologies that show promise for the fabrication of MAV wings are presented and analyzed in Chapter 6. The conclusions of this literature review are summarized in Chapter 7, which also provides an outline of the scope of this research. A description of the RepRap rapid prototyping machine and how it was used in this research as a method for fabricating MAV wings is then described in Chapter 8, which includes a detailed description of the system, as well as the calibration and testing process. The development and fabrication of the prototype flapping wings using the RepRap 3-D printer is presented in Chapter 9, followed by a description of the aerodynamic and stiffness testing performed on the prototype wings in Chapter 10. This testing compared the performance and properties of the various prototype wing designs with real insects, such as the African migratory locust *Locusta migratoria*. Finally,

conclusions from this work and recommendations for future research in this field are given in Chapter 11, with the overall contributions made by this research presented in Chapter 12.

2 Micro Air Vehicles

Significant progress has been made in the field of micro air vehicles (MAVs) over the past 15 years, out of which has come a better understanding of the principles of flight at small scale. Various approaches have been taken in the design of MAVs, such as fixed-wing and rotary-wing designs based on traditional larger manned aircraft, as well as relatively new “bio-inspired” approaches using various configurations of flapping wings. While our knowledge of fixed- and rotary-wing aircraft design has developed over the past century, our understanding of flapping wing aerodynamics and MAV design is still relatively limited. This chapter discusses the past and present state-of-the-art in micro air vehicle design. While there are now many MAV research and development programs around the world, some examples that have made significant contributions to the field of MAV design are described here.

2.1 Background

The focus on micro air vehicles came after a 1992 study by the RAND Corporation for the United States Defense Advanced Research Projects Agency (DARPA) projected that it would be possible to have flying vehicles with a 1 cm (0.4 in) wingspan and 1g (0.035 oz) payload within 10 years. Later, in 1995, DARPA held a workshop for perceived MAV stakeholders, which led to the creation of a \$35M (USD) program to develop MAV systems and technologies (Michelson, 2004; Mueller, 2006). Since then, there have been many fixed, rotary, and flapping winged MAVs developed, many of them funded by DARPA. These will be discussed further in the subsequent sections.

In 2005, DARPA created its nano-air-vehicle (NAV) program, with the goal of developing air vehicles with a wingspan less than 15cm (6 inches) and a mass less than 20g (0.7oz) (Defense Advanced Research Projects Agency, 2011). The aim of this program was to advance the understanding of low Reynolds number flight, guidance and navigation in complex environments, and the design, manufacture, and packaging of small, lightweight, and efficient subsystems. This eventually led to the recent development of Aerovironment's Nano Hummingbird (Aerovironment Inc., 2011a), which will be described further in section 2.4.8.

In 2010, United States Air Force Research Laboratory (AFRL) Air Vehicles Directorate constructed an MAV test facility at Wright-Patterson Air Force Base, called the Micro Air Vehicle Integration & Application Research Institute (μ AVIARI) (Bumiller & Shanker, 2011; AFRL Air Vehicles Directorate, 2010). The facilities will be used in collaboration between AFRL and both industry and academia to develop and test MAV technologies. The facilities include four laboratories dedicated to unsteady aerodynamics, MAV fabrication, flapping wing bench testing, and indoor flight testing. The construction of such a facility demonstrates the United States military's long-term interest in the development and application of MAV technologies. Canada's military has also shown interest in developing micro and nano air vehicles through collaborative research projects between government agencies, such as Defence Research and Development Canada (DRDC) and the National Research Council Canada (NRC), as well as both academia and private companies (Lesage, *et al.*, 2008; Defence Research and Development Canada, 2009; Bilodeau & Wong, 2011).

2.2 Fixed-wing MAVs

The majority of early MAV designs had a fixed-wing configuration, most likely due to the familiarity of fixed-wing aircraft design which is based on knowledge developed over several decades. However, fixed-wing flight at low Reynolds numbers presented new challenges. As a result, these early MAVs have built a better understanding of low Reynolds number flight performance, as well as the development and application of small-scale motors, batteries, and electronic hardware. This section presents some examples of fixed-wing MAVs that have been developed.

2.2.1 Naval Research Laboratory MITE

Among the earliest MAV examples was the Micro Tactical Expendable (MITE) MAV (2001) developed by the United States Naval Research Laboratory (NRL) (Kellogg, et al., 2001). The MITE is a two-propeller, fixed-wing aircraft with a wingspan between 8 and 18 inches (20.3 and 75.7 cm), depending on version and payload, and has a flight endurance of over 20 minutes. It could be equipped with a small camera and is remotely controlled. The MITE program contributed to the understanding of low-Reynolds number flight, as well as the development of autopilot systems for MAVs.

2.2.2 Aerovironment

As part of DARPA's MAV program, the California-based company, Aerovironment Inc., was awarded a contract to develop a 15cm (6 in) span aircraft (Grasmeyer & Keennon, 2001). The result was the Black Widow MAV shown in Figure 2-1, a fixed wing aircraft with a 15 cm (6 in) wing span, capable of transmitting video up to 1.8km (1.1 miles), flying for 30 minutes, and weighing only 80g (2.8oz). Building upon the Black Widow design, Aerovironment developed the Wasp family of MAVs. The Wasp Block I had a

wing span of 33cm (13 in) and weighed 170g (6oz), which was further developed into the Block II version which won the United States Air Force Battlefield Air Targeting Micro Air Vehicle (BATMAV) contract. The Wasp Block II had a wingspan of 41 cm (16 in) and a weight to 275 grams (9.7oz) (Aerovironment Inc, 2011b). The latest version of the Wasp is Block III, with a wing span of 72 cm (28.3 in) and a weight of 430g (15oz) – which no longer fits within the MAV definition. Aerovironment also developed a hydrogen fuel cell powered MAV, called the Hornet. On March 21, 2003, it made the world’s first MAV flight powered entirely by a hydrogen fuel cell (Aerovironment Inc., 2011c).

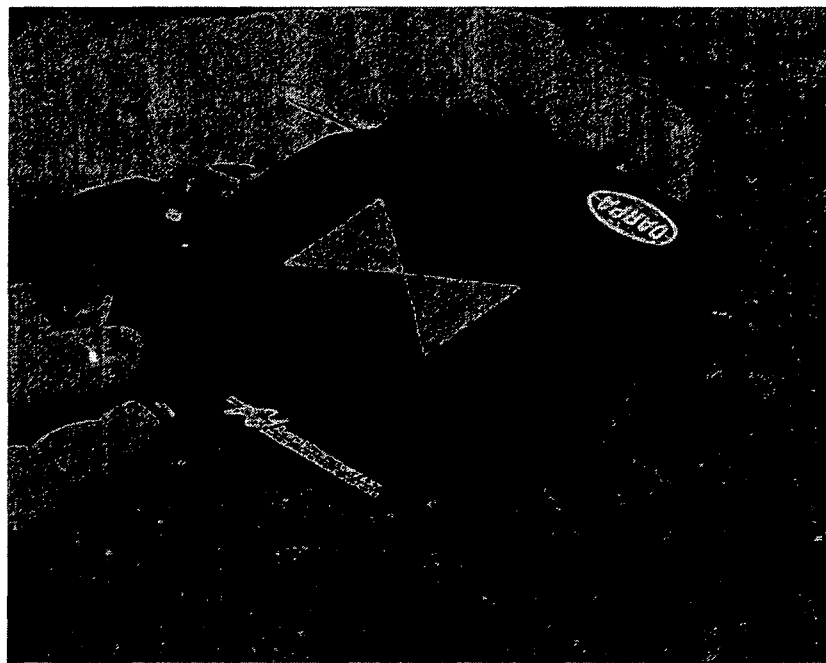


Figure 2-1. Black Widow MAV developed by Aerovironment, Inc. (Grasmeyer & Keennon, 2001)

2.2.3 University of Florida

Ifju *et al.* (2001, 2002) at the University of Florida developed a flexible-wing MAV with a wingspan of 6 inches (15 cm), a flying weight of up to 83g (2.9oz), and capable of flying up to five minutes. The thin, flexible, under-cambered wing is made up of a carbon

fibre composite leading edge (spar) and chordwise carbon fibre battens, with an extensible latex rubber membrane, as shown in Figure 2-2. The flexible membrane allows the wing to absorb energy from wind gusts and disturbances, providing increased flight stability and eliminating the need for gyro-assisted manually controlled flight. These MAVs also incorporated a vision-based stabilization system which detected the horizon for self-stabilization (Ettinger, Nechyba, Ifju, & Waszak, 2002). This design proved successful, with multiple winning entries at the International Micro Air Vehicle Competition. This flexible-wing design was also further developed into small unmanned aircraft system (sUAS), called the Prioria Maveric and shown in Figure 2-3, which was awarded a contract by the Canadian Forces under the ISTAR MUAV (intelligence, surveillance, target acquisition and reconnaissance miniature unmanned aerial vehicle) program for use in Afghanistan (Mortimer, 2010).

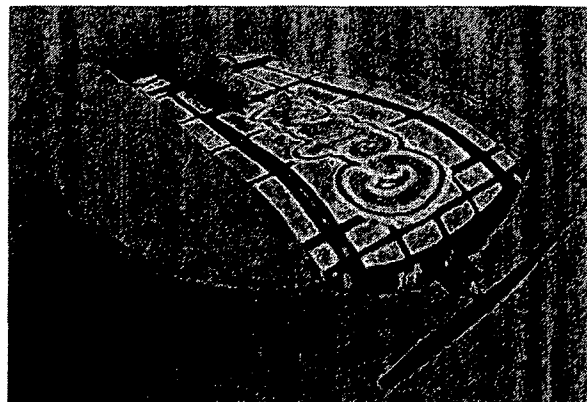


Figure 2-2. University of Florida MAV with flexible wings (Ifju, *et al.*, 2002)



Figure 2-3. Prioria Maveric small UAS (Prioria, 2011)

2.2.4 MLB Company

A series of MAVs were developed by Morris and Holden of the MLB Company (Morris & Holden, 2000), including an internal combustion engine (ICE) powered MAV called the Trochoid. While various wing-span and aspect ratio configurations were tested, the most successful was a 20 cm (7.9 in) version that demonstrated flight duration up to 20 minutes, with speeds from 10 to 60 mph (16 to 97 km/h). It could also be equipped with a video downlink and a stability augmentation system. Given the state of power sources and electronic hardware in the late 1990s, it was difficult for a 15-20 cm (6-8 in) aircraft to carry useful payload for any practical duration. Therefore, the Trochoid design was scaled-up, resulting in several Bat MAV versions ranging from 60 cm (24 in) to 1m (40 in) wingspan. Bat MAVs were tested in military exercises for the United States Marine Corps, and demonstrated autonomous flight and an inertial-stabilized camera system.

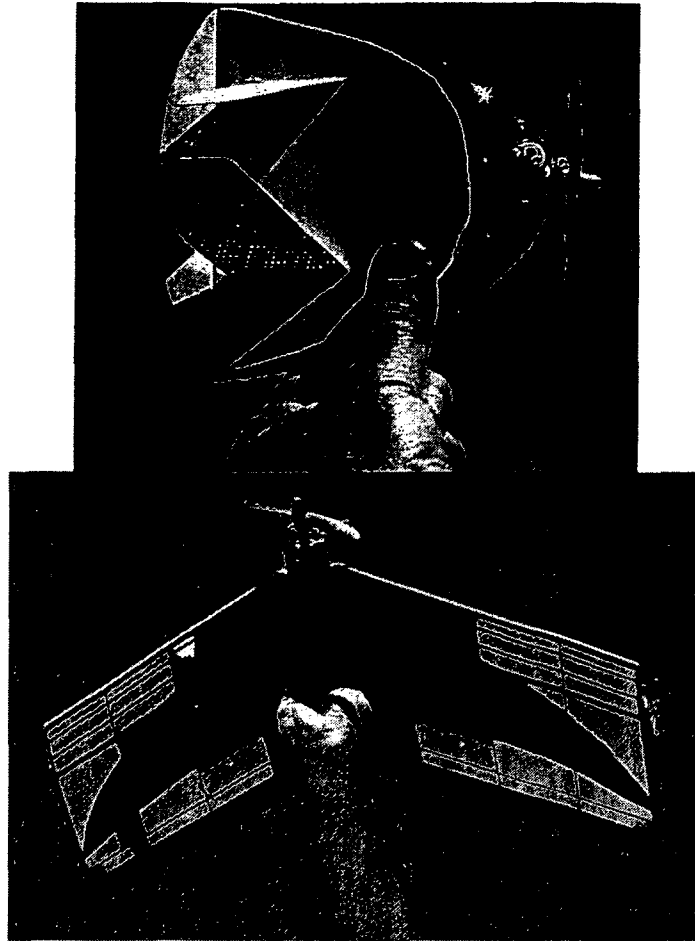


Figure 2-4. MLB Trochoid, 15cm version (left) and Bat MAV, 60cm version (right) (Morris & Holden, 2000)

2.3 Rotary wing MAVs

Despite their ability to hover and fly in small enclosed areas, few have focused on developing rotary-wing MAVs. The most likely reason is the relatively poor efficiency, and therefore endurance, of rotary-wing aircraft as compared to fixed-wing aircraft. This disadvantage is magnified at small scales, due to the unsteady low-Reynolds number aerodynamics as well as the limited available of lightweight power sources. Some of the MAV-scale rotorcraft that have been developed are described in this section.

2.3.1 Stanford University Mesicopter

Researchers at Stanford University, in collaboration with the National Aeronautics and Space Administration (NASA), performed a feasibility study in 1999 on a centimeter-scale aircraft, called the Mesicopter (Kroo & Prinz, 2009). The Mesicopter design featured four electric motors with 15 mm (0.6 in) diameter rotors, as shown in Figure 2-5, and was studied for both terrestrial and Mars exploration applications. This study focused on rotor design for ultra-low Reynolds numbers using 2-D and 3-D computation fluid dynamics (CFD), as well as manufacturing methods for small rotors and electric motors. The study resulted in the demonstration of tethered flight; however no free-flight results have been published.

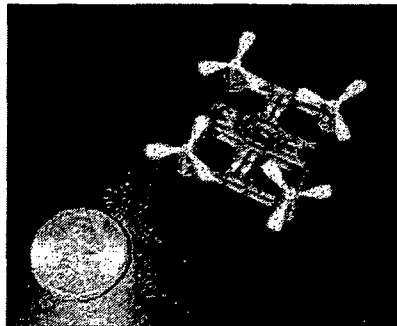


Figure 2-5. Stanford University Mesicopter (Kroo & Prinz, 2009)

2.3.2 Seiko Epson Micro Flying Robot

In 2003, Seiko Epson Corporation (Epson) unveiled the Micro Flying Robot (μ FR), which “featured two ultra-thin, ultrasonic motors driving two contra-rotating propellers for levitation, plus the world's first linear actuator stabilizing mechanism for attitude control during flight” (Advanced Model of World's Smallest Flying Microrobot from Epson, 2004). The μ FR was developed to demonstrate Epson's developments in micromechatronics. In 2004, Epson revealed the μ FR-II (Figure 2-6), a lighter and more

advanced version which included the world's smallest and lightest gyro sensor at the time, more powerful ultrasonic motors, and optimized rotors. The μ FR-II also featured an attitude control system, and an image sensor capable of capturing and wirelessly transmitting images via Bluetooth. The μ FR-II weighs 12.3g (0.43oz), has a rotor diameter of 136mm (5.35 in), and is capable of flight times up to 3 minutes.

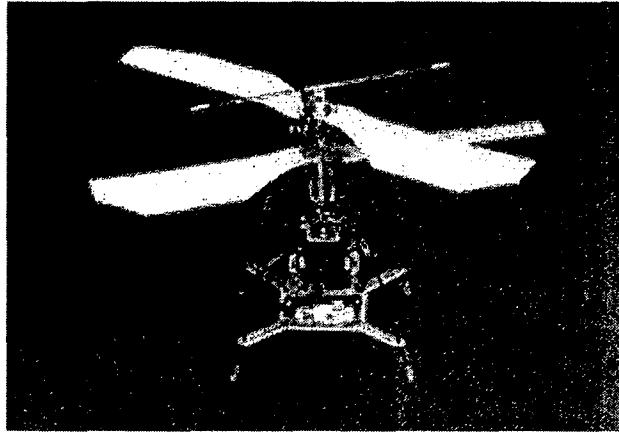


Figure 2-6. Seiko Epson's μ FR-II (Advanced Model of World's Smallest Flying Microrobot from Epson, 2004)

2.3.3 Prox Dynamics

Also in 2003, two prominent micro-scale radio-control (RC) helicopter designers Petter Muren and Alexander Van de Rostyne collaborated and challenged each other to build an RC helicopter weighing just 6.9g (0.24oz). The result was Van de Rostyne's Pixelito and Muren's Proxflyer Micro, both meeting the 6.9g (24oz) target (Muren, 2005; Van de Rostyne, 2003; Pixelito: Even Lighter Helicopter, 2004) (Figure 2-7).

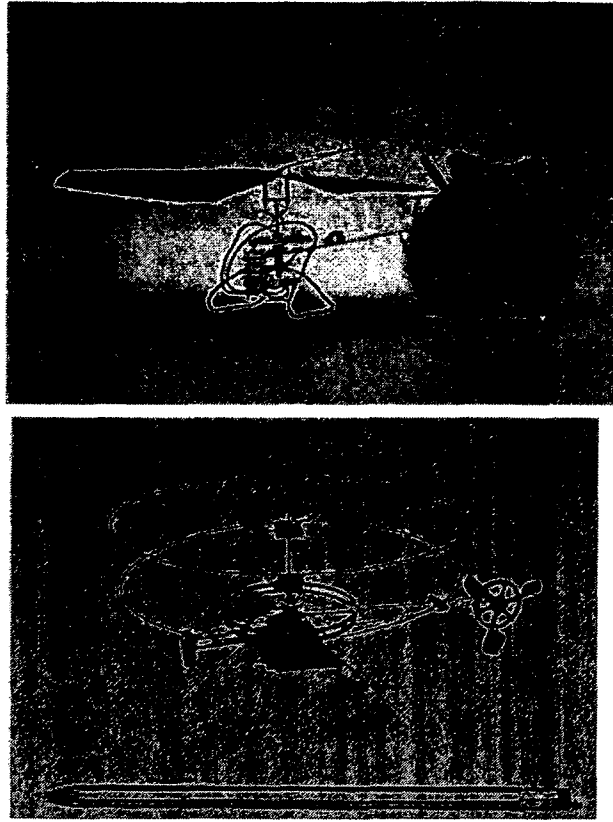


Figure 2-7. Pixelito (left) and Proxflyer Micron (right), both weighing 6.9 grams (Van de Rostyne, 2003)

Muren further developed the Proxflyer family of micro-scale radio-controlled rotary wing aircraft prototypes, ranging in weight from 2.7g (0.1oz) to 130g (4.6oz) (Muren, 2005). The smallest in terms of size is the Picoflyer, with a 60 mm (2.4 in) rotor diameter and a mass of 3.3g (0.12oz). It is, however, limited to a flight time of approximately one minute. The lightest aircraft is the Nanoflyer at 2.7g (0.1oz), which has 85 mm (3.3 in) diameter coaxial counter-rotating rotors. At 3.0g (0.1oz), the Nanoflyer II, has a larger battery and can fly for up to 10 minutes. The largest prototype is the Mosquito Twin-tail, with 36 cm (14.2 in) rotors and a weight of 130g (4.6oz). The Mosquito is capable of 4-channel control, including pitch, roll, yaw, and throttle. The Picoflyer and Nanoflyer, on the other hand, are limited to yaw and throttle control. Proxflyer helicopters are unique because they are passively stable, and therefore do not require additional gyroscopes or

other control system hardware. Furthermore, they employ three small electric motors, and have no servos, links, or other moving parts, resulting in a very lightweight and simple system. Each of the prototypes is a one-of-a-kind model, and is not offered for sale. However, Muren has patented its passive stabilization system, which has been incorporated into commercial radio-controlled (RC) helicopters by Interactive Toy Concepts (Muren, 2005), a toy company based in Toronto, Ontario.

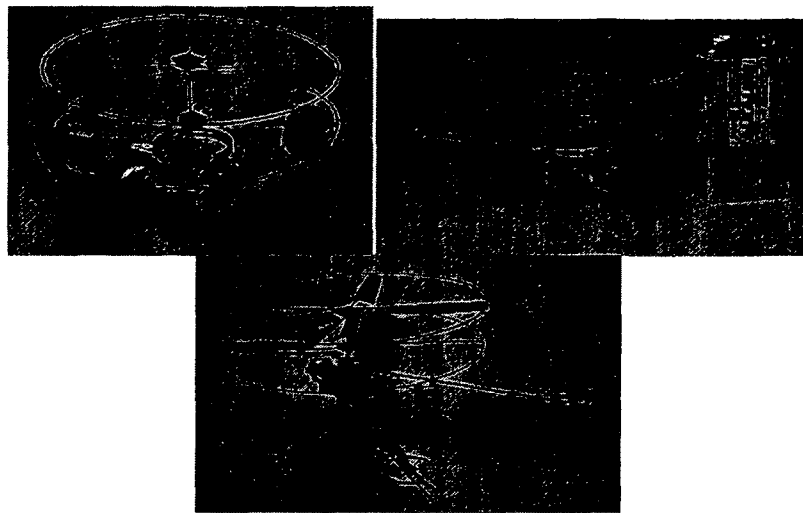


Figure 2-8. Prox Dynamics' Nanoflyer (left), Picoflyer (centre) and Mosquito Twin-tail (right) (Muren, 2005)

In 2006, Muren developed a radio-controlled helicopter weighing 0.9g (0.032oz), with a rotor diameter of 70 mm (2.8 in). It is considered to be the lightest radio-controlled helicopter in the world. Muren also developed a micro helicopter weighing 30g (1oz), equipped with RC control and video downlink. It had a flight time of 10 minutes.

Muren later founded Norway-based Prox Dynamics in 2007 (Prox Dynamics, Inc., 2009), which is developing the PD-100 Black Hornet system for military applications. The system is expected to include multiple aircraft equipped with data link, autopilot, and

video downlink, each weighing 15g (0.5oz) and having a rotor diameter of 120 mm (4.7 in).

2.4 Flapping wing MAVs

As the overall size of aircraft decreases, there has been a trend toward flapping aircraft, or “ornithopters”, rather than fixed- or rotary-wing aircraft. This is primarily due to the fact that a flapping wing is more aerodynamically efficient at generating lift and thrust than a fixed or rotating wing at the micro air vehicle (MAV) scale (see Chapter 3). The trend toward flapping aircraft has increased significantly in recent years as biologists and engineers alike have made significant advances in the understanding of flapping flight and its applications in aircraft design.

Humans have been trying to achieve flapping-winged flight since Leonardo Da Vinci studied this in the 15th Century; however, he never realized his dream of human-powered flight using flapping wings. It was not until 1870 that Gustav Trouvé would be the first to fly a flapping-winged aircraft to a distance of 70 metres (230 feet), powered by an internal combustion engine using gunpowder (Pornsirak, Tai, Ho, & Keennon, 2001). For decades, hobbyists have been fabricating and flying rubber-band powered ornithopters; however, the understanding of the physics of flapping flight, particularly at the MAV scale, as well as the availability of small, efficient power sources, actuation and control systems, and miniaturized electronics has been limited. Consequently, there has not yet been a flapping wing MAV with practical mission capabilities. This section describes some of the aircraft that have made significant contributions the design and development of flapping wing MAVs, and have brought us to the threshold of useful mission capabilities.

2.4.1 MicroBat

Pornsirirak *et al.* at the California Institute of Technology (Caltech) and the University of California, Los Angeles (UCLA), and in collaboration with Aerovironment, developed a flapping MAV called the Microbat (Pornsirirak, Tai, Nassef, & Ho, 2001; Pornsirirak, Tai, Ho, & Keennon, 2001). First flown in October 1998, it is reportedly the “first electrically powered palm-sized ornithopter”. The initial 15 cm (6 in) wingspan prototype, weighing 7.5g (0.26oz), was a free-flight model using a small electric motor powered by super-capacitors, achieving a maximum flight time of only 9 seconds. A second prototype used a rechargeable Nickel-Cadmium (Ni-Cad) battery, achieving flight duration of up to 22 seconds. An 8 in (20.3 cm) wingspan radio-controlled prototype was also developed, weighing 12.5g (0.44g), with the longest flight duration reaching 42 seconds. The radio-controlled (RC) Microbat used shape-memory-alloy (SMA) wire to actuate its tail control surfaces. In November, 2001, a Microbat equipped with a Lithium-ion battery (among the first commercially available types) and RC control achieved a new world record flight duration of 6 minutes 17 seconds (California Institute of Technology, 2001). This version weighed 11.5g (0.41oz). This research was the first to investigate micro-electro-mechanical-systems (MEMS) based manufacturing processes for the fabrication of MAV wings (to be discussed further in Chapter 5); however, the mass and stiffness of the MEMS wings were too high to be used on functional prototypes.

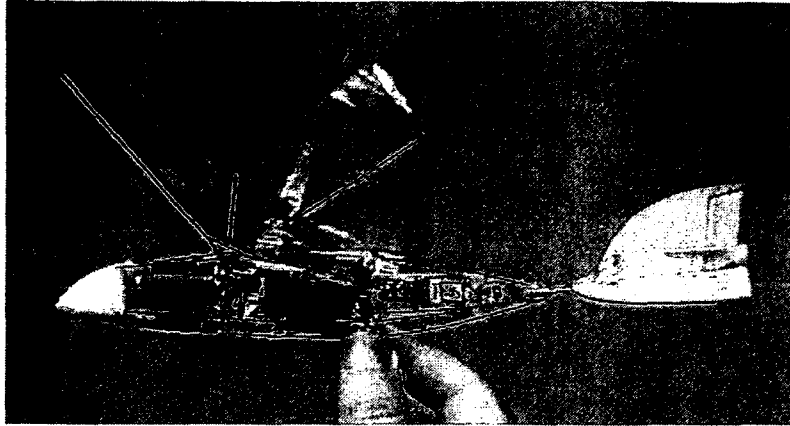


**Figure 2-9. Lithium-ion battery-powered Microbat with radio-control system
(California Institute of Technology, 2001)**

2.4.2 Tamkang University, Taiwan

Yang *et al.* at Tamkang University in Taiwan developed upon the Caltech Microbat design by integrating a piezoelectric polymer called poly-vinylidene-di-fluoride (PVDF) into the wings' membrane, allowing lift to be measured directly from the wings (Yang, 2007; Yang, Hsu, Ho, & Feng, 2007).

2.4.3 Mentor MAV

As part of DARPA's Micro Air Vehicle Program, the Mentor MAV was developed in 2002 through collaboration between SRI International and the University of Toronto Institute for Aerospace Studies (UTIAS) (Zdunich, *et al.*, 2007). The Mentor MAV was an internal combustion engine-powered ornithopter capable of both hovering and forward flight, as well as stabilized manual control. The Mentor demonstrated the advantages of the flapping wing aerodynamic phenomenon known as "clap-fling" to achieve lift and thrust for hovering.

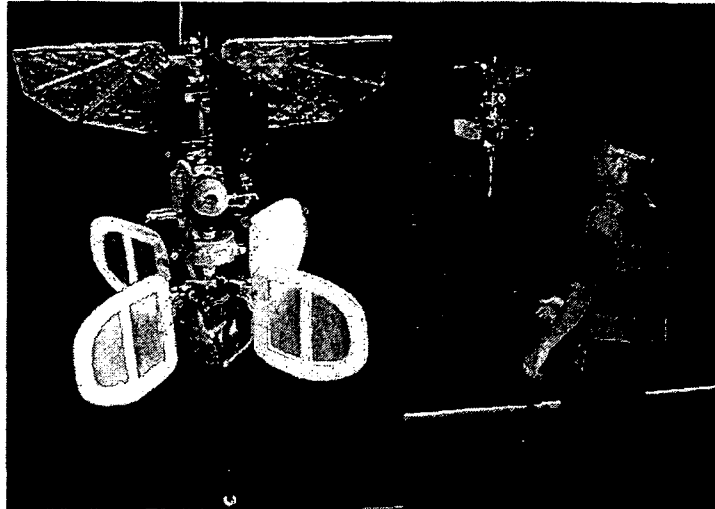


Figure 2-10. Mentor MAV with internal combustion engine (Zdunich, et al., 2007)

In addition to the University of Toronto's development of flapping wing MAVs, UTIAS has also developed both gasoline-powered and human-powered manned ornithopters (DeLaurier, 1999; hpo.ornithopter.net). This work has made UTIAS one of the leading universities in the world for flapping winged flight.

2.4.4 Delfly

In 2005, over a period of 10 weeks, a group of eleven third-year engineering students at Delft Technical University in the Netherlands designed a flapping wing MAV called Delfly (Mols, 2005; Lentink, Jongerius, & Bradshaw, 2009). Operated via radio control, the Delfly is 40 cm (15.7 in) long, has a 33 cm (13 in) wingspan, weighs between 15g (0.53oz) to 21g (0.74), and has flown for up to 17 minutes. It is also equipped with a miniature camera and is capable of transitioning between hovering and forward flight. The Delfly design was scaled down to a 28 cm (11 in) span ornithopter, called Delfly II (2006). Equipped with a video camera and weighing 16g (0.56oz), it can take off and land vertically, as well as hover for up to 8 minutes. Delfly Micro (van Dijk, 2008; Roos, 2011) was introduced a few years later in 2008. While similar in configuration to the

earlier Delfly, the Delfly Micro has a wingspan of 10 cm (3.9 in) and a mass of 3.07g (0.108oz). Also equipped with a miniature camera and radio control system, it has flown for 3 minutes at a speed of 5 m/s (11 mph). The Delfly project is investigating both the structural and aerodynamic aspects of flapping MAV flight (De Clercq, de Kat, Remes, van Oudheusden, & Bijl, 2009; Jongerius & Lentink, 2010), but also guidance, navigation and control for MAVs using optical methods (de Croon, de Weerd, de Wagter, & Remes, 2011; de Croon, de Clercq, Ruijsink, Remes, & de Wagter, 2009), demonstrating optical obstacle detection and avoidance via its onboard cameras.

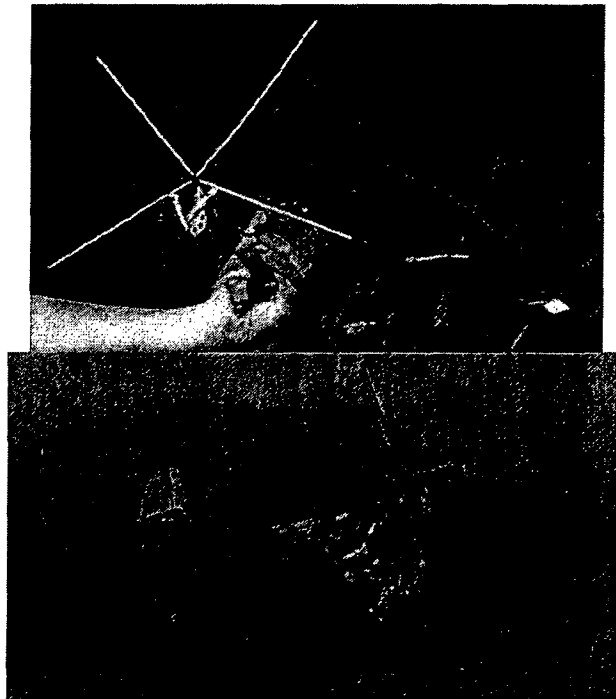


Figure 2-11. Delfly I (left) and Delfly Micro (right) (Roos)

2.4.5 Muren Ornithopter

In 2007, Petter Muren, who developed the Proxflyer micro-helicopters (section 2.3.3), built a radio-controlled ornithopter weighing 1.1g (0.04oz) (Prox Dynamics Inc., 2009). With a wingspan of 10 cm (3.9 in) and powered by a lithium polymer battery, it had a

flight endurance of less than 1 minute. It is believed to be the world's smallest radio-controlled ornithopter.



Figure 2-12. Muren's 1g ornithopter (Prox Dynamics, Inc., 2009)

2.4.6 Entomopter

The Entomopter, developed by Michelson at the Georgia Technology Research Institute (Michelson, 2004; Michelson & Naqvi, 2003), is a flapping MAV that uses a reciprocating chemical muscle (RCM) for power and actuation. The 15 cm (6 in) span aircraft weighs approximately 50g (1.8oz) (Astrobiology Magazine, 2009), and is capable of both flight and ambulatory locomotion. Its RCM propulsion system does not require an oxygen-rich environment; therefore, the entomopter is also being developed for Martian applications. The use of the RCM allows for electrical energy to be scavenged from the heat generated by the chemical process. Furthermore, the exhaust gases are used for flight control via circulation-controlled lift modification, by ejecting gases through channels in the wings. Acoustic obstacle detection and avoidance can also be achieved through modulation of the muscle waste gasses and wing motion.

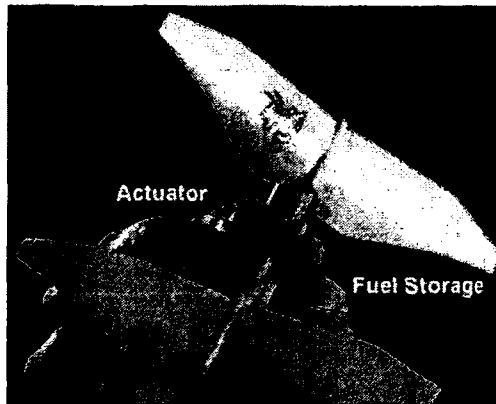


Figure 2-13. Michelson's Entomopter MAV (Astrobiology Magazine, 2009)

2.4.7 Harvard Microrobotic Fly

Wood, at Harvard University, has developed a small MAV prototype weighing only 60mg (0.002oz), with a wing span of approximately 40mm (1.57 in) and a flapping frequency of 120 Hz (Wood, 2008; Harvard University, 2011). This prototype is currently restricted to tethered flight using external power sources; however, the Microrobotic Fly has demonstrated a “meso-scale” fabrication method for fabricating wing structures, flexible joints, transmissions, and piezoelectric actuators. This process is described in further detail in Chapter 5. It has also allowed for the investigation of aerodynamics and wing design at true insect-scale.

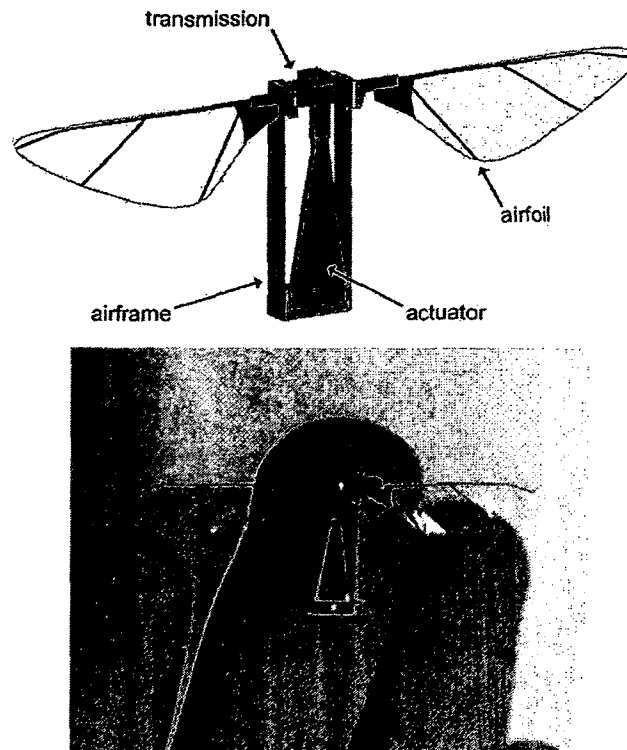


Figure 2-14. Harvard's Microrobotic Fly, weighing just 60 mg (Wood, 2008)

2.4.8 Aerovironment

Aerovironment was awarded a Phase I contract as part of the Defense Advanced Research Projects Agency (DARPA) Nano Air Vehicle (NAV) program to develop an aircraft less than 6 inches (15 cm), weighing less than 10g (0.35oz), and capable of flight speeds up to 10 m/s (22 mph) and withstanding 2.5 m/s (5.6 mph) wind gusts (Aerovironment, 2009; Defense Advanced Research Projects Agency, 2011). In 2009, Aerovironment demonstrated a hovering, two-winged flapping aircraft resembling a hummingbird, which was capable of vertical climb and descent, as well as flying forward, backward, and sideways via remote control.

As a result of its Phase I success, Aerovironment was awarded a contract for Phase II of the NAV program in 2009 to further develop this system by improving flight efficient

and endurance, demonstrating the capability to transition between hover and forward flight, and to integrate video downlink. In 2011, Aerovironment demonstrated its Nano Hummingbird, the first aircraft to meet the following milestones set by DARPA (Aerovironment Inc, 2011a):

1. Demonstrate precision hovering flight within a virtual 2m (6.6 ft) diameter sphere for one minute
2. Demonstrate hover stability in a wind gust flight which required the aircraft to hover and tolerate a 2 m/s (5 mph) wind gust from the side, without drifting downwind more than 1m (3.3 ft)
3. Demonstrate a continuous hover endurance of eight minutes with no external power source.
4. Fly and demonstrate controlled, transition flight from hover to 11 mph (5 m/s) fast forward flight and back to hover flight.
5. Demonstrate flying from outdoors to indoors, and back outdoors through a normal-size doorway.
6. Demonstrate flying indoors 'heads-down' where the pilot operates the aircraft only looking at the live video image stream from the aircraft, without looking at or hearing the aircraft directly.
7. Fly the aircraft in hover and fast forward flight with a bird-shaped body and bird-shaped wings.

The two-winged Nano Hummingbird has a flying weight of 19g (0.67oz) and a wingspan of 16 cm (6.5 in), similar in size and weight to a real hummingbird. The aircraft does not have any tail surfaces, using only its two wings for lift, thrust, and control.

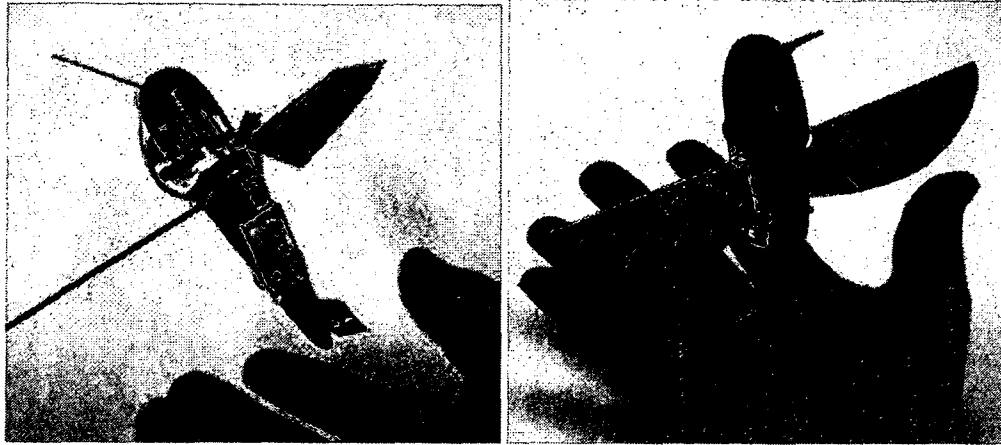


Figure 2-15. Aerovironment's Phase I demonstrator (left) (Aerovironment Inc., 2009) and Phase II Nano Hummingbird (right) (Aerovironment Inc., 2011a)

2.5 Summary

A summary of some flapping-wing MAVs is given in Table 2-1, which illustrates that current flapping and non-flapping MAVs do not yet have sufficient capabilities to perform useful missions. This progress is limited both by technological limitations in the size and weight of power sources and electronic hardware available, but also by our lack of a complete understanding of the principles of flight at this scale. However, it can be expected that technology will continue to miniaturize, which is primarily driven by the mobile electronics industry, while research such as that presented in this thesis will continue to advance our understanding of MAV design.

Table 2-1. Summary of flapping-wing MAVs

Design	Institution	Year	Weight (g)	Wingspan (cm)	# Wings	Untethered Hovering (s)	Features
Microbat	Caltech	2001	11.5	20.3	2	377	Radio controlled
Mentor	SRI, UTIAS	2002	580	36	4	> 60	Nitromethane (gas) powered
Entomopter	Georgia Tech	2003	50	15	4	-	Reciprocating chemical muscle
Delfly II	TU Delft	2006	16.07	28	4	480	On-board Camera, Radio controlled
Van Breugel	Cornell	2007	24.2	45	8	33	Passively Stable
Nathan Chronister	-	2007	3.3	15	4	Unknown	Radio controlled
Micromechanical Insect	Harvard	2007	0.06	3	2	N/A	Piezoelectric actuation, tethered flight
Petter Muren	-	2007	1.1	10	2	<60	Radio controlled
Delfly Micro	TU Delft	2008	3.07	10	4	240	On-board Camera, R/C
Nano Air Vehicle	Aerovironment	2009	10	7.5	2	20	Tailless, Active Wing Control
Golden Snitch	Tamkang	2009	7	20	4	N/A	Radio controlled
-	Cornell	2010	3.89	14.3	4	85	3D Printed Wings and Structure, passive flight
Nano Hummingbird	Aerovironment	2011	19	16	2	480	Radio controlled, stabilized, on-board camera, tailless

3 Insect Flight

Since wing design, material selection and ultimately fabrication process selection rely heavily on structural and aerodynamic requirements necessary for flight (i.e. shape, stiffness, deformation), an overview of the physics of flapping wing flight and the current knowledge of wing design is described in this chapter. A bio-inspired approach is taken in the design of the prototype wings, which is described in the following sections. While there is extensive literature describing the flight mechanics of various insect species, this chapter provides only a brief overview of the mechanics and aerodynamics of insect flight in order to derive potential design principles that may be applicable to micro air vehicles (MAVs). Specifically, the wing stroke pattern is described, as well as various unsteady aerodynamic mechanisms employed by insects to produce lift and thrust at low Reynolds numbers. The physical morphology of insect wings and their properties is given in the next chapter.

3.1 Bio-inspiration

In order to overcome the challenges of flight at small scales, many researchers have looked to birds and insects for inspiration, and for good reason, since all living creatures capable of powered (i.e. non-gliding) flight use flapping wings. However, it is important to distinguish biological inspiration (*bio-inspired*) from biological mimicry (*biomimetic*). A biomimetic design attempts to copy nature's solution, while a bio-inspired design may use the design space set out by nature, but will ultimately attempt to improve upon it. A classic example is the ground locomotion problem: Looking to nature suggests the use of hopping, sliding, slithering, or crawling. Experience tells us that a wheel is often the most

efficient design; however, we do not see wheeled creatures in nature (Michelson & Naqvi, 2003).

Biological solutions have benefited from millions of years of evolution, providing a good starting point for designers; however, biology has faced many constraints during evolution that designers do not necessarily face. Biological designs do not evolve towards a particular goal, but is determined based on random mutations which may, or may not, give the creature an advantage in a particular environment. Engineering design, however, is based upon specific mission requirements, such as speed, endurance, or manoeuvrability. The creature being studied may only be capable of slow forward flight and hovering, while the MAV may be required to have fast forward flight and not require hovering capabilities. These differences should be taken into account when using nature as inspiration for engineering designs.

The principles of insect flight investigated in this research are generally based on “normal” or “typical” insect flight, where many of the unique and highly adapted insect wings of some insect species are ignored. These unique designs include ornamentation used for courtship and mating displays, forewings which serve as protective shells, and the evolution of wings into sensory organs (Ellington, 1999).

By directly studying the geometric and structural properties of real insect wings, valuable insight can be gained into the design of artificial flapping wings. More specifically, the wings of the African migratory locust (*Locusta migratoria*), shown in Figure 3-1, are used in this research as a basis for comparison for geometric and aerodynamic properties. The locust is used as a model for several reasons: 1) it is a relatively large insect, and

therefore in many cases the wings and properties do not need to be scaled; 2) it is a well-mannered insect that does not bite or sting; 3) no animal care protocols are required for studying insects (as opposed to birds or bats); and 4) Carleton University's Department of Biology has a colony of live locusts available to study, as well as expertise in the principles of locust flight. Locusts have also been studied extensively in the literature, and were the first model for insect flight studies (Weis-Fogh, 1956, 1956a, 1964, 1973; Weis-Fogh & Jensen, 1956; Jensen, 1956; Jensen & Weis-Fogh, 1962; Wootton, Evans, Herbert, & Smith, 2000; Smith, Herbert, Wootton, & Evans, 2000; Herbert, Young, Smith, Wootton, & Evans, 2000). However, one disadvantage to studying locusts is that they are four-winged insects, which may not be the ideal configuration for MAV application due to the need for additional wings, linkages and actuation systems.



Figure 3-1. African migratory locust, *locusta migratoria* (Hornung, 2005)

3.2 Flapping-wing flight

At the MAV and insect scale, Reynolds numbers range from 100 – 10,000 (Ellington, 1999). In this range, conventional airfoil performance deteriorates due to the several effects: 1) lower lift coefficient, which means lower load carrying capability; 2) higher

drag coefficient, which means high motive power input; and 3) flow separation on the wing, which means stall at low angles of attack, thus reducing the wing's performance and manoeuvrability. Therefore, conventional fixed and rotary wings and propellers are less efficient for flight at the MAV scale (Pornsin-sirirak, Tai, Nassef, & Ho, 2001). Lift and thrust are achieved more efficiently through the use of unsteady lift mechanisms at the low Reynolds numbers experienced at the MAV scale. These mechanisms are described in section 3.4.

3.3 Birds versus insects

While all flying creatures use flapping wings, it is important to distinguish between the flapping flight of birds and bats from that of insects. In one of the more clear distinctions, birds and bats have muscles and articulated joints, allowing the shape of the wings to be actively controlled in flight; whereas insect wings are passive structures with no muscle or articulated joints, permitting minimal shape control in flight. However, the absence of active insect wing structures does not necessarily imply that insect-scale MAVs cannot benefit from actively controlled wings through the use of “smart” materials such as piezoelectric and electro-active materials as a means for flight control, sensing, and/or energy harvesting.

There is another major distinction between insects and other larger flying animals that relates to both size and aerodynamics. Micro air vehicles with a wingspan of 15cm (6 in) are on the border between two categories of flying creatures: (a) small flyers that are capable of hovering, but not soaring; and (b), larger flyers that are capable of soaring, but not hovering. Consequently, the way the flapping wings are used to achieve flight differs greatly between the two regimes. It should be noted that some animals, including insects,

employ a third mode of flight: gliding. Soaring uses air currents to provide additional lift, whereas gliding does not. It can be observed in nature that as the size and weight of a flying animal decreases, the more that animal produces lift from wing flapping than from soaring (Pornsin-sirirak, Tai, Nassef, & Ho, 2001). One can observe that large birds generally only flap their wings for thrust and manoeuvring, such as when taking off or flying into a headwind, while small birds, bats, and virtually all insects tend not to soar, but flap their wings almost continuously to produce both lift and thrust. One reason for this is that as size decreases, flapping wings are more efficient at generating lift than fixed wings (Pornsin-sirirak, Tai, Nassef, & Ho, 2001). As can be seen in Figure 3-2, MAVs fall within the unsteady-state regime where wing tip speed is greater than air speed and thus flapping becomes the primary flight mode. Flapping wings in this regime have an aerodynamic advantage over fixed and rotary wings because they benefit from unsteady, low Reynolds number flows ($<15,000$) experienced at this scale by extracting additional energy from the flow (Wang, 2005). These mechanisms are discussed in further detail in the following sections.

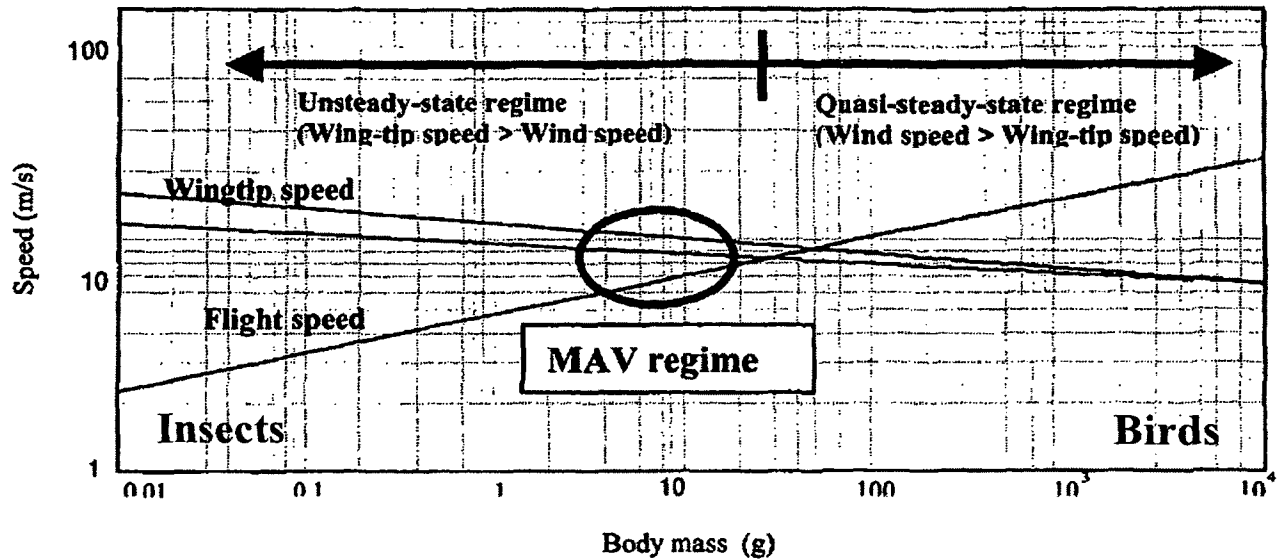


Figure 3-2. Size relationship between flapping (unsteady state regime) and soaring (steady state regime) (Pornsirirak, Tai, Nassef, & Ho, 2001)

3.4 Aerodynamics of flapping

This section presents the basic principles behind flapping wing flight, including the kinematics of wing flapping and a description of the various unsteady lift mechanisms that are employed by insects.

3.4.1 Scaling and Reynolds number

Despite the vast number of insect species, which range in weight from 20-30 μ g to 2-3g (0.07-0.1oz), insect wing geometries show a general trend (Ellington, 1999). On average, wing area is proportional to $m^{2/3}$ where m is the mass of the insect, while flapping frequency tends to be proportional to $m^{-1/4}$. Similar to large aircraft, the aerodynamics of flapping wings is dependent on the Reynolds number, Re , which is defined as the ratio between inertial forces and viscous forces in a fluid. For flapping flight, Reynolds number can be defined by:

$$Re = \frac{4\Phi nR^2}{\nu A_R} \quad (3.1)$$

where Φ is the wingbeat amplitude in radians, n is the wingbeat frequency, R is the wing length, ν is the fluid's dynamic viscosity, and A_R is the wing aspect ratio. For large insects, Re is generally between 5000 and 10,000, but can be as low as 10 for the smallest insects (Ellington, 1999).

3.4.2 Wing kinematics

A wing stroke consists of four distinct phases: two translation phases of the upstroke and downstroke, and two rotation phases called pronation and supination, which occur between each upstroke and downstroke (Pines, 2006). The wing stroke cycle is illustrated in Figure 3-3.

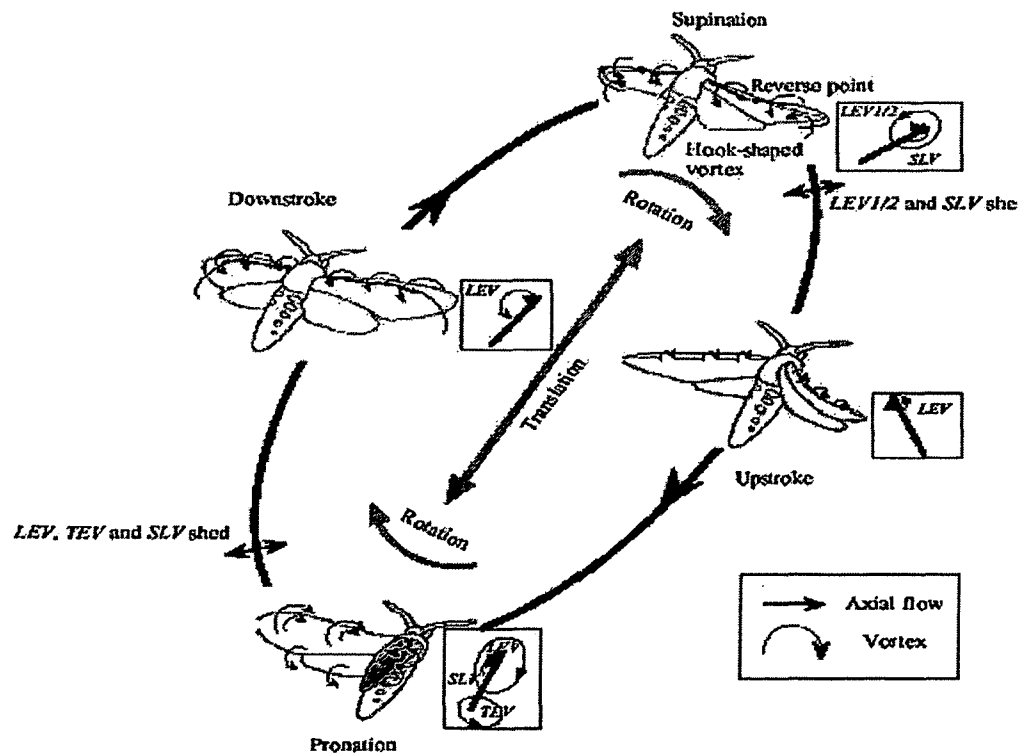


Figure 3-3. Typical wing stroke cycle comprising of upstroke, pronation, downstroke, and supination (Pines, 2006)

As mentioned above, both the size and corresponding Reynolds numbers vary greatly among insects, and the specific manner in which different species fly can also vary. However, the study of a wide range of insects has shown that wing motion follows a general pattern that can provide insight into what can be considered “normal” flapping flight for the purposes of MAV design (Ellington, 1999).

A method for characterizing and comparing insect flight is through a dimensionless measure of speed called the advance ratio, J . The advance ratio is the ratio between flight velocity and the flapping velocity, or:

$$J = \frac{V}{\phi n R} \quad (3.2)$$

where V is the flight velocity. For a hovering insect, $J=0$; while for a bumblebee in fast forward flight, $J=0.6$ (Ellington, 1999). The wing tip path for an insect in flight is shown in Figure 3-4. In hover, the stroke plane is horizontal, with the upstroke and down stroke being symmetric, which provides lift but no thrust. Between each stroke, the wing rotates (pronates and supinates) through 120° and the wing’s anatomical upper surface becomes the aerodynamic lower surface during the upstroke.

As the insect transitions to forward flight, the body tilts forward and the advance ratio increases. Similar to a helicopter, the stroke plane tilts forward with the body and the wing downstroke generates nearly all of the lifting force and some of the thrust, while the upstroke generates only thrust (Ellington, 1999). At maximum speed, the downstroke angle is such that a nearly net vertical force is generated, while the upstroke angle becomes nearly vertical.

As the insect flight speed changes, the body tilts forward until it is nearly horizontal at top speed, presumably to reduce drag. In general, flapping frequency remains relatively constant, however the wingbeat amplitude, ϕ , decreases with speed.

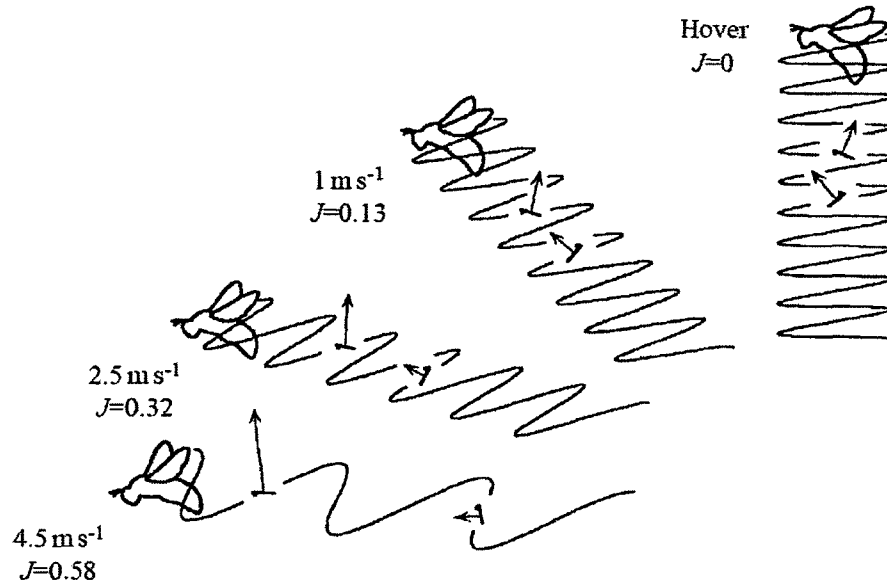


Figure 3-4. Wing tip path for a bumblebee in flight, showing the generated force vectors for the upstroke and downstroke (Ellington, 1999)

During hovering and slow flight, the insect's low centre of mass provides passive pendulum stability. Control is achieved primarily by tilting the stroke plane much like a helicopter (Ellington, 1999). Additional roll control is achieved by increasing the flapping frequency and/or the angle of attack of the outside wing, while pitch is achieved by shifting the centre of lift fore or aft. Finally, yaw has been shown to be achieved through the insect "paddling" on one side, where a high angle of attack on one wing creates excessive drag; however, locusts have been shown to use their abdomen as a rudder in flight (Ellington, 1999).

3.4.3 Unsteady lift mechanisms

Aerodynamic studies of insect flight using the conventional theories of aerodynamics, such as blade-element theory with steady flows, have shown that insects cannot fly without some additional unsteady high-lift mechanism (Ellington, 1999). Some of the unsteady mechanisms known to be employed by flying insects are described here.

3.4.3.1 Clap - fling

Upon studying tiny insects, Weis-Fogh (1973) observed that the wing motions were similar to the wing motion of larger insects, the left and right wings “clapped” together at the end of the upstroke, and “fling” apart during the start of the downstroke. As the wings fling open, an air vortex around the wing is generated by the inflow of air into the space between the wings. This increases air velocity over the top surface of the wing, thus generating lift. This clap-fling mechanism, illustrated in Figure 3-5, has been observed in small insects, as well as butterflies and moths in order to produce as much as 25% more lift than with the typical wing motions described previously (Ellington, 1999).

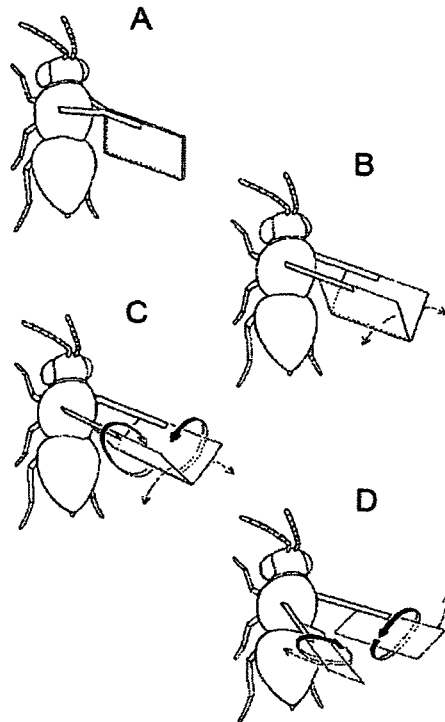


Figure 3-5. Illustration of the clap-fling mechanism. The wings clap together and the end of the upstroke (A) and fling apart at the beginning of the downstroke (B), creating a vortex (C and D) around the wing to generate additional lift (Ellington, 1999)

This approach has been employed in several flapping MAV design, such as the Mentor (Zdunich, et al., 2007) and Delfly (Roos; Lentink, Jongerius, & Bradshaw, 2009) MAVs. Studies by Zdunich *et al.* (2007) showed that wings employing clap-fling showed as high as a 35% increase in thrust-to-power ratio, as shown in Figure 3-6; however, the clapping action of the wings results in significant wear and damage on the wings. Alternatively, the same net increase in lift could be achieved through larger wings or increased flapping frequency (Ellington, 1999).

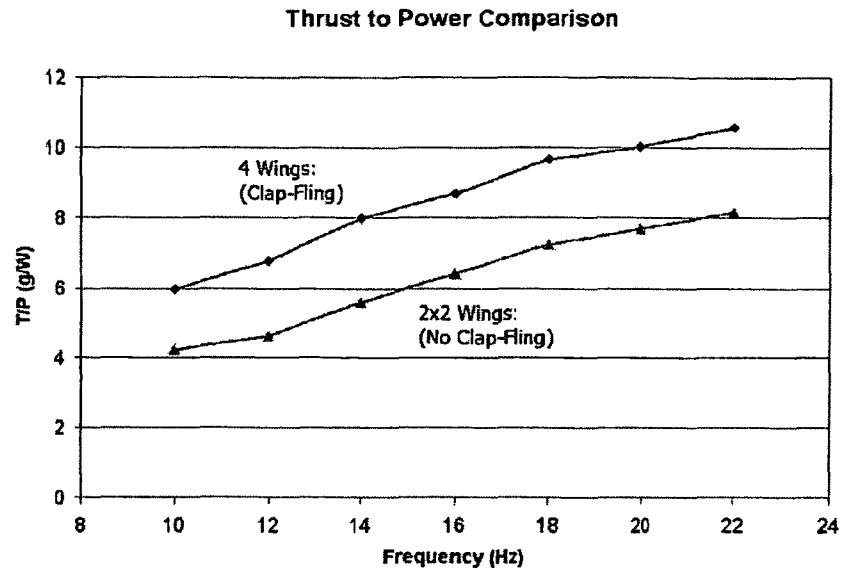


Figure 3-6. Increase in thrust-to-power ratio when using clap-fling (Zdunich, et al., 2007)

3.4.4 Dynamic stall

While clap-fling has been shown to provide increased lift, it is not widely used in nature (Ellington, 1999). Another high lift mechanism called *dynamic stall* is employed by most insects, where the wing can produce extra lift and high angles of attack before stalling. A leading edge vortex (LEV) is created during the downstroke, initiated by air swirling around the wing's leading edge, enhancing lift. The LEV occurs primarily on thin wings with sharp leading edges at high angles of attack (Ellington, 1999). This additional lift can be sustained for the entire downstroke if the LEV interacts with a spanwise flow, as shown for the hawkmoth *Manduca sexta* (Ellington, 1999), which creates a spiral leading edge vortex that remains attached and prolongs the lift benefit.

3.4.5 Other unsteady mechanisms

While delayed stall can explain the lift generation required to support the insect's weight beyond that predicted by conventional aerodynamic theory, it does not provide an explanation for the high lift forces generated by insects that can exceed twice their body

weight (Pines, 2006). Illustrated in Figure 3-7, other unsteady lift mechanisms, such as rotational circulation, wake capture, and bound circulation, are proposed (Pines, 2006); however, these mechanisms and how forces are generated in flight are not yet fully understood. Nevertheless, insight into the unsteady aerodynamics of flapping flight has been gained in order to better understand the requirements for flapping MAV design.

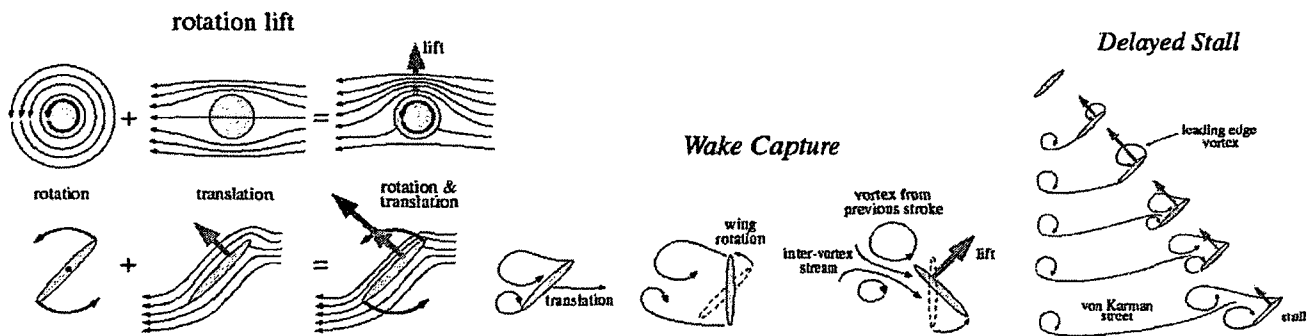


Figure 3-7. Unsteady lift mechanism during flapping flight (Pines, 2006)

An understanding of the aerodynamics of flapping wing flight is essential for the design and optimization of flapping wings for MAVs; however, the wing structure plays an equally important role in flapping-wing flight. An overview of insect wing structures and considerations for MAV wing design are given in the next chapter.

4 Wing Design Considerations

While designers and engineers have learned a great deal about designing relatively rigid wings, rotor blades, and propellers for traditional aircraft, many of these principles do not directly apply to flapping wings given both the unsteady aerodynamics and highly dynamic conditions associated with flapping flight at the micro air vehicle (MAV) scale. The design of flapping wings stands to benefit a great deal from a bio-inspired approach as described in the previous chapter since flapping wings are so prevalent in nature; however, insect wings are also complex and highly optimized structures. Their complicated motion and deformation during flight combined with the complex aerodynamics described in chapter 3 makes modeling and analysis of the wing structure challenging. Therefore, the morphology and structural features of insects are described in this chapter, as well as a description of some of the major wing design considerations derived from insect wings, so that these principles may be applied to the design of flapping MAV wings.

4.1 Forces affecting deformation

Flapping wings do not only experience aerodynamic loads, but they also must withstand the inertial-elastic loads due to the flapping motion. Since the wings are passive structures, their deformation in flight is entirely dependent upon these aerodynamic and inertial loads. The complex interaction between fluid and inertial forces makes modeling of flapping MAV wings challenging, and thus makes the design of wings with the required aeroelastic properties difficult. However, a study by Combes and Daniel (2003) tested the wings of the hawkmoth *Manduca sexta* in both air and helium using a robotic

flapping mechanism. Despite an 85% reduction in fluid density between the air and helium, the wing deformation patterns showed only slight changes. This suggests that wing deformation, at least in some insects, is governed primarily by inertial forces rather than fluid forces. This allows for a decoupling of inertial and fluid forces in wing design and modeling, allowing for an inertial-elastic model rather than an aeroelastic model, and thus simplifying the wing design process.

4.2 Venation pattern

Wing venation patterns differ greatly among insect species, however Figure 4-1 shows that “older” insect species have more complex vein patterns with a large number of cross veins, while more recently evolved species have simpler vein patterns with fewer cross veins (Combes & Daniel, 2003). One reason for this may be that insects have evolved to achieve the same wing properties, such as stiffness distribution, more efficiently by using fewer veins. This suggests that complex vein patterns are not strictly necessary for flapping MAV wings, provided the necessary overall structural properties can be achieved. However, all wings have stiff leading edges, usually comprised of multiple longitudinal veins, with additional veins radiating from the wing root to the edges.

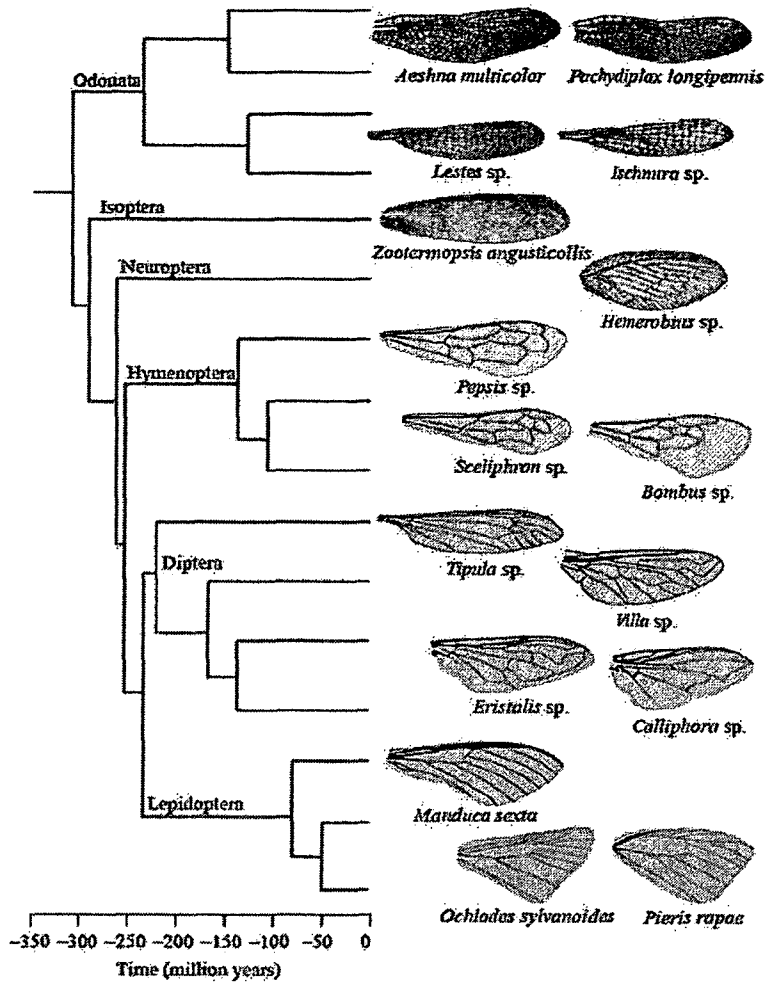


Figure 4-1. Insect wings show an evolutionary trend towards simple vein structures (not to scale) (Combes & Daniel, 2003)

Early insect species also tend to have two pairs of wings, with a pair each of forewings and hindwings, as seen in dragonflies and locusts (Ellington, 1999). However, most modern insects employ only a single pair of wings for flight, with the other wings evolving to serve alternate functions such as protective shells in beetles, or small protrusions called *halteres* in flies which are used as sensory organs. Alternatively, the two pairs of wings can be joined together to act as a single pair of wings as seen in butterflies and moths.

4.3 Locust wing morphology

As discussed in Chapter 3, this research uses the wings of the African migratory locust (*Locusta migratoria*), since locust species have been studied extensively and provides a good basis for comparing the properties and performance of fabricated MAV wings (Weis-Fogh, 1956, 1956a, 1964, 1973; Weis-Fogh & Jensen, 1956; Jensen, 1956; Jensen & Weis-Fogh, 1962; Wootton, Evans, Herbert, & Smith, 2000; Smith, Herbert, Wootton, & Evans, 2000; Herbert, Young, Smith, Wootton, & Evans, 2000). This section presents the morphology of the locust wing, with details on the wing vein structure and properties. In particular, the locust hind wing is the focus of this research, since it has been thoroughly studied in the literature. The forewings and hindwings of an African migratory locust are shown in Figure 4-2.

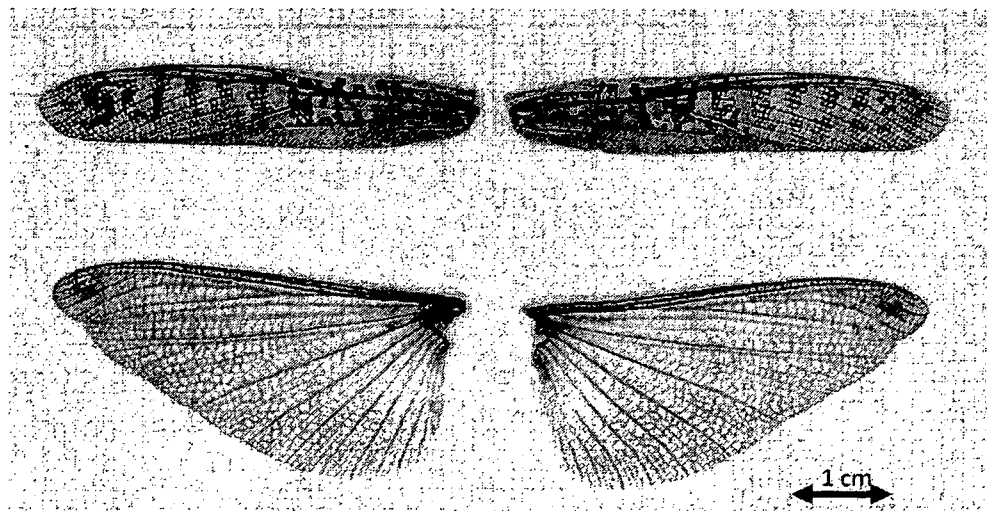


Figure 4-2. Forewings (top) and hindwings (bottom) of the African migratory locust *Locusta migratoria*

A thorough investigation of the wing morphology of the desert locust *Schistocerca gregaria* is given by Wootton *et al.* (2000). The locust hind wings have a corrugated structure with many cross veins, as shown in Figure 4-3. The wings also have a broad

“vannus” which is supported by many veins radiating from the base. The wing corrugation is formed by ridges and furrows created by alternating veins, providing spanwise rigidity to the wing, while enabling chordwise flexibility.

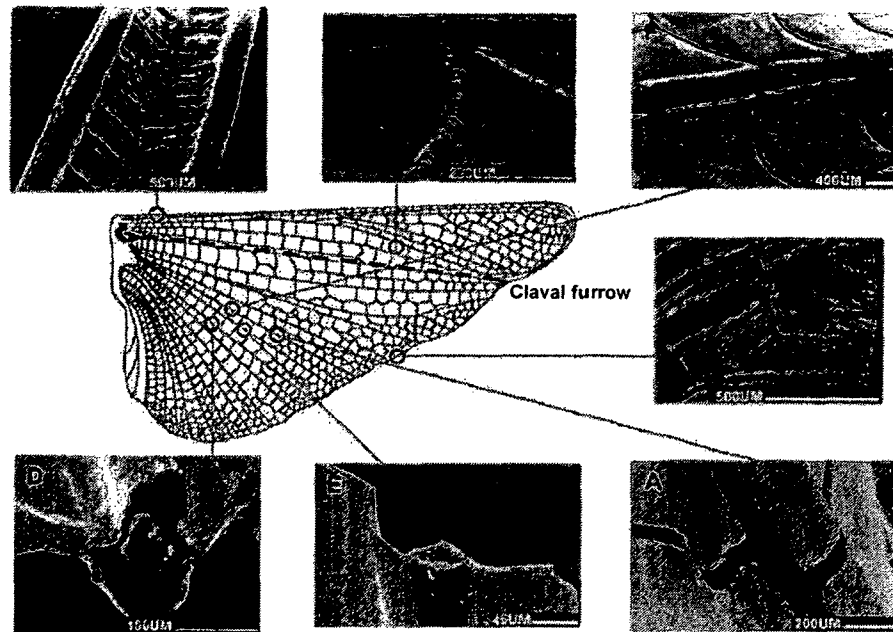


Figure 4-3. The hind wing of a desert locust, showing scanning electron micrographs of the wing structure (Wootton, Evans, Herbert, & Smith, 2000)

The hind wing has two areas, the remigium and the vannus, which are divided by a flexion line present in most insect wings called the claval furrow, shown in Figure 4-3. The remigium is the area of the wing anterior to the claval furrow, which is deeply corrugated near the base, forming a leading edge spar consisting of three veins in a V-shape. Posterior to the claval furrow is the vannus, a fan-like structure comprised of radiating veins and fold lines. These fold lines allow the wing to fold up at rest. In contrast, the locust forewing is slender and consists primarily of the remigium. As shown in Figure 4-4, some of the wing veins have a cross section that is more resistant to upward bending, as experienced in the downstroke, than downward bending.

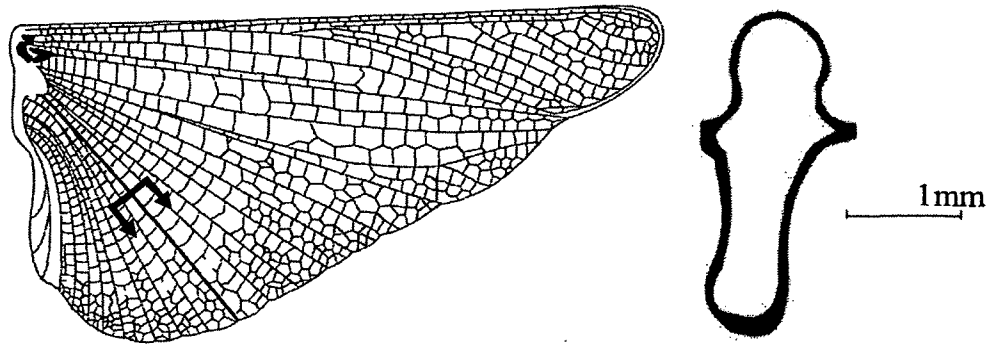


Figure 4-4. Cross sectional view of a locust wing vein, which is more resistant to upward bending than downward bending (Herbert, Young, Smith, Wootton, & Evans, 2000)

The wing deformations experienced by the locust hind wing in flight are illustrated in Figure 4-5. The wings perform a “near clap and fling” (Figure 4-5-F), as described in chapter 3. During the peeling action, the vannus flexes into a shape similar to the surface of a cone, with the expansion of the vannus resulting in no corrugation. This deformation is referred to as “radial flexion”, where the vannus expands along its radial flexion lines. During the downstroke (Figure 4-5-A), the wing develops a cambered shape, called the “umbrella effect”. The umbrella effect occurs due to the shape, orientation, and properties of the vannal veins, which induce curvature naturally as the wing is extended, providing camber to the wing and thus increasing lift. In (Figure 4-5-B,C), the wing retracts and flattens at the onset of the wing upstroke.

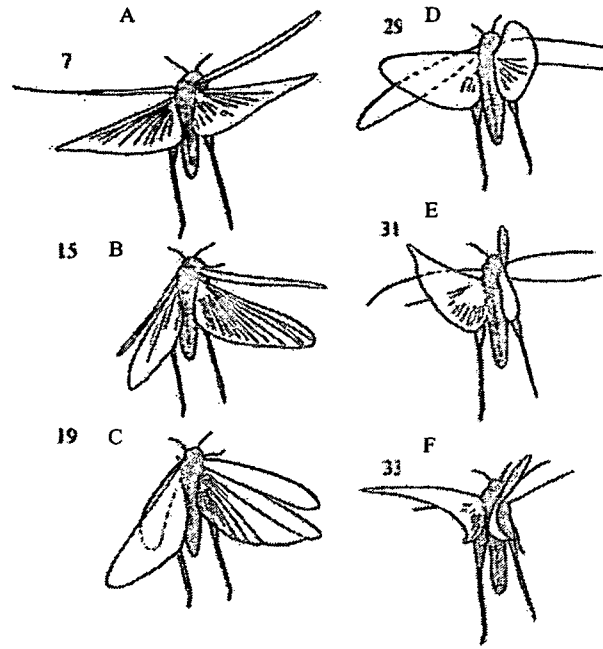


Figure 4-5. Illustration of wing deformation of the desert locust in flight (Herbert, Young, Smith, Wootton, & Evans, 2000)

4.4 Flexibility of wings

Combes and Daniel (2003b) studied the relationship between venation pattern and wing flexibility in 16 insect species. The results showed that wing size accounts for 95% of the variability of wing stiffness, where spanwise stiffness varies with the cube of wing span, while chordwise stiffness scales with the square of chord length. Their study also showed that spanwise stiffness is 1-2 orders of magnitude larger than the chordwise flexural stiffness.

The effect of spanwise flexibility of a rectangular wing in pure heave (vertical motion of the entire wing up and down) oscillations was studied by Heathcote *et al.* (2008). The results showed that a spanwise flexible wing produced a higher thrust coefficient and had higher efficiency than a rigid wing when oscillated in heave at one end. A highly flexible wing, however, performed poorly since there was a large phase lag in wing tip

displacement, resulting in the wing root and tip moving in the opposite directions out of phase. Furthermore, in the development of flapping wings for the Mentor MAV, Zdunich *et al.* (2007) found that manipulation of wing stiffness had a far greater effect on wing performance than by manipulation of wing planform geometry. In addition to the advantages in thrust and efficiency, a flexible wing is also inherently lighter than a stiff wing as is often observed for conventional fixed wing aircraft (e.g. flexible sailplane wing versus rigid transport aircraft wing).

4.5 Surface roughness and corrugation

Many insects, such as locusts, dragonflies, and damselflies, have “corrugated” wing airfoil shapes rather than smooth airfoils as seen on aircraft. The belief is that, in the low Reynolds number regime in which insects fly, corrugations act to “trip” the boundary layer, causing a transition from laminar to turbulent flow. This energizes the boundary layer, allowing it to remain attached and thus delaying stall or flow separation (Murphy, 2008). Under the same principle, the surface of a golf ball is dimpled to delay separation, reduce drag and travel farther.

A study by Murphy (2008) compared the performance of a flat plate airfoil, a corrugated airfoil modeled after a dragonfly wing, and a smooth airfoil with the same characteristics as the dragonfly airfoil, such as chord and thickness. Results showed that the corrugated airfoil stalled at a higher angle of attack than the smooth and flat plate airfoils at Reynolds numbers below 1×10^5 (i.e. the MAV range). The corrugated airfoil also produced 30% more lift than the other airfoils due to the delayed stall angle; however the drag was also much higher. At higher Reynolds numbers, however, the performance of the corrugated airfoil was worse than the smooth and flat plate airfoils. Murphy

recommended investigating airfoils that are corrugated on the top and smooth on the bottom in order to reduce drag at lower angles of attack, while maintaining the attached boundary layer to delay stall.

4.6 Applications to wing design

By examining nature's flying creatures, it can be concluded that flapping flight is a complex balance of unsteady aerodynamics and highly tailored structures. Furthermore, the types of aerodynamic mechanisms and the design of wings can differ among phylum, size, species, and survival requirements. However, nature presents some general trends that can provide insight into the design requirements for MAV design, such as stroke pattern, anisotropy between spanwise and chordwise stiffness, relations between stiffness and wing size, flexibility requirements, and the potential need for surface roughness for improved aerodynamic efficiency.

5 MAV Manufacturing

While the understanding of the aerodynamics of flapping wings remains one of the major challenges facing MAV designers, there are a number of additional challenges to overcome before flapping wing MAVs, and even other more conventional MAVs, see widespread use. These include:

- i) Wing actuation and articulation
- ii) Guidance, navigation, control and communications
- iii) Onboard power sources
- iv) Payload integration
- v) Wing design and manufacture

Each of these points is a major obstacle primarily due to the need for very small, lightweight, efficient, and multifunctional components. Much of the technology required to achieve useful flight control and endurance at this scale simply has not been developed yet, such as lightweight power sources with sufficiently high power densities, and sufficiently small electronic payload and control system hardware. Despite the great deal of research effort to understand flapping wing aerodynamics, control and actuation, there has been little focus on enabling low cost manufacturing of lightweight MAV structural components, particularly the wings.

The focus of this research is to overcome these wing design and manufacturing challenges. The aim is to gain a better understanding of the physical requirements necessary for efficient flapping flight, such as wing geometry and structural properties.

However, achievable properties are highly dependent upon the materials and manufacturing process; therefore, it is necessary to consider manufacturing processes concurrently with wing structural design.

5.1 Wing manufacturing

As shown in Chapter 4, the design of flapping wings is complex, requiring specific tailoring of stiffness and flexibility to achieve the required deformations for efficient lift generation. There exists a need for a process that allows custom wings to be designed and fabricated quickly and easily at low cost. There are two approaches that may be taken: a “small-batch” process that allows for parametric changes to small quantities of parts for research purposes; or, a “mass-production” process for the production of repeatable, high quality parts at low cost. As each approach has different requirements, there may not be a process that suits both. Given the state of flapping wing MAV technology, it would be more beneficial to the research community to have an optimized “small-batch” fabrication process that would allow designers to make parametric design changes efficiently and precisely, and was therefore the focus of this research. This section reviews the fabrication methods currently being used by researchers to develop their flapping MAV prototypes, with particular attention paid to wing fabrication.

5.2 Current methods

Several approaches have been taken to fabricate flapping wings for MAVs, with varied success. This section investigates some of these approaches and highlights the advantages and disadvantages of each.

5.2.1 Simple frame and membrane

Many researchers have taken a simple approach to fabricating wings for their flapping wing MAVs, which usually consist of carbon fibre rods as wing frames and a thin film as a membrane. The Delfly family of MAVs (Mols, 2005), developed at Delft Technical University in the Netherlands, all have relatively simple wing structures. The wings of the first generation aircraft, Delfly I, have carbon fibre reinforced balsa spars glued to a thin mylar film, while the tailplanes are made from carbon fibre rods and mylar film. The wings flap at approximately 6 Hz. The wings and tailplanes are fabricated by hand, requiring a great deal of time, labour, and skill. Furthermore, this method does not allow for precise and repeatable wing structures.

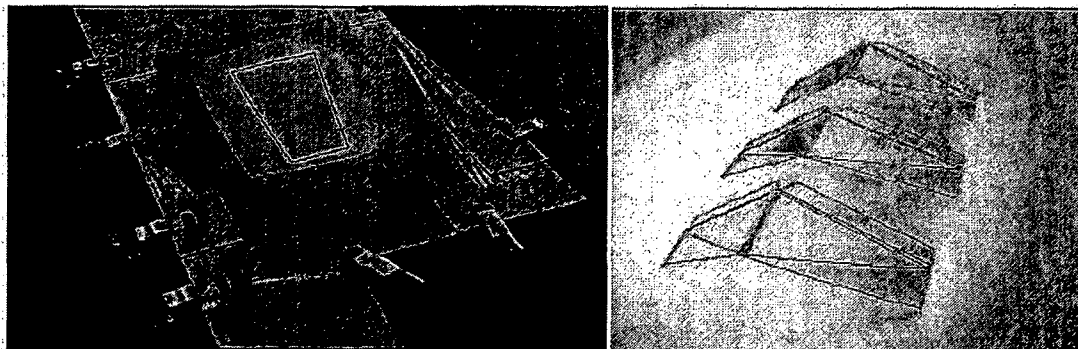


Figure 5-1. Fabrication of the Delfly's tail surfaces by gluing carbon fibre rods to Mylar film (Mols, 2005)

Delfly Micro, with a wingspan of 10 cm (3.9 in) and weight of 3.07g (0.11oz), uses carbon fibre rods and polyethylene terephthalate polyester (PET) film for its wings and tailplane. Its wings flap at approximately 30 Hz (van Dijk, 2008). Experimental bio-inspired wing designs were also fabricated by stretching dry carbon fibers on a three-dimensional mould and manually applying a cyano-acrylate matrix using a pin (Lentink, Jongerius, & Bradshaw, 2009).

Researchers at the University of Delaware took a similar approach to wing fabrication for their four-winged, dragonfly-like MAV (DiLeo & Deng, 2009). Carbon fibre rods, tubes and beams were used for the wing frame, and a 0.075 mm (0.003 in) thick polyester film was glued on for the membrane. They also employed rods made from Garolite, a glass fibre reinforced phenolic, as wing spars and wing pin attachment joints. The completed wing was 158.75 mm (6.25 in) long and weighed approximately 1.5g (0.05oz).

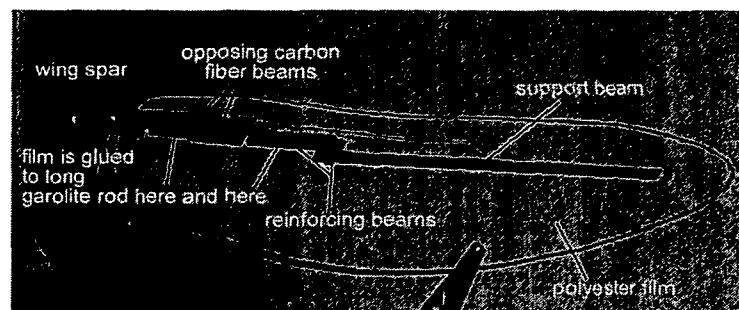


Figure 5-2. Dragon fly-like wing fabricated by the University of Delaware (DiLeo & Deng, 2009)

Researchers at the Caltech Institute of Technology (Caltech) fabricated their MicroBat MAV's wings using 750 μm (0.030 in) diameter carbon fibre rods glued to thin mylar film (Pornsin-sirirak, Tai, Nassef, & Ho, 2001). However, they found that the method had several disadvantages. Despite a simple wing structure, the method was cumbersome, and it was difficult to achieve identical sets of wings without the use of a mould. Furthermore, the glue added weight, making the wings too heavy. Consequently, this method is costly, time consuming, and has a slow turn-around time, which does not allow for efficient and effective study of design variable changes.

Manually fabricating wings for the purposes of parametric studies is not practical because the process is very labour intensive and time consuming. It is also difficult to achieve

accurate or repeatable results. Therefore, this method was not considered as a feasible process for the purposes of this research.

5.2.2 MEMS Technologies

Micro-electro-mechanical systems (MEMS) technologies have been employed at Caltech to fabricate flapping wings for a 15-cm wingspan MAV (Pornsir-sirirak, Tai, Nassef, & Ho, 2001; Pornsin-Sirirak, Tai, Ho, & Keennon, 2001). Unlike the manual fabrication method described in the previous section, MEMS technology provides repeatability, size control, weight minimization, mass production, and the ability to fabricate complicated structures. The first Caltech wings used silicon for the wing frames and poly-monochloropara-xylylene, or parylene-C, for the wing membrane. The process is shown in Figure 5-3.

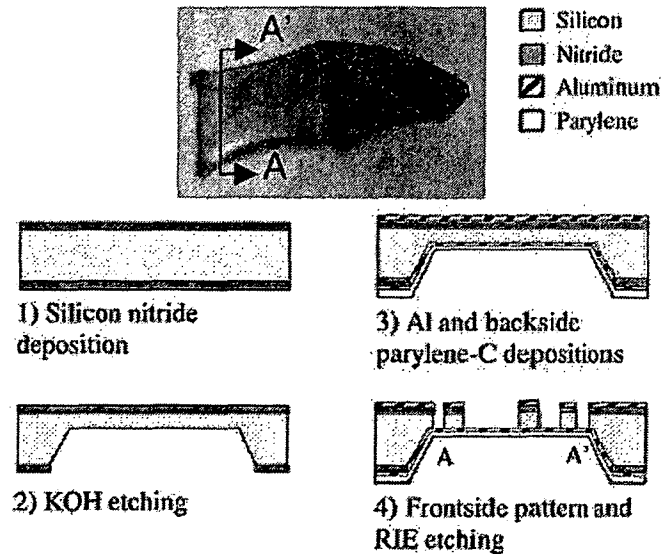
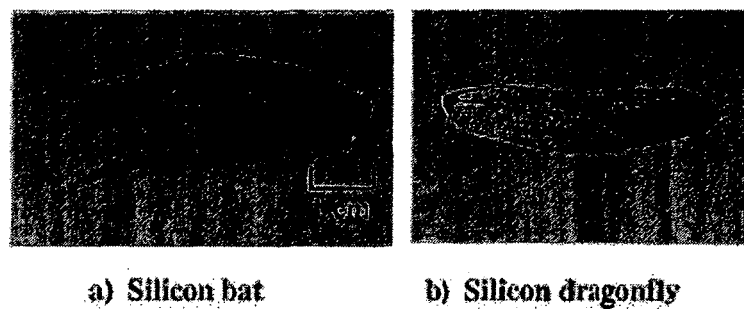


Figure 5-3. MEMS-based fabrication process used by Caltech (Pornsir-sirirak T. N., Tai, Nassef, & Ho, 2001)

The resulting wings, shown in Figure 5-4 were too fragile and broke easily; therefore a new process using titanium-alloy wing frames was developed. A common aerospace

titanium alloy (Ti-6Al-4V) was selected because it is strong, light, and widely commercially available. Furthermore, it is ductile, allowing it to be bent to provide wing camber. Other metals, such as stainless steel and aluminum were not suitable for this application because stainless steel is too heavy, and aluminum is too soft. The etching process for the titanium alloy can also be conducted at room temperature at a reasonable etching rate.



**Figure 5-4. MEMS fabricates wings with silicon structure
(Pornsin-sirirak T. N., Tai, Nassef, & Ho, 2001)**

Parylene-C was selected as the membrane material because 1) it can be deposited directly to the titanium alloy at any desired thickness; 2) its adhesion to titanium alloy is excellent; 3) it is light and strong enough to withstand high flapping frequency without tearing; and 4) it is deposited at room temperature and produces a conformal coating, allowing step corners to be uniformly coated.

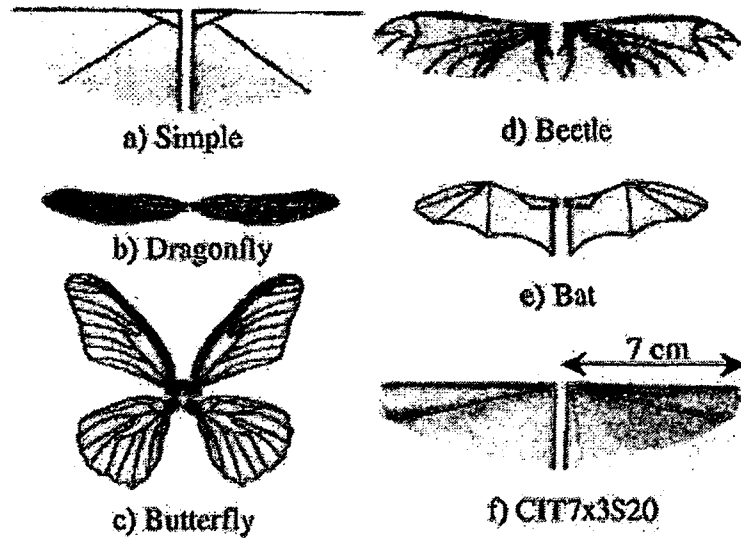


Figure 5-5. MEMS fabricated wings with titanium structure (Pornsin-sirirak T. N., Tai, Nassef, & Ho, 2001)

The MEMS wing fabrication technique allowed the stiffness distribution of the wing to be tailored in order to mimic natural wings. This was done by tapering the wing thickness by selectively etching parts of the wing in a diluted mixed solution of hydrofluoric (HF) and nitric (HNO_3) acids. Furthermore, unlike conventional machining processes, etching does not induce residual stresses in the part, eliminating warping and adverse deformation of the airfoil structure.

Wind tunnel testing of the MEMS wings with the complicated wing structures showed poor performance compared to real insect wings, which are much lighter and stiffer than the MEMS wings, and have more complex 3-dimensional shapes which contribute to higher lift generation as explained in chapters 3 and 4. As a result, Caltech focused on manually fabricating simple wing structures that would generate enough lift and force to fly their prototypes.

A similar process was used at TamKang University in Taiwan (Lung-Jieh, 2007; Yang, Hsu, Ho, & Feng, 2007) to fabricate “smart” wings employing a piezoelectric poly-vinylidene-di-fluoride (PVDF) polymer to measure lift forces in situ. Similar to the Caltech wings, the wing frames were made from etched titanium alloy, 250 μm (0.001 in) thick, by applying a photo-lithographically patterned photoresist to the titanium alloy substrate and etching in HF acid. The photoresist was then stripped and the wing frame was coated in parylene, which acts to insulate the metallic wing structure from the PVDF film. The PVDF film was glued to the wing, followed by a coat of parylene over the entire wing. The process is illustrated in Figure 5-6.

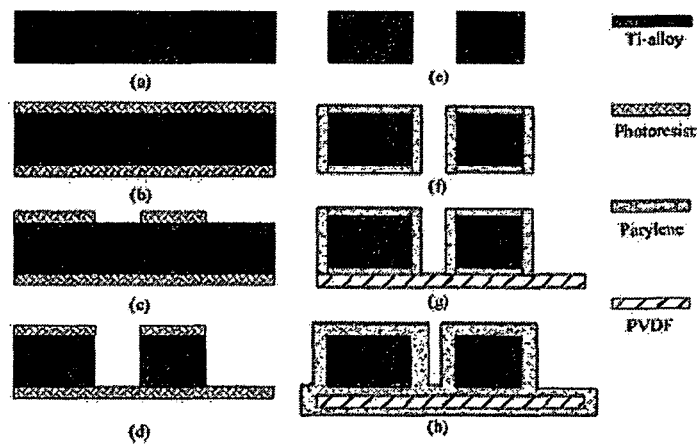


Figure 5-6. MEMS fabrication process using PVDF (Yang, Hsu, Ho, & Feng, 2007)

The piezoelectric PVDF membrane produced signals that correlated closely with the measured lift from a load cell, showing promise for the use of PVDF for the measurement of aerodynamic forces and/or active control of wings during flight.

While MEMS fabrication techniques have shown good results in producing complicated vein structures that are accurate and repeatable, the process is very expensive and requires special equipment and facilities. Furthermore, the materials that can be used in

this process are limited, and the few materials tested have shown poor aerodynamic performance in flapping wings due to their high stiffness.

5.2.3 Rapid prototyping

In 2010, Richter and Lipson (2010) of Cornell University demonstrated an 85 second passively-stable flight of a 3.89g (0.14oz) flapping MAV whose wings and airframe structure were fabricated using a rapid prototyping machine, or 3-D printer. The parts were made using an Objet EDEN260V rapid prototyping machine from a proprietary acrylic-based photopolymer called Objet FullCure 720 (ActiveKB Knowledge Management System, 2011). The use of this process, which is described in more detail in chapter 6, allowed the two wings, including the frame and membrane, as well as the hinge and pivot point, to be fabricated as one piece. The use of rapid prototyping also allowed a full set of MAV parts to be fabricated in approximately 60 minutes (with minimal labour required), with an additional 60 minutes required for cleaning, preparing, and assembling the components. This significantly reduced the design cycle time.

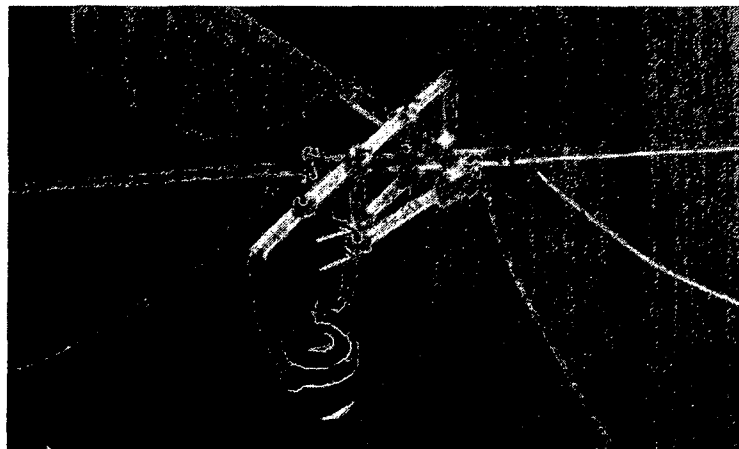


Figure 5-7. Cornell University's 3-D printed flapping MAV (Richter & Lipson, 2010)

In 2011, a UAV airframe fabricated using rapid prototyping was designed and flown by the University of Southampton, United Kingdom (Marks, 2011). The entire aircraft structure was “printed” from nylon using selective laser sintering (SLS). The use of 3-D printing allowed the designers to employ an elliptical wing planform and geodesic airframe structure, both of which are not found in conventional aircraft due to the challenges in construction. These complex structures, however, are easily fabricated using 3-D printing. Furthermore, the design contains no additional fasteners, and moving parts such as hinges were incorporated while printing, eliminating the need for assembly.



Figure 5-8. University of Southampton’s UAV fabricated using selective laser sintering (Marks, 2011)

Rapid prototyping methods have also been employed by the University of Delaware for the fabrication of their MAV’s airframe components (DiLeo & Deng, 2009), as well as in Michelson’s Entomopter (Michelson & Naqvi, 2003). Furthermore, rapid prototyping facilities have been built by the United States Air Force Research Laboratory (AFRL) as part of their MAV test facility (AFRL Air Vehicles Directorate, 2010).

Rapid prototyping technologies show promise for producing accurate and repeatable parts with a high level of detail. A wide range of materials are available, and small parts can be

made relatively quickly with very low labour requirements. This type of process favours parametric design techniques, since the parts are produced directly from computer models, and is therefore of greatest interest for this research. However, there are many types of rapid prototyping processes, each with their own unique advantages and disadvantages. These processes are described in the next chapter.

6 Rapid Prototyping Technology

Rapid prototyping (RP), or often called additive manufacturing, processes may provide solutions to some of the challenges of MAV wing fabrication. These processes are well suited for fabrication of small, complex shapes with good accuracy and repeatability, while significantly reducing labour requirements for small batch manufacturing. As shown previously in Chapter 5, various other MAV development programs are using rapid prototyping technology to produce structural components for MAVs. Rapid prototyping refers to the layer-by-layer fabrication of a 3-dimensional physical object directly from a computer-aided design (Cooper, 2001), and allows for the simple fabrication of complex shapes, such as internal structures and thin walls, with good dimensional accuracy and repeatability that would otherwise be impossible using traditional machining, forging, casting or other methods. Furthermore, there is usually minimal manual labour associated with rapid prototyping, with the exception of some post-processing (i.e. cleaning) of the part.

One of the advantages of using an additive process is that there is very little production waste, as opposed to subtractive processes such as machining. There is also no need for moulds, which can be very expensive and time consuming to make, especially for parts which are made in small quantities. Given the nature of this research, where small quantities of various part designs are to be manufactured and tested, rapid prototyping is well suited not only for wing design and manufacture, but for any design development process such as the fuselage or other aerodynamic surfaces. As demonstrated by the RepRap project (RepRap.org, 2011; Jones, et al., 2011), the rapid prototyping process can

also be used to create parts for improving and maintaining the rapid prototyping machine itself. This could be extended further to the fabrication of components for testing equipment.

One of the major disadvantages to rapid prototyping processes is that RP-fabricated parts are typically anisotropic in their properties due to the layering process used to fabricate the part, as shown in Figure 6-1 (Ahn, Montero, Odell, Roundy, & Wright, 2002). However, the impact on the structural properties of 3-D printed wings remains to be investigated; in fact, anisotropic properties inherent in the process could potentially provide aeroelastic benefits, such as spanwise stiffness and chordwise flexibility which could mimic the effect of wing corrugation found in insects.

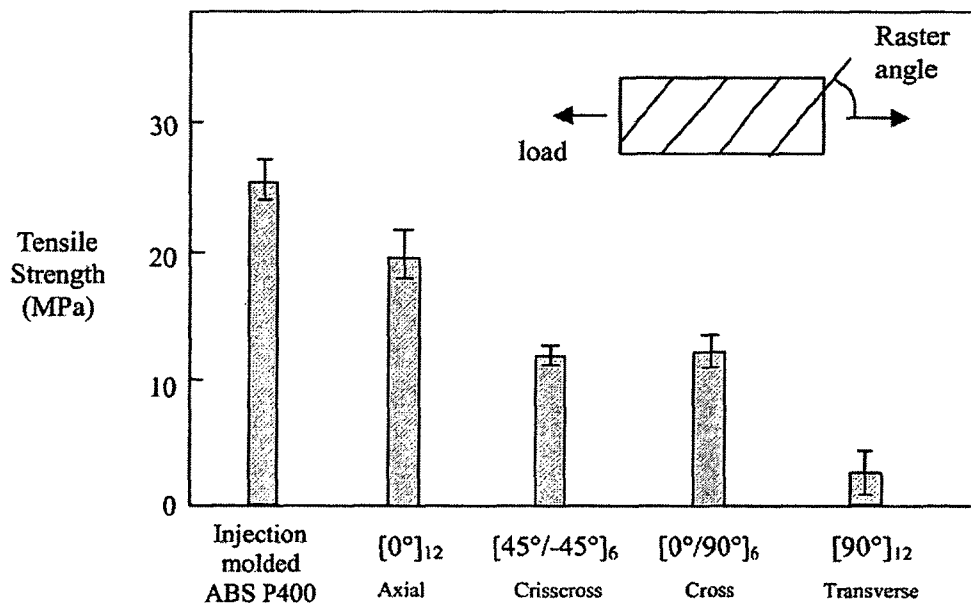


Figure 6-1. Anisotropy of material properties of parts produced using fused deposition modeling (Ahn, Montero, Odell, Roundy, & Wright, 2002)

Several types of rapid prototyping processes exist, where each process produces parts in a different manner, and therefore has its own advantages and disadvantages. Only those

processes that were deemed feasible for MAV wing manufacturing are described in this chapter.

6.1 Overview

In general, rapid prototyping processes follow the same principle of virtually “slicing” a computer-generated 3-dimensional part file, usually in stereolithography (.stl) format, into multiple thin layers, where the thickness of each layer dependent on the process to be used. Each cross section of the part corresponding to its layer is then “printed” with the build material. The specific material deposition/consolidation process is the major difference among the various RP processes. In all cases, the part is built up layer-by-layer until the 3-dimensional object complete. Depending on the process used, some post-processing of the part may still be required such as trimming, drilling or adding additional inserts for local reinforcement.

The following table provides a summary of some commonly used rapid prototyping processes and their specifications. These processes are described in further detail in subsequent sections.

Table 6-1 - Summary of Rapid Prototyping Processes [Derived from (CustomPartNet, 2009)]

Method	Build Medium	Materials	Speed	Resolution		Minimum layer thickness		Dimensional accuracy		Surface finish
				in	mm	in	mm	in	mm	
Fused deposition modeling	Filament	Thermoplastics: ABS, HDPE, PLA, PPS, PC; Elastomers	Slow	0.0050	0.1270	0.0050	0.1270	±0.005	±0.127	Rough
Ink Jet	Liquid	Thermoplastics: Polyester	Slow	0.0050	0.1270	0.0005	0.0127	±0.0010	±0.0254	Smooth
Jetted photopolymer	Liquid	Thermosets, photopolymers: Acrylates	Fast	0.0060	0.1524	0.0006	0.0152	±0.0010	±0.0254	Smooth
3-Dimensional Printing	Powder	Starch and gypsum-based ceramic	Fast	0.0080	0.2032	0.0020	0.0508	±0.004	±0.1016	Rough
Stereolithography	Liquid	Thermosets: Acrylates; Elastomers	Average	0.0040	0.1016	0.0010	0.0254	±0.005	±0.127	Smooth
Selective laser sintering	Powder	Thermoplastics: Nylon, Polyamide, and Polystyrene; Elastomers;	Fast	0.0050	0.1270	0.0040	0.1016	±0.010	±0.254	Average
Direct metal laser sintering	Powder	Stainless steel, aluminum, titanium	Fast	0.0050	0.1270	0.0010	0.0254	±0.010	±0.254	Average
Laser engineered net shaping	Powder	Stainless steel, titanium alloy	Average	0.0050	0.1270	0.0100	0.2540	±0.02	±0.508	Rough
Laminated object manufacturing	Sheet	Paper, plastics, composites, wood	Fast	0.0100	0.2540	0.0038	0.0965	±0.01	±0.254	Rough

6.2 Fused Deposition Modeling

Fused deposition modeling (FDM), or fused filament fabrication (FFF), is a common rapid prototyping process that produces parts by depositing an extruded filament layer-by-layer (Cooper, 2001). The thermoplastic filament, which ranges in diameter from 0.3mm (0.012 inch) to 1mm (0.0396 inch) (Ahn, Montero, Odell, Roundy, & Wright, 2002), is fed through heating elements via drive wheels to the extrusion tip, where the molten plastic is deposited onto the part. Filament materials include acrylonitrile butadiene styrene (ABS), high density polyethylene (HDPE), polyetheretherketone (PEEK), polycarbonate (PC), polyphenylsulphone (PPSF), and some elastomers (Cooper, 2001; Liou, 2008). A soluble support material can also be used to support floating or

unsupported part surfaces and cavities, and can be simply flushed away using a solvent once the part is completed. FDM parts typically require less post processing than other processes.

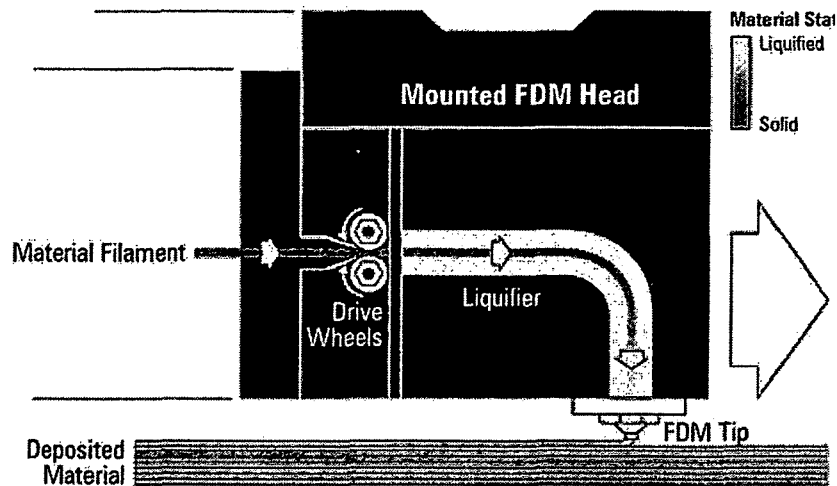


Figure 6-2. Illustration of the fused deposition modeling process (Ahn, Montero, Odell, Roundy, & Wright, 2002)

The advantages of FDM over other methods include the use of relatively high strength plastics; safe, laser-free operation; and minimal post-processing. Additionally, the use of soluble support material allows complete systems with moving parts to be made in one build operation with no additional assembly required. However, disadvantages include slower speed compared to laser-based processes, and the inability to make thin vertical columns and walls due to interaction with the extrusion head. Furthermore, parts fabricated using FDM tend to be highly anisotropic and contain stress concentrations throughout the part (see Figure 6-1).

Carleton University currently owns a Dimension 1200es 3D Printing machine, made by Stratasys Inc., which uses a proprietary *ABSplus* plastic as the build material (Stratasys, Inc., 2009). *ABSplus* is claimed to be 40% stronger than standard ABS material. Both the

soluble support material (Dimension SST) and breakaway support material (Dimension BST) are available with this machine. There are also open-source 3-D printers that use the same process, such as RepRap (Jones, *et al.*, 2011) and Makerbot (MakerBot Industries, 2011), which can be purchased for under \$2000 USD.

The ability to rapidly make complex parts, and even interacting components, from high strength polymers makes this an attractive process for MAV applications. The ability to use soluble support material means that the MAV wings, flapping mechanism, and fuselage could potentially be fabricated at once with no required assembly.

6.3 Selective Laser Sintering

Selective laser sintering (SLS) is another common rapid prototyping process, and is well-suited for making small-scale 3-dimensional parts. SLS can be used to create parts with feature sizes as small as 0.76 mm (0.030 in), with dimensional tolerances of 0.25 mm (0.010 in) (Cooper, 2001).

The laser sintering process begins by spreading a thin layer of polymer powder over the building platform. The powder is then quickly pre-heated above its crystalline temperature, T_c , to prevent the sintered material from cooling too quickly, which results in shrinking and warping of the part. The scanner-guided laser beam then sinters the layer of powder according to a CAD file, forming a thin layer of the part. The building platform is then lowered, a new layer of powder is applied, and the next layer is sintered and fuses to the previous layer. Once the part is complete, the part is cooled such that homogeneous cooling of the melted polymer takes place (Rechtenwald, Krauß, Pohle, & Schmidt, 2007).

Selective Laser Sintering has several advantages (Cooper, 2001):

- a. Scanning speed – The fast scanning speed of the carbon dioxide laser allows large part cross-sections to be scanned in seconds, and multiple parts to be made with a short turn-around time.
- b. 3D part nesting – The powder-bed media used in the SLS process allows multiple parts to be “nested” throughout the build volume with no support structure required. This means that many parts can be made in a single run
- c. Minimal material waste – The SLS process uses only the amount of material required to make the part and the rest is recycled for building other parts.

Laser sintering is commonly used with polyamides, which are semi-crystalline polymers such as Nylon; however, laser sintering has been successfully used on polyetherether ketone (PEEK), a polymer with high tensile strength and good temperature and chemical resistance (Rechtenwald, Krauß, Pohle, & Schmidt, 2007).

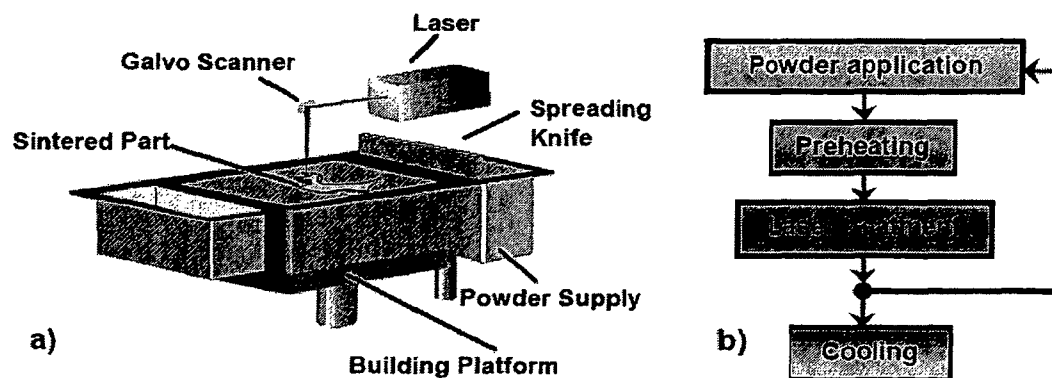


Figure 6-3. Selective laser sintering set-up (a) and process (b) (Rechtenwald, Krauß, Pohle, & Schmidt, 2007)

Selective laser sintering is an attractive process for MAV component fabrication because it allows wings with complex vein patterns to be printed with camber and twist without

the need for additional support material. Investigation into the suitability of materials compatible with the SLS process for MAV components would be required.

6.4 Stereolithography

Stereolithography (SLA) is a similar process to selective laser sintering; however, instead of sintering a polymer or metallic powder by a high powered laser, a photosensitive polymer resin is selectively cured by a relatively low powered laser through photopolymerization (Cooper, 2001). The light energy acts as a catalyst to cross-link monomers into polymers, which finally develop into a cross-linked solid polymer. Like SLS, stereolithography machines apply a thin layer of liquid resin over the part or build platform, and the laser scans the part cross section to form the solid part layer. The part is then lowered, a new layer of liquid is applied, and the next layer is scanned with the laser. Once the part is complete, the part is taken out of the resulting vat of uncured resin surrounding the part. Some post processing is required to remove the part from the base and remove any material acting as support structure for hollow or over-hanging parts.

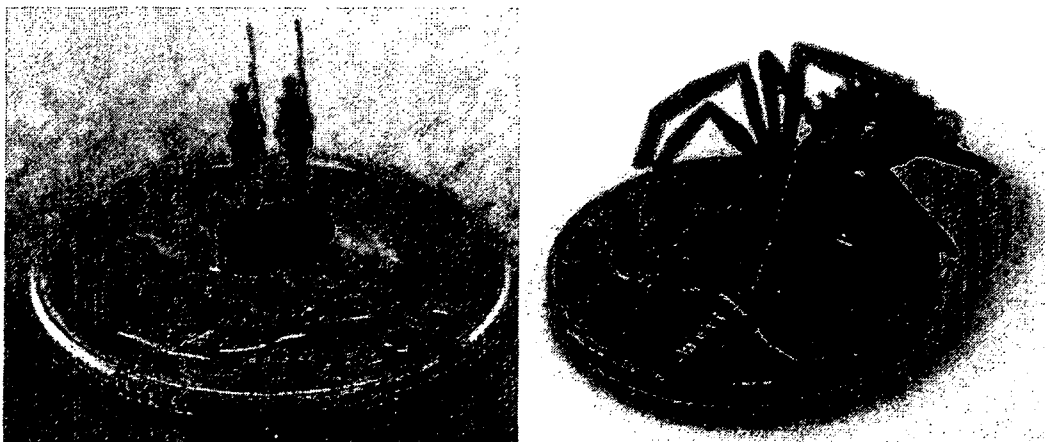


Figure 6-4. Examples of parts fabricated using stereolithography (RJM Rapid Prototyping)

The major advantages of stereolithography are its excellent surface finish and dimensional accuracy. Finely detailed features, including thin vertical walls and sharp corners, can also be made easily using this process. Furthermore, stereolithography has good speed and there are a range of available resins with good mechanical and thermal properties. On the other hand, this process is limited to thermosetting polymers, and the cost of these photo-curable polymers is relatively high, at approximately \$250 per litre (\$950 per gallon) (Ellsworth Adhesives, 2010).

Stereolithography shows promise for MAV applications because it can fabricate complex parts with good dimensional accuracy and surface finish. However, it may not be suitable for cambered wing shapes without the addition of support structures that must be later removed during post processing and could damage the part. Soluble support material is not available in the stereolithography process.

6.5 3-Dimensional Printing

While many rapid prototyping processes are referred to as “3D printing”, 3-Dimensional Printing (3DP) refers to a specific process licensed by the Massachusetts Institute of Technology (MIT) (Cooper, 2001). It is similar to selective laser sintering in that it uses a powder media; however, instead of using a laser to sinter the particles, liquid binder is jetted onto the powder using ink-jets. Similar to conventional ink jet printing, each layer is “printed” by making consecutive scans across the part, depositing the binder where required based on the part’s CAD file. The build platform is then lowered by the thickness of one layer, a new layer of powder is spread over the part, and the process repeats until the part is complete.

While inexpensive, 3DP cannot produce parts with the required material properties due to limited material selection, which include starch- or gypsum-based powders (Cooper, 2001). The system also provides relatively poor dimensional accuracy and a rough surface finish. Therefore, this process is used typically for concept verification models, and not functional prototypes. Throughout this thesis, “3-D printing” is used synonymously with “rapid prototyping”, and does not refer to this particular 3DP process.

6.6 Inkjet-Based Printing

The Inkjet Printing process is derived from 2D printing techniques with ink and paper; however, the ink is replaced with thermoplastic and wax materials (CustomPartNet, 2009). The build material is a molten thermoplastic that hardens upon cooling instantaneously on the part. The support material is a wax material that also hardens upon cooling and is easily removed during post-processing. Both the build material and the support material are deposited from the jetting head as it moves in the x- and y- axes. The build platform then lowers and the next layer is deposited.

The Inkjet-based process can produce complex parts with excellent surface finish, very small layer thicknesses, and high resolution and accuracy. The disadvantages include slow build speed, few material options, and fragile parts (CustomPartNet, 2009).

6.7 Jetted Photopolymer

The jetted photopolymer technique, or photopolymer inkjet printing, is similar to both the inkjet-based process and stereolithography. A photopolymer resin is deposited by the inkjet head and is cured under ultra-violet (UV) light. Similar to stereolithography, the build material is an acrylate-based polymer, while the support material can be either a gel

or wax material that is washed away once the part is complete. The jetted photopolymer process offers good accuracy and surface finish with fast build speed; however, feature details and material properties are not as good as those provided by stereolithography. This process is the basis for the Objet Polyjet series of rapid prototyping machines, and was used by Cornell University for the fabrication of their functional MAV prototype (Richter & Lipson, 2010).

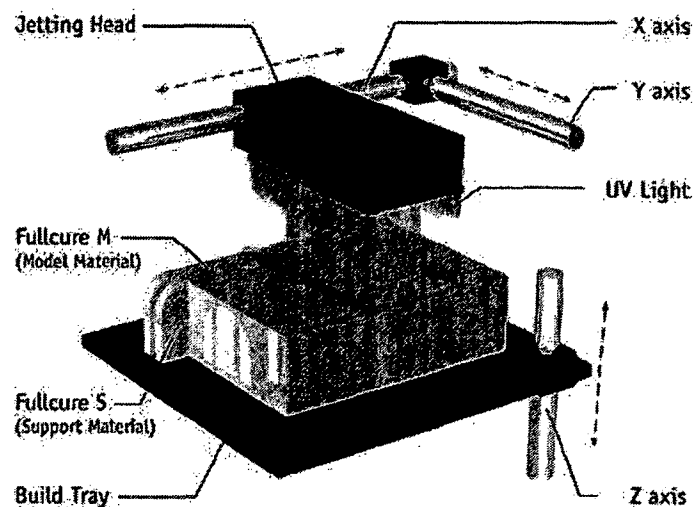


Figure 6-5. Illustration of the jetted photopolymer process used by Objet (Proto3000, 2008)

6.8 Laser Engineered Net Shaping (LENS)

Laser Engineered Net Shaping (LENS) produces full-strength metallic parts upon removal from the machine. Metallic powder is injected from four tubes into the focal point of a high-powered laser, welding the material on top of the previous layer (Cooper, 2001). The process is carried out in an inert environment to prevent oxidation of the powder during the build. Available materials include stainless steel and titanium alloy Ti-6Al-4V. The LENS process is capable of making simple to semi-complex parts with a dimensional accuracy of ± 0.051 mm (± 0.020 in) and layer thicknesses between 0.25mm

(0.010 in) to 2.5 mm (0.100 in). However, objects with internal overhangs or free-hanging surfaces cannot be made easily due to the lack of fixed supports. Upon part completion, the part must be mechanically removed from the build surface, since it is essentially welded to it. The surface finish is also typically rough, requiring some machining.

The major advantage of the LENS process is its ability to fabricate parts with full strength properties without any post curing or heat treatment, particular for metals such as Ti-6Al-4V. The ability to use rapid prototyping technology with Ti-6Al-4V, a strong and lightweight metal, makes the LENS process of interest for MAV applications, particularly for making detailed wing frames. However, the wing would need to be fabricated standing vertically due to the nature of the process, where the part is fused to the build surface. This may not be suitable for long, thin wings which may deflect when stood on end during building. Furthermore, metallic MAV wings may not be suitable, due to stiffness and weight requirements.

6.9 Laminated Object Manufacturing

Laminated object manufacturing (LOM) (Cooper, 2001) is a hybrid between additive and subtractive processes. The part is built up layer-by-layer, but each layer is individually cut to shape by a laser. Build material can be made of paper, plastic, or composite material; have range in thickness from 97 μm (0.0038 in) to 127 μm (0.005 in), and has a heat-sensitive adhesive backing. The first layer of build material, supplied from a roll, is laid horizontally on the support surface, and a carbon dioxide laser is used to cut the part cross section in the x,y plane. The next layer of material is then applied and a heated roller traverses across the face of the part to activate the adhesive and bond the part layers

together. The laser then cuts the new layer's cross section. As the part is created, excess material around the part is cross-hatched, forming "cubes" that are later removed once the part is completed. This post-processing step can be labour intensive for large parts. LOM can produce parts with dimensional tolerances of approximately ± 0.25 mm (± 0.010 in) (Cooper, 2001).

The major advantage of the LOM process is its ability to quickly fabricate large, thin parts. Parts requiring more layers, however, require more time. There are also several disadvantages to this process. Since the material is cut by a laser, smoke and fumes must be ventilated to the outside or a proper filtering device. There is also a great deal of wasted material. This process may not be well suited for curved surfaces, and would therefore be limited to flat wing planforms, unless the laminate is laid over a preform. In this case, a new preform would need to be fabricated for different wing designs.

This process may be well-suited for fabricating many thin wings quickly and affordably, since only a few layers would be required. The ability to use high-strength and low density polymer films, composites, or even metals should be investigated. Each layer of composite material could be oriented as required to tailor strength and stiffness. Furthermore, layers of different materials may be possible, such as conducting outer layers and a piezoelectric (PVDF) inner layer, or a stiff outer wing frame with a continuous flexible inner membrane.

6.10 Process selection

Both selective laser sintering (SLS), stereolithography (SLA), and fused deposition modeling (FDM) were identified as feasible potential processes for manufacturing wings

based on the range of potential build materials with suitable material properties and part resolution; however, the costs associated with performing manufacturing trials using SLA and SLS were prohibitively high. As of 2010, the least expensive non-open-source 3-D printer commercially available was the V-Flash made by 3D Systems, at \$9,900 (Jones, et al., 2011), while other rapid prototyping machines can be orders of magnitude higher in price.

An alternative to purchasing a commercial 3-D printer is to out-source the part fabrication to companies with rapid prototyping equipment. An Ottawa-based manufacturing organization with an SLS machine quoted a cost of \$1,750 for the fabrication of nine 76 x 76 x 13 mm (3 x 3 x 0.5 in) test parts, which was considered prohibitively high. While there are many companies that offer online submission of part files and can ship the completed part for a more reasonable cost, this method was not deemed feasible for the purposes of research and development due to long lead times and recurring costs.

The feasibility of using the Carleton University Department of Mechanical and Aerospace Engineering's Dimension 1200es FDM machine was also explored. This machine is shared across the Department, and access to the machine is not always possible due to high demand. Furthermore, the Department charges an operating cost of \$10 per hour for use of the machine. Finally, due to the fact that it is a commercial machine and belongs to the University, modifications to the hardware, software, settings, or print materials are not possible.

With the use of commercial rapid prototyping machines deemed unfeasible, remaining options included the use of open-source 3-D printers, or to develop a custom 3-D printer in-house. Photo-curable resins for the development of a stereolithography cost approximately \$250 per litre (\$950 per gallon) (Ellsworth Adhesives, 2010), whereas filament for a fused deposition modeling machine costs approximately \$20-40 per kg (\$10-20 per lb). There are several open-source fused deposition modeling machines that have been developed to a relatively advanced state, with a lot of documentation and community support available; therefore, this research could be leveraged by the existing work done by the open-source community, while still being able to modify the hardware and software as necessary. The lessons learned from the use of this readily-available open-source technology could be eventually applied to a custom process developed in-house in future phases of this research. Therefore, the use of open-source fused deposition modeling technology was selected as the most feasible process for the fabrication of flapping micro air vehicle wings. This is described in further detail in Chapter 8.

7 Scope of Research

The preceding chapters have reviewed the literature and current state-of-the art in micro air vehicles, flapping wing flight, and rapid prototyping manufacturing processes. Based on this review, this chapter will outline the scope and the major goals of this research, as presented in the following chapters.

7.1 Literature review conclusions

As shown in Chapter 2, micro air vehicle (MAV) technology, particularly for flapping wing vehicles, is still in the development stage and has not yet reached sufficient maturity to perform useful missions. One of the major areas for development is to increase the understanding of flapping wing flight and aerodynamics at the MAV scale. While Chapters 3 and 4 described some of the knowledge that has been gained regarding flapping wing aerodynamics, kinematics, and design, there are still opportunities to continue to explore flapping wing flight and functional MAV designs.

Researchers and engineers have used a variety of manufacturing processes to fabricate wings for MAV prototypes, as was shown in Chapter 5; however, many of these processes are not well suited to prototype development and testing due to their cost, long process times, and/or manual labour requirements. Furthermore, the resulting wings often lack the required properties to achieve sufficient aerodynamic performance. Upon review of these processes, it was concluded that rapid prototyping was the most promising technology for rapidly fabricating customized and detailed MAV wings. A review of potential rapid prototyping technologies in Chapter 6 showed that open-source fused deposition modeling (FDM) technology is a feasible rapid prototyping process for

quickly fabricating accurate and repeatable wing prototypes at low cost and with little manual labour required.

7.2 Research Scope

The scope of the work presented in the remaining chapters of this thesis comprises the set-up, testing, and operation of an open-source fused deposition modeling machine, called the RepRap Mendel, for the purpose of fabricating prototype MAV wings. The fused deposition machine used in this research was comprised of “stock” hardware and software, with little customization or modifications performed. By fabricating prototype parts, the advantages and limitations of the process were identified, and recommendations for further improvements to the hardware and software were made.

The process was quantitatively assessed based on manufacturing repeatability and performance of the fabricated parts through aerodynamic spin testing and structural stiffness measurements. These tests also served to identify any inherent aerodynamic or structural benefits realized through the use of the FDM process, and to determine whether the process limitations, such as materials and resolution, have any adverse effects on wing performance. The feasibility of the FDM process as part of the overall design cycle was also evaluated by performing a parametric study of different wing designs. Not only was this study used to assess the process as part of the overall design development process, but it also served to gain valuable information about the design of flapping wings for MAVs.

Overall, the aim of this research was to lay a foundation for future MAV research by identifying and developing a process for MAV prototype development, while at the same

time gaining insight into the design of flapping wings. This work, along the conclusions and recommendations drawn from it, are presented in the following chapters.

8 RepRap Mendel

In light of the advantages of rapid prototyping technology presented in the previous chapter, the RepRap (Replicating Rapid Prototyper) Mendel (RepRap.org, 2011) was selected as the most feasible solution for this research. The RepRap Mendel is an open-source desktop-sized rapid prototyping machine, or 3-D printer, that uses fused-deposition modeling (FDM) to build 3-dimensional parts from thermoplastic polymer filament. This specific type of printer was selected over other similar machines primarily because of its low capital cost and low operating costs; however, it also has the potential to be modified to suit our specific applications.

This chapter provides some historical background behind the RepRap project, as well as an explanation of open-source technology. The hardware and software employed by using the RepRap Mendel are also described, followed by a description of the various settings and calibration procedures used to produce 3-dimensional parts.

8.1 RepRap history

The RepRap project was started at the University of Bath, United Kingdom, in 2004 by Adrian Bowyer (Jones, *et al.*, 2011). The intent of the RepRap project is to develop a machine that is capable of self-replicating - or at least producing as many of its own parts as possible. The first generation RepRap printer, called Darwin, was built in 2007. This machine later evolved into a simpler and more robust machine with a larger build volume, called Mendel. To date, the Mendel has further evolved into the Prusa Mendel and Huxley. The Prusa Mendel has a lower part count and is easier to build than the original Mendel, while the Huxley is a smaller, “travel sized” version of the Mendel with

a smaller build volume. The evolution of the RepRap so far has primarily focused on ease of construction, reduced part count with a higher percentage of printable parts, and increased reliability. In general, each generation of RepRap printer operates under the same principles and capabilities such as print speed and resolution have remained relatively constant. The RepRap versions developed to-date are shown in Figure 8-1.

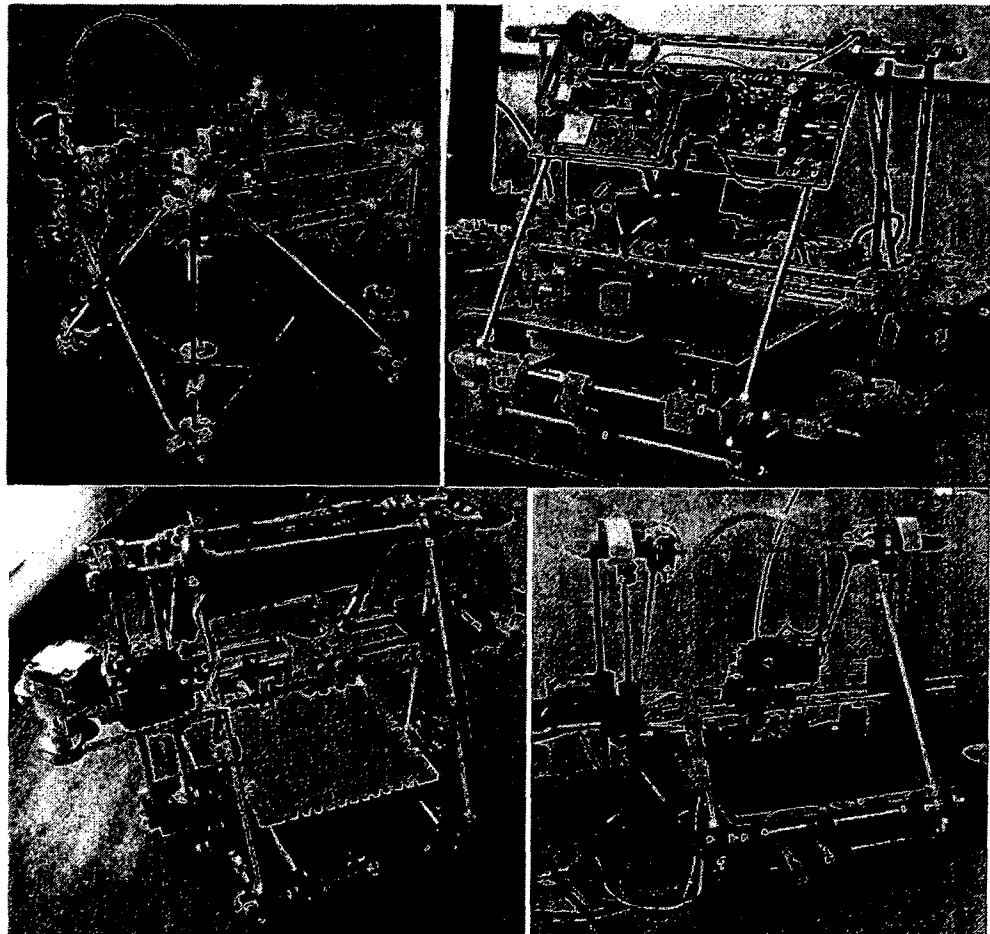


Figure 8-1. Evolution of RepRap. Clockwise from top left: Darwin, Mendel, Prusa Mendel, and Huxley.

8.2 Specifications

In terms of performance, RepRap printers, and most other open-source 3-D printers, do not yet match that of commercial systems. Table 8-1 compares some of the RepRap

Mendel's specifications with commercial FDM printers such as the Stratasys Dimension 1200es and the uPrint SE desktop-sized printer.

These commercial printers tend to be much more reliable, and in general have better accuracy and part resolution. Furthermore, commercial printers offer a turn-key solution, while the RepRap Mendel requires assembly and extensive calibration and testing. The trade-off, however, is the much higher cost of commercial systems, as well as the inability to modify or service the machine yourself. This is discussed further in the next section. The RepRap Mendel offers comparable print speed and build volume, while in a much smaller overall size and weight. Furthermore, the Mendel allows for many material options, while commercial printers are usually limited to only a few materials, which are often proprietary (and thus expensive).

Table 8-1. RepRap Mendel specifications compared to commercial 3-D printers

		RepRap Mendel		Stratasys Dimension 1200es		Stratasys uPrint SE	
Price of all materials		Approx. \$500-1000		\$32,900		\$15,900USD	
Annual Service Cost		Occasional oiling = \$8. Can print its own replacement parts at material cost.		-		-	
Size	W	500 mm	20 in	838 mm	33 in	635 mm	25 in
	D	400 mm	16 in	737 mm	29 in	660 mm	26 in
	H	360 mm	14 in	1143 mm	45 in	787 mm	31 in
Weight		7.0 kg	15.5 lbs	148 kg	326 lbs.	76 kg	168 lb
Build Envelope	W	200 mm	8 in	254 mm	10 in	203 mm	8 in
	D	200 mm	8 in	254 mm	10 in	152 mm	6 in
	H	140 mm	5.5 in	305 mm	12 in	152 mm	6 in
Materials		PLA, HDPE, ABS & more.		ABSplus		ABSplus	
Material Cost		PLA: \$14/lb, HDPE: \$7/lb, ABS: \$10/lb		-		-	
Speed		15.0 cm ³ (0.92 in ³) per hour		16.4 cm ³ (1 in ³) per hour		16.4 cm ³ (1 in ³) per hour	
Accuracy		Nozzle diameter: 0.5 mm (0.020 in), Minimum feature size: 2 mm (0.080 in) Positioning accuracy: 0.1 mm (0.004 in) Layer thickness: 0.3 mm (0.012 in)		Layer thickness: 0.254mm (0.010 in)		Layer thickness: 0.254mm (0.010 in)	
Finished surface quality		Fair to Good		Good		Good	
Total part count		1390 including fasteners 198 excluding fasteners		n/a		n/a	
Percentage of printable parts		48% (excluding fasteners)		None		None	
Source		RepRap.org		Dimensionprinting.com		uPrint3Dprinting.com	

8.3 Open-source technology

The RepRap Mendel uses open-source hardware and software, which means that all instructions, drawings, schematics, software and code are freely available to the public. Consequently, the cost of the RepRap printer was very low in comparison to commercial rapid prototyping machines, at less than \$1000USD. Furthermore, the hardware and software may be modified as necessary to meet project requirements without voiding any commercial warranty.

RepRap is licensed under the GNU General Public License (GPL), as published by the Free Software Foundation (RepRap.org, 2011; Free Software Foundation, 2010). Under the GPL, all RepRap software and documentation is freely available to use, copy, distribute and/or modify; however, anyone who uses or modifies it must also freely distribute it, and may not copyright, license or restrict it in any other way.

The development of the RepRap Mendel is community-based, where RepRap users around the world can contribute and collaborate to improve the system. These contributors include both academic researchers and hobbyists. This results in relatively quick development of the system. However, this rapid development does not usually occur serially, but in parallel. This fragmentation of the development process has resulted in various alternate RepRap configurations and adaptations existing at any given time. Consequently, it becomes difficult to track the development progress of the overall system and distinguish which development is relevant to one's own hardware and software version.

Another issue arising out of open-source, community-based development is that there is generally a lack of clear and up-to-date documentation. The rapid evolution of the system quickly makes much of the available information obsolete. Furthermore, the information is not all found in one place and from a single source. While the RepRap Wiki (RepRap.org, 2011), which is editable by all RepRap users, is the primary source of information and instructions for the RepRap Mendel, the majority of useful how-to and troubleshooting guides exist as web-log (blog) entries posted on individual users' websites. Fortunately, there are various online forums and chat-rooms associated with both the RepRap and open-source 3-D printing in general, where users can receive

support from the community. These blogs and forums proved to be invaluable for overcoming some of the challenges and obstacles encountered when setting up and calibrating the Mendel printer.

8.4 Principle of operation

The RepRap Mendel uses a process called fused-deposition modeling (FDM), or fused filament fabrication (FFF), to fabricate 3-dimensional objects. For a detailed description of the FDM process, see Chapter 6. The Mendel is a 3-axis Cartesian robot which moves the printer tool-head in the x-, y-, and z-axes relative to the build platform, functioning in the same way as a 3-axis computer-numerical-control (CNC) mill, with the exception of using a thermoplastic extruder instead of a milling tool head. In the case of the Mendel, the extruder moves on a gantry along the x-axis, while the build platform moves in the y-axis. For movement in the z-axis, the entire x-axis gantry moves vertically along two threaded rods. Each axis is belt-driven using a 12 volt stepper motor. Thermoplastic filament is fed into the extruder, where it is melted and extruded through a nozzle onto the build platform. The extruder and build platform simultaneously move back and forth horizontally, depositing molten plastic as it moves until the part cross section corresponding to that layer is complete. The x-axis gantry then moves vertically and the next layer is printed directly on top of the previous layer. The process continues until the entire part has been fabricated.

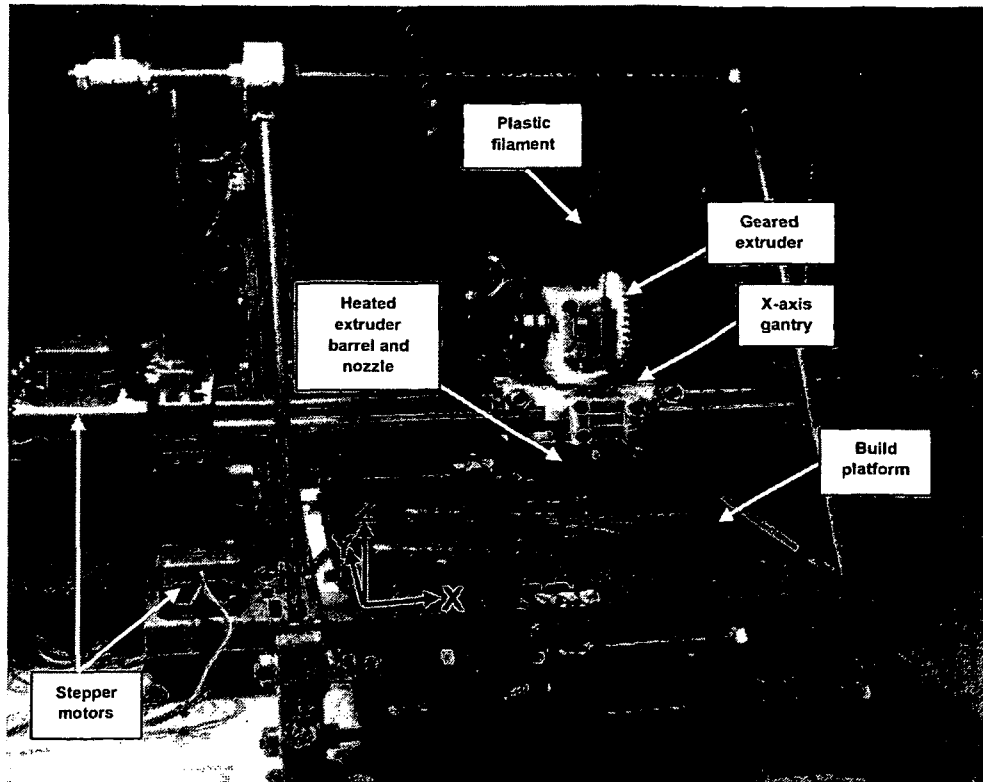


Figure 8-2. RepRap Mendel 3D printer

The thermoplastic extruder consists of a drive system, a thermal barrier, a heated barrel, and a nozzle. The drive system is mounted to the x-axis gantry, which moves along two steel rails. Plastic filament is fed into the extruder through the top of the extruder bracket. A knurled bolt passing through the bracket grips the filament and forces it down into the heated barrel. The knurled bolt is driven by a stepper motor through two plastic gears with an 11:39 gear ratio. The geared extruder allows the extruder stepper motor to rotate at a higher RPM and provides better resolution on the filament extrusion (i.e. more motor steps per mm of extruded material). The extruder drive system is shown in Figure 8-3, while the extruder hot section is shown in Figure 8-4.

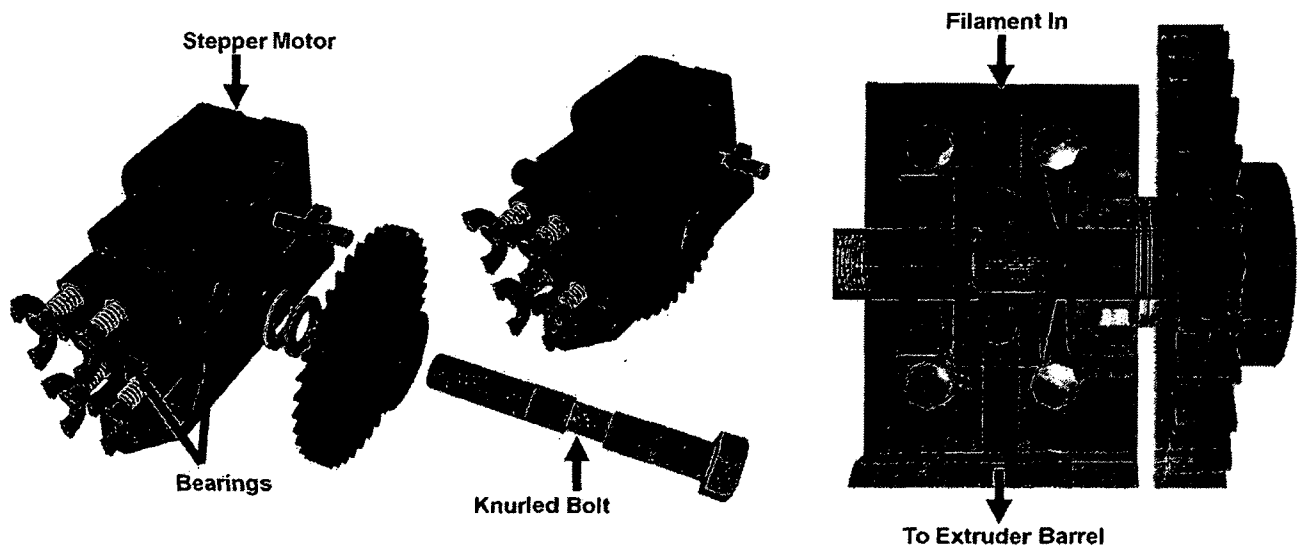


Figure 8-3. Extruder assembly, showing exploded view (left), assembled view (centre) and cross section of filament drive system (right). (Hodgson, 2011).

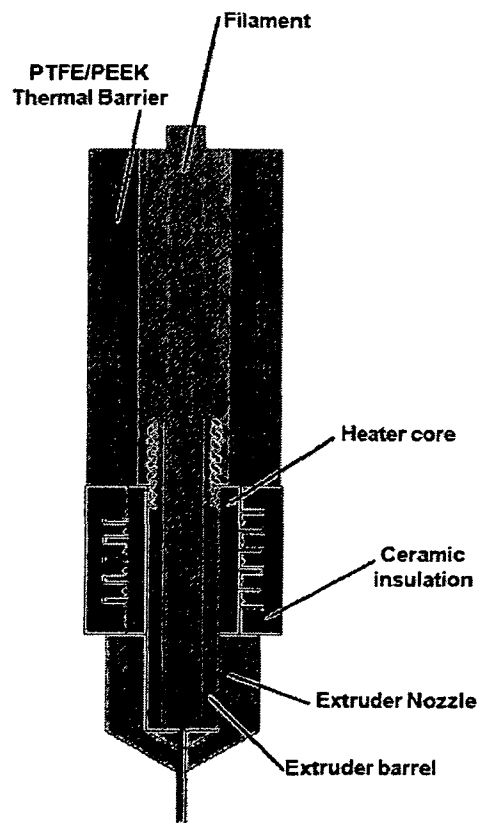


Figure 8-4. Cross section view of the extruder barrel (Sluis, 2011).

The thermal barrier insulates the heated barrel, and consists of an inner hollow cylinder of poly-tetra-fluoro-ethelene (PTFE), commonly known as Teflon, and an outer cylinder of poly-ether-ether-ketone (PEEK). The inner tube guides the plastic filament feedstock down into the heated barrel. The PTFE reduces friction between the thermal barrier and the filament. The outer PEEK material, which has a higher melting temperature than PTFE, is used to prevent deformation and creep of the thermal barrier when heated.

The brass heater barrel is where the filament feedstock is melted. Surrounding the barrel is a brass heater core which is wrapped with approximately 30 mm (1.18 in) of 30-gauge nickel-chrome wire along its length, for a total wire resistance of approximately 6 ohms, for a power output of 24 watts at 12 volts. The heater core is insulated with a ceramic coating and a layer of woven fiberglass. The molten plastic is forced out through a small hole in the tip of the brass nozzle, which is screwed onto the end of the threaded barrel. Various nozzle outlet diameters can be used, however a 0.5 mm nozzle diameter is most commonly used because it gives a good balance between part resolution and printer reliability. Smaller nozzle diameters provide better part resolution, but can be more prone to clogging due to dirt, dust, or other contaminants which can enter the extruder as the filament is drawn into it.

8.5 Hardware

This section describes the mechanical and electronic hardware contained in the RepRap Mendel 3-D printer used for this research.

8.5.1 Mechanical hardware

The structure of the Mendel is made primarily of common, off-the-shelf parts such as bearings, nuts, bolts, threaded rod, and metal bar-stock. The remainder of the parts specific to the Mendel is designed to be printed from another 3-D printer, such as another RepRap. In the case of the RepRap Mendel used for this research, the parts were purchased as a kit from Fleming CNC (Fleming CNC, 2010), which were computer-numerical-control (CNC) machined from a wood-plastic composite material rather than printed. In theory, the printer's structure can be made from any suitable materials, and in any shape or configuration, provided the appropriate changes are made to the firmware and software, such as build volume size and axis travel directions.

8.5.1.1 Modifications from stock configuration

The kit from Fleming CNC included a direct current (DC) motor-driven extruder; however, this configuration was not only large and heavy, but there were also problems getting the motor to operate properly. The DC motor-driven extruder was replaced with a stepper motor-driven geared extruder. The extruder assembly and gears were printed in-house on a commercial Stratasys Dimension 1200es rapid prototyping machine based on part files downloaded from the RepRap Wiki (RepRap.org, 2011).

Another modification to the stock configuration was the addition of a heated build platform. The heated build platform raises the temperature of the build platform to as high as 115°C. This provides better adhesion between the deposited plastic and the platform during the print, as well as reduces warping and shrinking of the part. The heated build platform is described in further detail in section 8.6.

The arrangement of electronics was also modified to allow better access to the extruder and shorten the wire and cable lengths. This consisted of mounting all of the circuit boards to the side of the printer, rather than mounting them at the top of the printer along the cross-brace. This had no effect on functionality of the printer.

8.5.2 Electronic hardware

The electronic hardware for the RepRap Mendel was purchased as a kit from TechZoneCommunications.com; however, the schematics and bill-of-materials for creating these circuit boards are freely available under the open-source license. The electronic hardware consists of the following components:

- a) Motherboard
- b) Stepper controllers
- c) End stop optoelectronic-switches
- d) Extruder controller

Each of these circuit boards is described in the following sub-sections. The entire system is powered by a single 12VDC power supply, with the exception of the heated build platform described in section 8.6. A schematic of the system is shown in Figure 8-5. Solid lines represent data transfer, while dotted lines represent power connections.

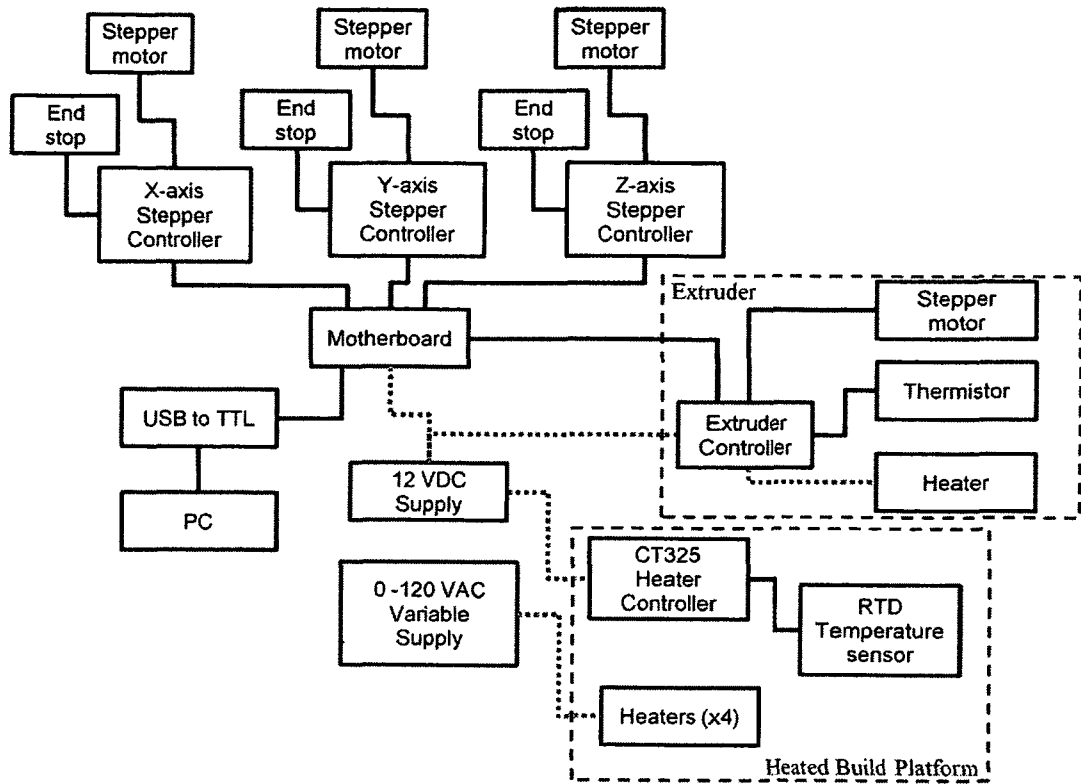


Figure 8-5. Schematic of the RepRap's electronic hardware.

8.5.2.1 Motherboard

The RepRap motherboard is based on the Arduino open-source microcontroller board, and uses an ATmega644P microprocessor chip with 64 kilobytes of flash memory. The motherboard controls all the functions of the printer and communicates with the computer (PC) via a universal serial bus (USB)-to-serial transistor-transistor logic (TTL) adaptor. The machine code, or G-code, is sent from the computer to the motherboard via serial communication. The G-code is then interpreted by the motherboard, which sends the necessary commands to the other peripheral boards, such as the stepper motor controllers and the extruder controller.

8.5.2.2 Stepper controllers

The stepper controller boards receive digital signals from the motherboard and move the stepper motors accordingly. There is an independent stepper controller for each axis (x, y, and z). Each stepper controller includes a potentiometer that can be used to vary the input voltage to each stepper motor. This is useful for reducing or increasing the motor torque where necessary. If torque requirements are low, the motor voltage is decreased to prevent overheating of the stepper motors.

8.5.2.3 End stop optoelectronic-switches

An optoelectronic-switch is placed at the zero position of each axis. A bracket is placed on the build platform, the extruder gantry, and the z-axis assembly such that when each reaches its zero position, the bracket passes through the infrared beam across the optoelectronic-switch and the movement stops. The end stops are connected to the motherboard, telling the motherboard whether each axis is at its respective zero, or “home”, position.

8.5.2.4 Extruder controller

The purpose of the extruder controller is to control the functions of the extruder, such as the barrel temperature and the extruder’s stepper motor. This board is also based on the Arduino microcontroller board with an ATmega644P microprocessor chip. A thermistor mounted to the extruder’s nozzle is connected to the extruder controller in order to measure the extruder’s temperature. The extruder controller then turns power on or off to the nickel-chrome heating element until the desired temperature is reached. Similar to the stepper controllers, a potentiometer is used to adjust the voltage, and thus torque, of the stepper motor. The stepper controller can also be used to control either an additional

extruder (for depositing a different material type or colour, for example) or a fan for cooling the extruder; however, these features are not currently used.

8.6 Heated build platform

Initial tests using the stock printer configuration, without a heated build platform, were satisfactory when using poly-lactic acid (PLA) as the build material. In this configuration, the built platform consisted of a polycarbonate plate covered with polyimide (Kapton) tape. At room temperatures of approximately 20°C (68°F), the adhesion between the deposited filament and the polyimide tape was sufficient to secure the part in place on the build platform throughout the build process, while still being able to remove the part from the platform upon completion without damaging the part. PLA also exhibits little shrinkage upon cooling, which resulted in little warping. However, the use of acrylonitrile butadiene styrene (ABS) as the build material was difficult at room temperature. The adhesion between the polyimide tape and the ABS was poor, often resulting in the part releasing from the build platform during the print process. Furthermore, the ABS shrinks as it cools, causing the first layers of the part to curl upward and peel off of the build platform. Consequently, the part would become detached from the build platform during the print and the part would be ruined.

Other RepRap users reported that the use of a heated build platform improves the adhesion between ABS and the polyimide film. The elevated temperature of the build platform also reduces the shrinkage and warping of the part upon cooling.

Four flexible, silicone-coated etched foil resistive element heating pads were purchased from Minco. Each adhesive-backed heating pad measures 50.8 mm x 50.8 mm (2 in x 2

in), and has a resistance of 17.8 ohms and a maximum power density of 136 W, or 7.4 W/cm² (48 W/in²). The heaters were evenly spaced on the bottom side of the build platform's aluminum base and connected in parallel to a variable transformer, capable of outputting up to 120VAC. A 5A fuse was placed between the heaters and the transformer to prevent overloading of the heaters, and to provide safety.

The top side of the aluminum plate was covered with polyimide tape to create the build surface, in lieu of using the polycarbonate plate which would warp at elevated temperatures. Temperature sensitive stickers were placed on the top side of the heated build platform for a general reference of the platform's temperature. For more accurate measurement of the platform temperature, a 100 ohm platinum resistive thermal device (RTD) was used in conjunction with a Minco CT-325 temperature controller to measure the temperature at the centre of the plate.

While the CT-325 controller is capable of actively controlling the temperature of the build platform when used with a solid state relay, however in the current configuration it was only used for measuring the temperature of the platform. Temperature control was accomplished by manually adjusting the variable transformer until the desired steady state temperature was achieved. Testing showed that a build platform temperature of approximately 100°C provided good adhesion between the ABS and the build platform. Higher temperatures not only required more energy, but left the ABS too soft, resulting in part deformation when removing the part from the build platform. Lower platform temperatures did not provide good adhesion and caused warping of the part. This steady state temperature coincided with an input voltage to the heaters of approximately 16 VAC, resulting in a power draw of approximately 57 watts.

8.7 Software

Various software applications are used during the process of fabricating a part on the RepRap Mendel. The process for creating a part is as follows:

1. Design the 3-dimensional part using computer-aided (CAD) design software (such as ProEngineer) and export the file into the stereolithography (.STL) file format.
2. Generate machine code (G-Code) instructions that the printer uses to create the part.
3. Import G-code to the printers graphical-user interface (GUI). Prepare printer for printing part, i.e. pre-heat extruder, zero axes. Instruct printer to begin part fabrication.
4. Printer firmware interprets G-code and controls motion in each axis as well as extruder heat and feed rate to fabricate part.

In general, each step in the process involves independent software packages with common file formats used in between each package. The software packages used for this research are described in the subsequent sections.

8.7.1 Computer-Aided Design (CAD) Software

Any computer-aided design (CAD) software capable of exporting parts in the stereolithography (.STL) format may be used to fabricate parts on the RepRap Mendel. Initially, ProEngineer Wildfire 3.0 was used to create 3-dimensional models of the wings for printing. ProEngineer is an advanced solid modeling program capable of creating

complex parts and assemblies and is available to all Mechanical and Aerospace engineering students at Carleton.

However, because ProEngineer is a commercial software package, obtaining a license for installation and use of this software was an issue, and presented additional cost. Furthermore, it was often tedious to make parametric models of wings, where only one dimension needed to be changed between each part (i.e. vein angle). Therefore, a free and open-source CAD program called OpenSCAD was used for creating part models.

OpenSCAD is a script-based solid modeling program which allows simple parametric models to be created with relative ease. Parts are generally created through the use of geometric primitives, where more simple geometries are either added to or subtracted from each other as extrusions through Boolean operations. While it is more difficult to create complex models in OpenSCAD, it has sufficient capabilities for the simple wing designs used in this research. Various wing geometries can be created by simply changing a few parameters within the script (i.e. vein thickness and angle).



Figure 8-6. Simple wings designed using OpenSCAD.

8.7.2 G-code generator

There are several software tools available for generating G-code from the STL part file for use on the 3-D printer. The RepRap Host software and RepSnapper (described further

in section 8.7.3) are two open-source GUIs that allow the user to import either one or multiple STL part files and convert them to G-code instructions. However, these programs do not offer a great deal of flexibility over how the G-code is written and how the part will be printed. The basic parameters include print speed, infill density, filament thickness, and extruder temperature. An example of some typical G-code instructions sent to the printer. For even simple parts, the G-code instructions can consists of hundreds or thousands of lines of code.

Table 8-2. Example of G-code used by the RepRap printer

G-code line	Instructions
G21;	Set units to millimeters
G28;	Zero all axes
M108 S190;	Set extruder temperature to 190°C
G4 P200;	Stay at current position for 200 milliseconds
G1 F1500;	Set extruder feed rate to 1500mm/minute
G1 X25 Y14.5 E28 F3000;	Move to position (25,14.5) while extruding 28mm of filament and accelerating the feed rate to 3000mm/minute
M0;	Stop and shut down all motors and heaters

One of the most powerful tools available for generating G-code for 3-D printers is a free and open-source application called Skeinforge. Skeinforge is based on the Python programming language and offers a great deal of flexibility and customization of the G-code.

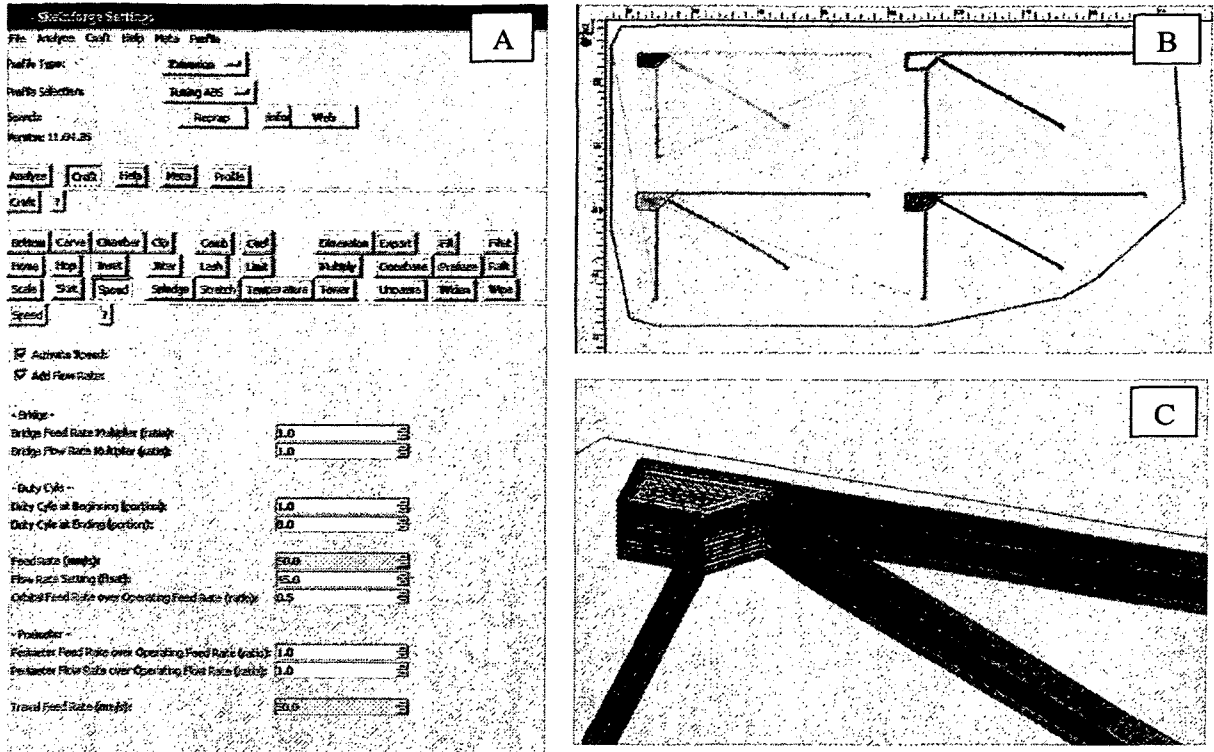


Figure 8-7. Skeinforge screenshots, including the user interface (A), as well as 2-D (B) and 3-D (C) representations of the extruder tool paths

These programs are designed for fabricating “typical” three-dimensional objects, where the border, or perimeter, of the part is printed first, and then filled with an infill pattern. The infill is typically accomplished by laying down parallel lines within the perimeter at a given angle with respect to the printer coordinate system. On the subsequent layer, the infill lines are deposited at an angle perpendicular to the previous infill direction, as shown in Figure 8-8.

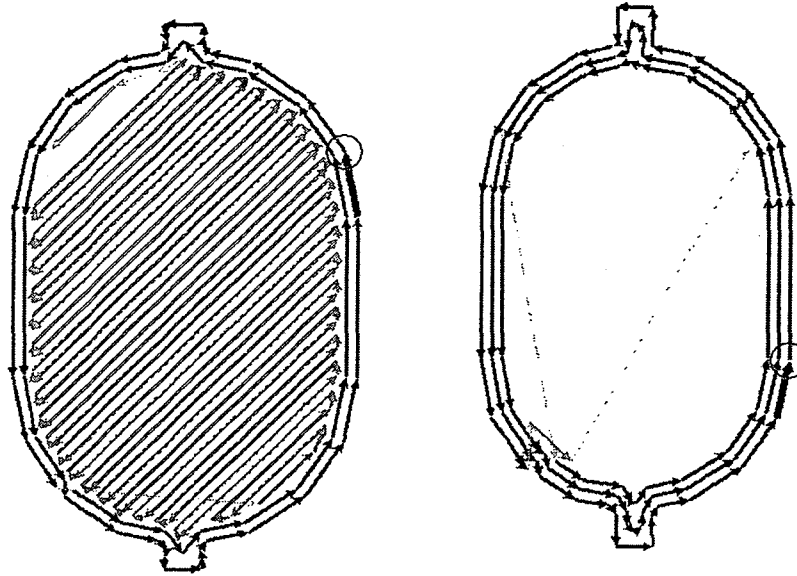


Figure 8-8. Tool paths of two layers deposited in sequence for a typical part, showing the border and infill pattern

When printing wings with thin features such as veins, these programs always try to print the border first, then print the infill. Even if the vein width is as wide as the deposited filament (i.e. one printed line), the software will automatically print two lines, as illustrated in Figure 8-9, in order to maintain a closed loop around the part perimeter. In the case of the RepRap host software, it will also try to infill between these lines. The result is a vein of twice the desired width. Consequently, the minimum vein width is limited to twice the deposited filament diameter (approximately 1.2 mm, or 0.05 in). Furthermore, if features in the part model are too thin or small, the G-code generating software will ignore these features and they will not be created in the part. The lower limit is dependent on the software being used, but is typically around 0.5 to 1 mm (0.02 to 0.04 in). Therefore, minimum feature size can be more dependent on the G-code generating software than on the capabilities of the printer itself.

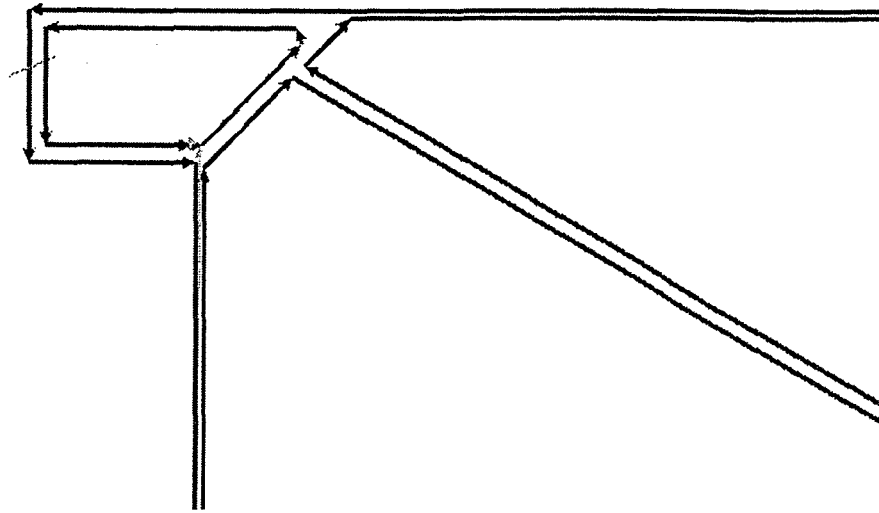


Figure 8-9. Tool path for a wing with thin veins, showing two path lines for each vein in order to maintain a closed loop around the part

One way to circumvent these issues is to develop a program, or modify an existing program, specifically for printing small features such as wing veins. This would allow the printer to deposit single lines of material where necessary, rather than closed loops of material. This program may even be combined with the 3-D modeling program, similar to OpenSCAD, which generates G-code directly from the model, without having to create the CAD model itself. The use of open-source software as a basis can facilitate the development of custom software, since the source code is freely available to modify; however, this work was outside the scope of this research and will be discussed further as a recommendation for future work.

8.7.3 Printer GUI

The printer graphical user interface (GUI) is the main link between the user and the printer. The GUI allows parts or G-code to be loaded and sent to the printer. It also allows the user to manually control or set the coordinates of the extruder, as well as set

and monitor the extruder temperature. There may also be a 3-dimensional rendering of the tool paths, depending on the program used.

The GUI application provided with the RepRep code is called RepRap Host. It is a Java-based program which allows part files or G-code to be loaded into the program and to be sent to the Mendel for printing. There is also manual control of each axis, as well as temperature controls. However, the RepRap Host program was very prone to freezing and crashing, particularly if the user attempted to perform more than one action at a time. This required restarting both the printer and the RepRap Host application.

Another free and open-source GUI application, called RepSnapper, is much more stable, while offering the same functionality as the RepRap Host software.

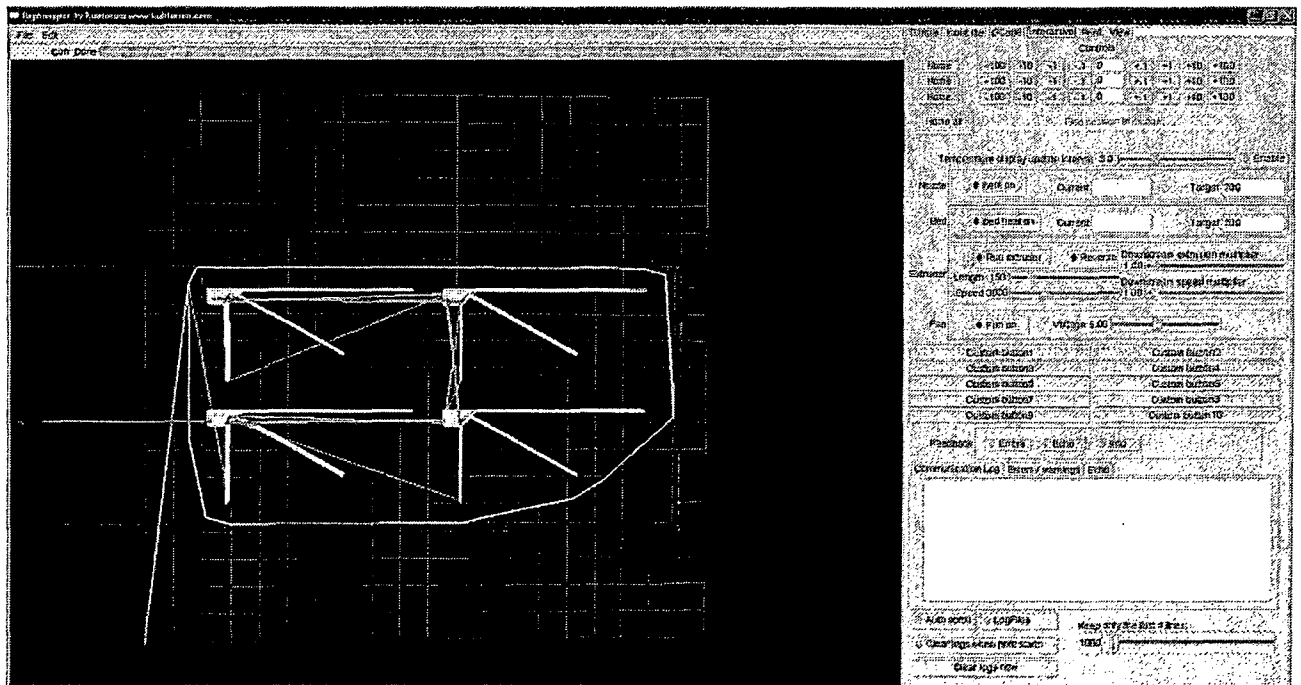


Figure 8-10. RepSnapper graphical user interface, showing a rendering of the G-code tool paths

8.7.4 Printer firmware

The printer firmware interprets the G-code sent from the computer to the motherboard and translates them into specific actions for the printer, such as control of each axis' stepper motor and heating of the extruder barrel. The firmware is typically edited and uploaded to the motherboard via the Arduino integrated development environment (IDE). While the majority of the firmware code is not modified by the user, there are several user-defined parameters that are used for tuning and calibrating the system. These parameters are described below.

8.7.4.1 Printer configuration

The user must specify which electronic hardware version is being used, since the input and output assignments may be different for different hardware versions. The user also specifies other configuration parameters, such as how many end stops are used (i.e. at “zero” only, or at zero and the maximum travel distance).

8.7.4.2 Axis travel calibration

For each axis, the user specifies a “steps per millimeter” value. This tells the firmware how many steps the motor must turn to achieve the commanded travel distance. This value is dependent on the type of motor being used and printer geometry, i.e. the diameter of pulleys used. The user also specifies the maximum travel distance for each axis to prevent damage to the printer if a large travel distance is commanded.

8.7.4.3 Extruder calibration

Similar to the axis travel calibration, the user must specify a “steps per millimeter” of extruded material. This value is more complicated to determine, because it is dependent

on the extruder motor, the gear ratio, and the nozzle diameter. Furthermore, the data regarding the thermistor used for measuring the extruder temperature must also be given, since the correlation between the measured resistance value and the temperature is dependent on the type of thermistor used.

8.8 Printer setup

This section describes the setup and testing of the RepRap Mendel 3-D printer, including the calibration procedure used to tune the various parameters. Proper calibration and set-up of the printer is essential to achieving satisfactory prints, and therefore requires a great deal of testing. Thorough testing is also required to properly define the various parameters used in both the firmware and the G-code generating software.

8.8.1 Calibration

A first approximation for each user-defined parameter was obtained from the stock settings, or as recommended by other RepRap users. However, due to variability in each user's setup, further refinement of these values was required.

8.8.1.1 Axis travel

Calibration of axis travel is important for obtaining dimensionally accurate parts. Axis travel calibration was performed by commanding each axis to move a prescribed distance via the GUI. The actual distance travelled is measured, and the "steps per millimeter" value in the firmware is multiplied by the ratio of desired travel to actual travel. This process is repeated until the commanded distance equals the actual travel distance.

8.8.1.2 Extruder calibration

Calibration of the extruder was performed in the same way as the travel distance. By commanding the extruder to feed a prescribed amount of filament into the extruder and measuring the actual length of filament, the correct value was obtained.

8.8.1.3 Extruder feed rate

The extruder feed rate is one of the most critical parameters. It determines how much filament needs to be fed into the extruder to output a given amount of material. This value is dependent on the filament material, and is therefore external to the firmware. Specifically, it factors in “die swell” of the material – how much the material expands after it is extruded. For instance, while the nozzle diameter is 0.5mm, the diameter of the actual filament deposited can actually be 0.65mm due to die swell.

8.8.1.4 Temperature

Determination of the optimal print temperature was achieved by printing test parts and running the extruder at a range of temperatures. If the temperature is too low, the filament will not be in a completely molten state when deposited and will not fuse to either the build platform or to preceding layers of material. Low extrusion temperatures can also cause the extruder to clog and jam. If the temperature is too high, the filament can burn and harden inside the extruder, also causing the extruder to clog. For PLA, the optimal print temperature was 190°C (374°F), while the optimal temperature for ABS was 235°C (455°F). Temperatures within 5°C (9°F) above or below these values did not appear to affect print quality.

Additional temperature values can be set for different parts of the build. For example, a higher temperature can be used for the first layers of the print to ensure good adhesion between the build platform and the base layers, while lower temperatures can be used when a small cross sectional area is being printed, allowing the deposited material to cool faster before the next layer is deposited.

8.8.1.5 Travel speed

Travel speed of each axis must be properly selected in order to achieve good print quality. Travel speed can be independently specified for travel during deposition, and travel when material is not being deposited. The travel speed of the x- and y-axis during deposition can affect print quality. If the travel is too slow, too much material is deposited and the deposited lines are thick and non-uniform. If the extruder rate is made correspondingly low, the extruder motor moves too slowly and this can result in motor stall. Furthermore, slow travel speeds result in longer print times. On the other hand, high travel speed can cause lines of deposited material to be stretched out and too thin. The motors also have to work harder to overcome inertia when changing direction quickly. This can often lead to missed steps by the motors, which affects the printer's extruder position estimate and can create dimensional inaccuracies in the part. The travel speeds were adjusted by varying parameters through a series of test prints in order to achieve good print quality with reasonable print times.

8.8.1.6 Extruder-platform gap

The distance between the extruder nozzle and the build platform proved to be a critical parameter for obtaining good results. If the nozzle is too close to the build platform, the filament will be flattened by the nozzle. This can also lead to build-up of plastic on the

nozzle and clogging. However, if the nozzle is too high, the filament will tend to curl when deposited, leading to wavy lines or areas where the filament fails to fuse to the previous layer. The tolerance between the minimum and maximum height is approximately 0.5 mm (0.02 in). The height is set mechanically by adjusting the z-axis end stop such that the $z=0$ point lies at the desired height above the build platform.

Furthermore, the build platform must be perfectly level with respect to the printer's xy-plane. If the build platform is not level, the distance between the nozzle and the build platform will vary across the build area. The platform is adjusted by four bolts at each corner of the build platform.

Mechanical adjustment of both the z-axis end stop height and the build platform was tedious and difficult to achieve precise and accurate positions. The addition of an electronic range finder for precisely and accurately determining the z-axis position is recommended. The measured range should be sent to the GUI through the motherboard in order to adjust the extruder-platform gap, and thus the z-axis home position, through the user interface.

8.8.2 Test parts

Various test parts were used to test and adjust the various printer parameters until satisfactory results were obtained. The most commonly used test part was a 25.4 mm x 50.8 mm x 6.35mm (1 in x 2 in x 0.25 in) rectangular block. This was a simple part with specific dimensions that could be verified. It also had simple features and straight lines, allowing the extruder feed rate and travel speeds to be adjusted in order to achieve straight lines. A circular part with holes of various diameters was also used to test how

the machine printed curved lines of various radii. Once the basic settings were determined, more complicated parts were printed to test the printer's ability to print taller parts with complex geometries such as overhangs. Some of these test parts are shown in Figure 8-11.



**Figure 8-11. Example test parts used for calibrating and optimizing printer settings.
Scale bar in each image represents 1 cm (0.4 in)**

9 Prototype Wing Design and Manufacture

Several prototype wings were successfully “printed” using the RepRap Mendel in a variety of materials, planform shapes, dimensions, and vein configurations. The utility of rapid prototyping was demonstrated, as it has allowed many different designs to be printed in less than an hour. This chapter outlines the process and materials used for fabricating wing prototypes, followed by a description of the prototype wing designs.

9.1 Fabrication process

The fabrication process for a set of prototype wings was performed as follows (see Figure 9-1):

1. STL file preparation
 - a. Wing is designed in computer-aided design software and exported as an .STL file.
 - b. .STL file is uploaded to the g-code generating software, settings are adjusted as necessary, and g-code for wing print is generated.
 - c. G-code is uploaded to printer graphical user interface (GUI) software
2. Printer preparation
 - a. Heated build platform is pre-heated to desired temperature (5-10 minutes)
 - b. Extruder is pre-heated to desired temperature (5-10 minutes)
 - c. Membrane material is applied to build platform, ensuring no wrinkles.
Tape is used to secure membrane material to build platform, if necessary
 - d. Extruder is primed by running the extruder for several seconds
 - e. All printer axes are moved to their zero (“home”) positions

f. Print is started via the GUI software

3. Post-print

- a. The sheet of membrane material, with deposited wing veins, is carefully removed from the build platform
- b. The sheet containing the wing(s) is immediately placed between two flat surfaces and allowed to cool completely, if necessary, to prevent warping
- c. Once cooled, each wing is carefully cut from the membrane material sheet using a sharp knife

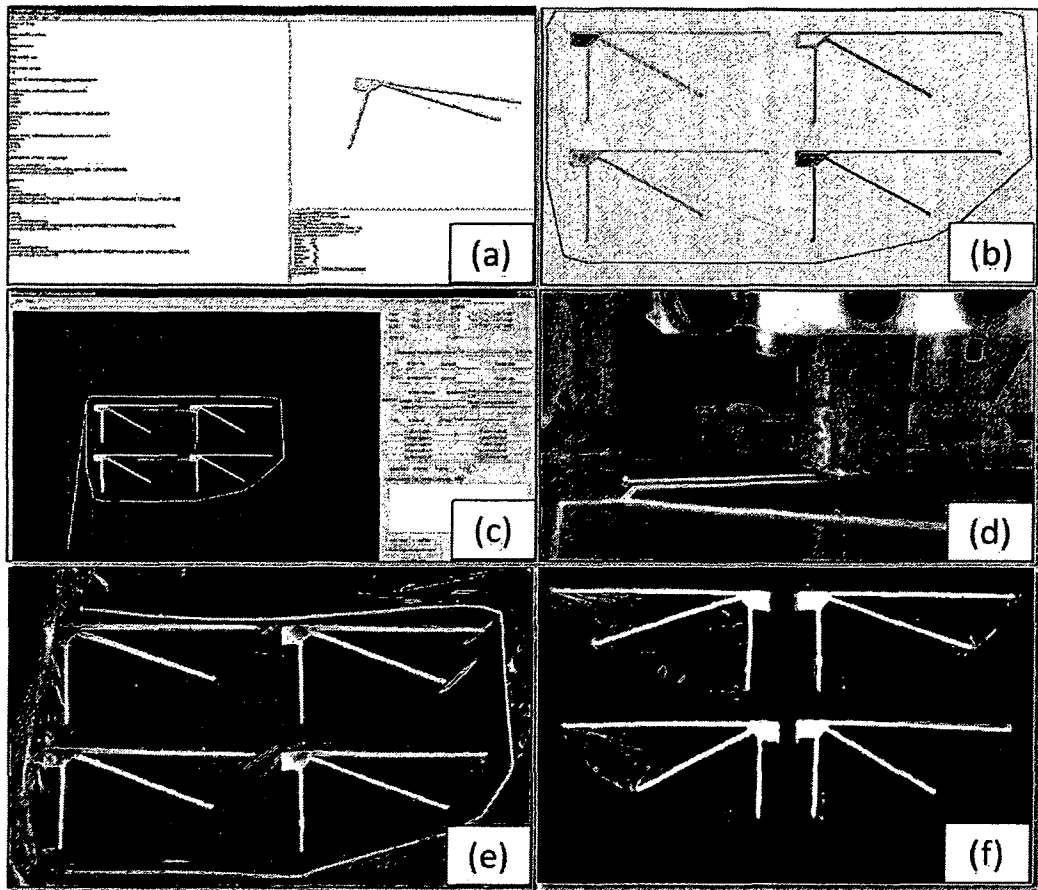


Figure 9-1. Wing fabrication process: (a) Wing designed in OpenSCAD, (b) Wing model converted to G-code, (c) G-code uploaded to printer GUI, (d) Wing printed using RepRap, (e) Printed wings removed from printer, (f) Wings cut from membrane material.

The preparation time for a print is approximately 10 minutes, during which the printer pre-heating and file preparation steps can be performed concurrently. Depending on the number and complexity of wings, the actual print process can take anywhere from 30 seconds to 5 minutes. Post-processing of the wings takes approximately 5 minutes. Therefore, the total process time for a set of wings is approximately 15-20 minutes, however it can be as low as 5 minutes when printing only one or two wings and pre-heating has already been accomplished or is not required.

9.2 Materials

Various material options are available for the wing veins and membrane. The wing veins are the primary structural element of the wing and must be made from materials with a suitable balance of weight, stiffness, flexibility, and durability; whereas the membrane material should be thin, lightweight, and flexible; therefore, material selection for the veins and membrane were considered independently.

9.2.1 Veins

Material selection for the veins was restricted by the printer's capabilities and its limited print material options. Based on prior testing (Chapter 8), polylactic acid (PLA) and acrylonitrile butadiene styrene (ABS) were shown to be feasible materials for fabricating the wing structure because they could be used reliably with the printer. The material was extruded through a 0.5 mm (0.020 in) nozzle, giving a filament thickness of approximately 0.6-0.7 mm (0.024-0.028 in). Veins may consist of one, two, or three layers of material, depending on the desired stiffness.

9.2.2 Membrane

Selection of the wing membrane material is less dependent on the specifications of the rapid prototyping machine; however, it was important to incorporate the application or deposition of the membrane material into the process with minimal additional labour and material requirements (i.e. adhesives).

The solution was to select a film that could be applied on the build platform, and deposit the molten polymer vein material directly onto the membrane. With proper material thermal properties and build conditions, the membrane material and vein material fuse together, eliminating the need for an additional process to adhere the membrane to the veins, which would likely require manual labour and the addition of an adhesive.

The primary membrane material tested in this research is polyvinylidene chloride (PVDC), which is commonly used as plastic “cling” wrap under the trade name “Saran”. The PVDC film has a thickness of approximately 50 μ m (0.002 in), and is both very flexible and durable, which makes it an attractive membrane material. It is also readily commercially available at very low cost (approximately \$0.10/m² or \$0.01/ft²). PVDC has a melting temperature of approximately 160°C (eFunda, Inc., 2011), which is lower than that of ABS and PLA, allowing the vein material to fuse to the PVDC film during printing. Polyetherether ketone (PEEK) film was also used as a membrane material in a similar manner. Results from these tests are described in the following sections.

Table 9-1. Properties of materials used in prototype wings

	ABS ¹		PLA ^{1,2}		PVDC ^{3,4,5}		PEEK ¹	
Tensile Strength	40 MPa	5.8 ksi	53 MPa	7.7 ksi	24 MPa	3.5 ksi	100 MPa	14.5 ksi
Tensile Modulus	1.9 GPa	275 ksi	3.5 GPa	508 ksi	170 MPa	24.7 ksi	3.6 GPa	522 ksi
Flexural Strength	96.5 MPa	14 ksi	83 MPa	12 ksi	-	-	170 MPa	24.7 ksi
Flexural Modulus	2.07 GPa	300 ksi	4 GPa	580 ksi	-	-	4.1 GPa	595 Ksi
% Elongation	20%		6%		400%		50%	
Melting Temperature, T _m	Amorphous		160°C	320 °F	160°C	320°F	334°C	633°F
Glass Transition Temperature, T _g	100°C	212°F	54°C	129°F	-17°C	1.4°F	146°C	295°F
Processing Temperature	177-260°C	350-500°F	170-200°C	356-392°F	160-199°C	320-390°F	-	-
Heat Deflection Temperature	104°C	220°F	65°C	149°F	70°C	158°F	160°C	320°F
Specific Gravity	1.05-1.2		1.24		1.63		1.32-1.44	

Sources: ¹www.makeitfrom.com, ²ultimachine.com, ³Dow Chemical, ⁴www.eFunda.com, ⁵www.azom.com

9.3 First wing prototypes

The first fabricated prototype wings were based on a real locust hind wing, maintaining the same shape as the wing, with four veins evenly distributed across the wing and a rigid perimeter, as shown in Figure 9-2. These prototypes were used primarily for proof-of-concept trials and testing of the manufacturing process with different material configurations. The resulting wings were too stiff for flapping-wing MAV applications due to the rigid perimeter, and therefore these wings were not considered for aerodynamic testing. Different vein and membrane material combinations were tested, and are described in the following subsections.

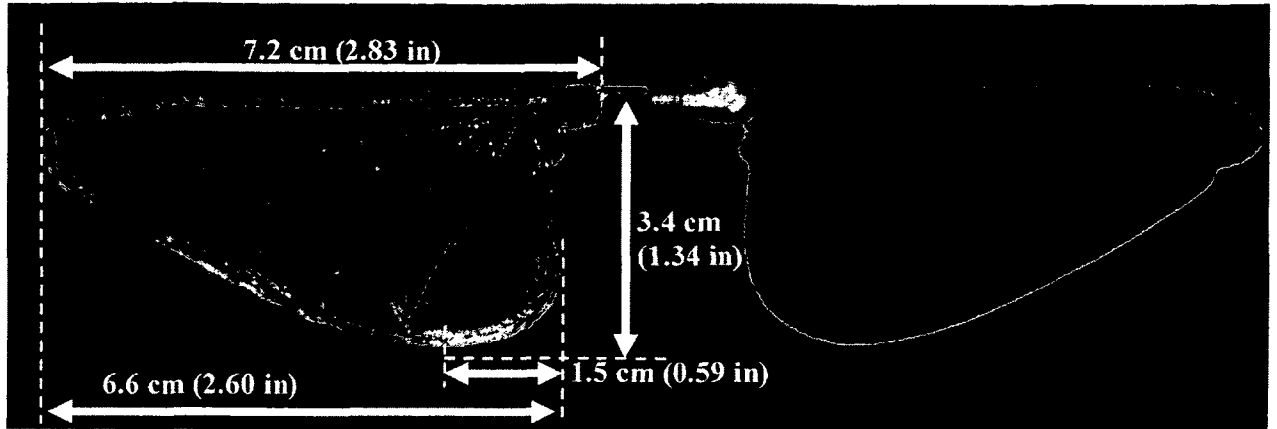


Figure 9-2. Printed prototype wing (left) and rigid wing (right)

The wing planform shape was based on rigid polystyrene wings used for aerodynamic trials by the Carleton University Insect Flight Group. These are a 2:1 scaled-up planform representation of a real locust hind wing, as shown in Figure 9-3, having a total wing length of 7.2 cm (2.83 in) and a maximum chord of 3.4 cm (1.34 in). The 3-D printed wings were designed to have equivalent dimensions to the rigid wings so that a direct quantitative comparison between the rigid wings and the flexible printed wings could be performed during aerodynamic testing.

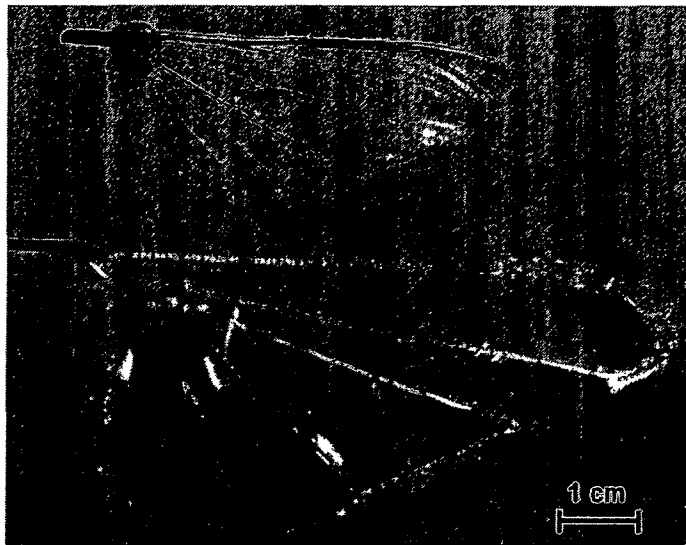


Figure 9-3. Comparison of a real locust hind wing (top) and a 3-D printed prototype wing (bottom)

9.3.1 PLA / PVDC

The first wing prototypes that were fabricated consisted of PLA veins printed directly onto the PVDC film membrane, as shown in Figure 9-2. The adhesion between the PLA and the PVDC was poor, resulting in the membrane detaching from the veins with little to moderate applied force. In some cases, there was no adhesion at all between the veins and the membrane.

In order to improve durability, the wings were printed without the membrane film, and the membrane was bonded to the veins by applying a spray adhesive. While this improved the adhesion between the veins and the membrane, it was not considered durable enough to withstand the abuse of flapping flight. Furthermore, this step added additional manual labour to the process and was a departure from the aim of this research.

It was observed that poor adhesion between the deposited PLA and the PVDC film occurred more often at low ambient temperatures (i.e. when testing during the winter months). The likely cause for the poor adhesion was that the molten PLA was cooling too rapidly upon deposition, and that the temperature of the PVDC film was too low. Consequently, the PVDC was likely not heated past its melting temperature upon PLA deposition, and therefore fusion between the PLA and PVDC did not occur.

The problem was remedied by pre-heating the build platform plate and PVDC film in a convection oven to approximately 75°C for 10 minutes. Prior to printing, the PVDC film was cleaned with isopropanol to remove any contaminants from the film. The resulting wings showed better adhesion than when printed at room temperature, however the wings still lacked the required durability.

A heated build platform was later integrated into the RepRap Mendel as described in Chapter 8. This heated platform allowed the PVDC film to be pre-heated and held at an elevated temperature throughout the printing process. The resulting wings showed good adhesion between the PLA veins and the PVDC membrane material, with good durability.

9.3.2 PLA/ PEEK

A set of prototype wings was fabricated using PLA as the vein material and polyetherether ketone (PEEK) film as the membrane material. In order to achieve adequate adhesion between the PLA and the PEEK, the build plate and the PEEK film were pre-heated to 70°C in an oven. The resulting wings did not have a durable bond between the PLA and PEEK, with the membrane separating from the veins under moderate applied force. Furthermore, the wing membrane was relatively stiff compared to the PVDC film, and was more comparable to thin paper in terms of flexibility. Therefore, no further testing with PEEK membrane material was performed.

9.3.3 ABS / PVDC

Wing prototypes were also printed using ABS as the vein material and PVDC as the membrane material. With the build platform and membrane material at room temperature (approximately 19-23°C or 66-73°F), the wings showed very good fusion between the ABS and PVDC. The membrane could not be separated from the veins without damaging the membrane, resulting in a very durable wing. The issue, however, with printing the wings at room temperature was that the wings had a tendency to warp upon cooling due to the mismatch in coefficient of thermal expansion between the film and veins, as well as asymmetric cooling of the deposited plastic, where to the upper surface of the wings

cools faster than the bottom surface. This resulted in curved wings as shown in Figure 9-4. It remained to be determined through the testing described in Chapter 10 whether this curvature caused any measureable beneficial or adverse aerodynamic effects.



Figure 9-4. Warped wing resulting from shrinkage of the ABS during cooling

Warping of subsequent wings was prevented by printing wings with the heated build platform heated to approximately 100°C (212°F). At this temperature, the ABS remains above its glass transition temperature and therefore warping does not occur. Upon removing the wings from the build platform, they were immediately placed between two flat surfaces, such as under a heavy book on a table, in order to allow the wings to remain flat until cooled to room temperature.

The ABS material was consistently easier to print with than the PLA, as it required lower extrusion force and was less prone to clogging in the extruder. Furthermore, printing with ABS provided an excellent fusion bond with the PVDC membrane material, resulting in durable wings without the need for additional adhesive application. Therefore, further testing was performed with ABS and PVDC; however, a more thorough investigation using PLA and other materials is recommended, as these materials may offer better thermal, mechanical, and/or physical properties in the final wings.

9.4 Simplified wing design

The first wing prototypes allowed for the testing of the wing fabrication process and to evaluate the use of different materials. Based on these initial prototypes, the use of ABS as a vein material and PVDC film as the membrane material provided the most reliability in fabrication, while possessing desirable properties for flapping wings such as stiffness and durability. However, the wing design was rather complex for use as a starting point for further aerodynamic and structural testing of the wings. Applying changes to the model parameters such as the number of veins, wing span, and aspect ratio were difficult due to the curvature of the leading and trailing edges. The wing shape was also challenging to model using OpenSCAD (see Chapter 8). Therefore, the wing planform was simplified to have a straight leading edge and veins, while approximating the dimensional properties of the initial “biomimetic” planform such as span, aspect ratio, area and second moment of area. Furthermore, the rigid border around the wing was eliminated to provide better flexibility. The resulting wing planform can thus be considered “bio-inspired”.

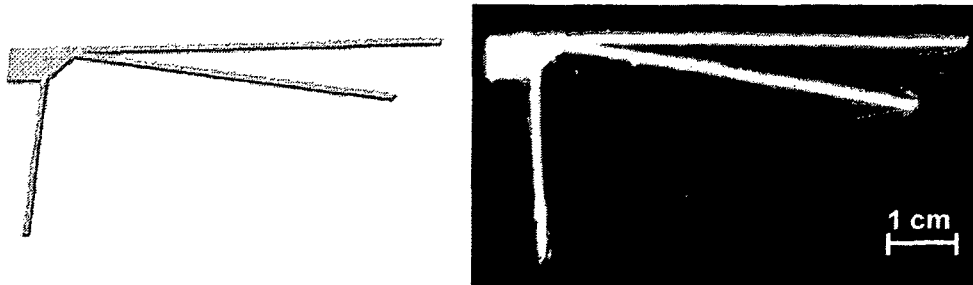


Figure 9-5. OpenSCAD model (left) and wing printed from ABS onto PVDC film (right)

Several wing design variations were created in order to perform a parametric study of different wing geometries. These include wings with no internal veins, single veins at

angles of 10° , 20° , and 30° , multiple veins, and insect-scale wings. Some examples are shown in Figure 9-6.

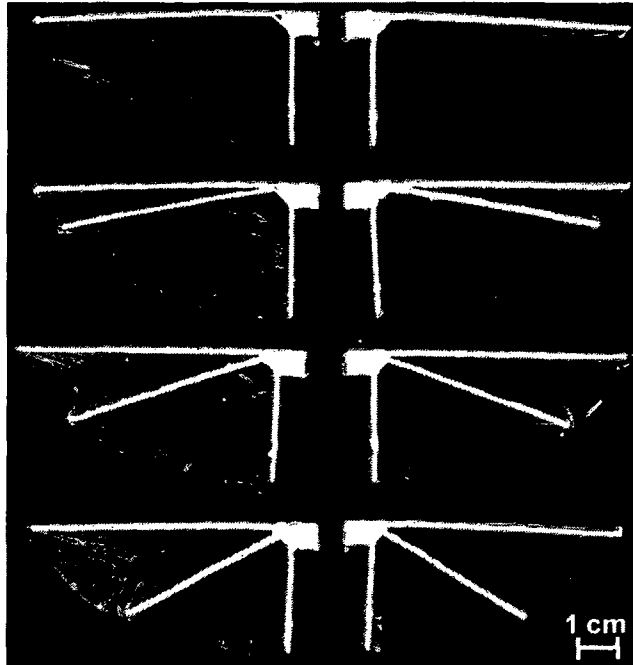


Figure 9-6. Wing prototypes based on simplified planform

The simplified wings were used to perform structural and aerodynamic testing in order to achieve the following:

1. Determine the stiffness distribution of different wing design variations
2. Evaluate and compare the aerodynamic properties of each wing design
3. Assess the repeatability of the manufacturing process by comparing structural and aerodynamic properties of wings of the same design
4. Assess the feasibility of the design, manufacturing, and testing process for parametric design studies

Details and results of these tests are described in the next chapter. Overall, the use of the RepRap Mendel for has been shown to be a feasible process for fabricating flapping wing

prototypes for MAVs. The use of script-based modeling tools such as OpenSCAD allowed for parametric design changes to be made easily and transferred from the solid model to the production of the physical component quickly. Furthermore, the overall design and manufacturing process has proven to be relatively fast compared to other processes, with fabrication times as low as 5 minutes, while also having very low overall system and material cost. Finally, a novel method of directly fusing the vein and membrane materials during the printing process has been developed, reducing the amount of manual labour required to fabricate the wings while simultaneously eliminating the need for adhesives. The next chapter presents the aerodynamic and stiffness testing of the 3-D printed wings in order to quantitatively assess their performance and to compare the different wing designs.

10 Wing Testing

This chapter describes the testing performed on real insect wings and the 3-D printed prototype wings in order to assess both the manufacturing process as well as the suitability of the printed wing design. These tests included spin testing, which allowed for analysis of the aerodynamic performance of the wing designs, as well as stiffness distribution measurements, which allowed for the correlation between aerodynamic and structural properties.

The tests described in this chapter aimed to achieve the following objectives:

1. Evaluate and compare the aerodynamic properties of each wing design;
2. Assess the repeatability of the manufacturing process by comparing structural and aerodynamic properties;
3. Determine the stiffness distribution of different wing designs; and
4. Assess the feasibility of the design, manufacturing, and testing process for parametric design studies.

10.1 Spin Testing

The aerodynamic performance of each wing was evaluated using a spin test around a fixed axis. The motion of the revolving wing replicates the down stroke of a flapping wing. During the down stroke of the flapping cycle, approximately 60% of the wing's total lift is generated (Usherwood & Ellington, 2002). This eliminates the need for complex flapping mechanisms to reproduce the entire flapping cycle. Although the spin

testing described here does not provide a complete representation of aerodynamic performance during all phases of flapping flight, it did serve to provide a suitable comparison between various wing designs, as well as between real and artificial wings.

10.1.1 Determination of Vertical Lift Coefficient

The lift performance of the wings was evaluated based on the coefficient of vertical lift, C_V , in the same way airfoils are evaluated based on the coefficient of lift, C_L . Since flapping wings generate both lift and thrust, the net force is broken into its vertical and horizontal components (C_V and C_H respectively). Because the spinner apparatus used in these tests was only capable of measuring vertical force, only C_V is used. In order to measure the coefficient of horizontal lift, C_H , one would need to measure the torque applied to the wing. While torque measurement would result in a more complete aerodynamic assessment which would allow for the calculation of net lift, thrust, and drag, a more complicated test setup is required and was outside the scope of this work. Evaluation of wing designs using only C_V still allowed for a quantitative assessment of the fabricated wings and comparison with real insect wings.

The coefficient of vertical lift is derived in the same manner as C_L for a conventional airfoil, where

$$C_L = \frac{L}{\frac{1}{2}\rho v^2 S} \quad (10.1)$$

In the above equation, L is lift force, ρ is air density, v is free stream velocity, and S is wing planform area. In the case of a spinning wing, the equation for vertical lift coefficient becomes:

$$C_v = \frac{L}{\frac{1}{2}\rho\omega^2\bar{S}} \quad (10.2)$$

In this case, ω is the speed of rotation in radians/second, and \bar{S} is the second moment of area of the wing or wings, depending on how many wings are mounted on the spinner apparatus. The second moment of area is important because it accounts for the fact that the airspeed is greater at the wing tip than at the root, and therefore the wing tip will have a greater effect on the overall lift for a given chord length.

The rotational velocity used during the test was determined based on the typical Reynolds number of 5600 experienced by a real locust, weighing approximately 2g (0.7oz). For comparison, the Reynolds number for a conventional fixed wing airplane such as a Cessna 172 with a maximum takeoff weight of 1043 kg (2300 lbs) is approximately 5×10^6 – approximately 1000 times higher (McIver, 2003). For a rotating wing, the Reynolds number is calculated by:

$$Re = \frac{\bar{c} \cdot \bar{u}}{\nu} \quad (10.3)$$

where \bar{c} is the average wing chord, \bar{u} is the wing tip velocity, and ν is the kinematic viscosity of air (Ellington, 1999). Since

$$\bar{u} = \omega \cdot R \quad (10.4)$$

where R is the wing radius, or wing length from the centre of rotation to its tip, thus the rotation speed can be calculated by

$$\omega = \frac{Re \cdot v}{\bar{c} \cdot R} \quad (10.5)$$

Given that the average chord of the 3-D printed wings was 25.4 mm (1.0 in) and the wing length, or radius, was 66 mm (2.6 in), the required rotational frequency for the 3-D printed wings was approximately 8 Hz to give $Re=5600$.

10.1.2 Experimental Set-up

The spin testing apparatus was acquired from the Carleton University Department of Biology's Insect Flight Group, and is based on the apparatus used by Nachtigall (1981) in a study of rotating model locust wings, and later by Usherwood and Ellington (2002, 2002a) in their study of the aerodynamic performance of the hawkmoth (*manduca sexta*) wing. Additional modifications to its use in the present project were also undertaken and will be described below.

The apparatus, shown in Figure 10-1 and Figure 10-2, includes a wing spinner, a knife-edge fulcrum, and a precision balance. The spinner is constructed from aluminum, and houses a direct-current (DC) motor which rotates a vertical shaft. Wings are secured to an adapter attached to the top of the rotating shaft via small metallic rods bonded to the wing root. The DC motor is controlled by a speed controller which varies the input voltage to the motor, and thus motor speed, via a pulse-width modulated (PWM) signal generator. The motor rotation speed was measured using a stiff wire attached to the spinner's rotating shaft which passed through an infrared optoelectronic-switch once per revolution, as shown in Figure 10-3. The optoelectronic-switch output was monitored by

a digital oscilloscope (Tektronix, model TDS 2012), which displayed the rotation frequency in Hertz (Hz) as shown in Figure 10-4.

Lift force generated by the spinning wings was measured using a digital balance (AND, model HA-120M). Since the mass of the spinner exceeded the measurement range of the balance, a counter-weight nearly equivalent to the combined mass of the spinner and wings was placed on the opposite side of a knife-edge fulcrum. The fulcrum also helped to isolate the digital balance from vibration caused by the spinner, as well as any downwash effects from the wings during spinning. A needle extending from the counter-weighted side of the fulcrum applied the reaction force due to wing lift onto the digital balance. With the wings stationary, the digital balance measured a mass in the range of 10 to 20g, depending on the amount of counter-weight used, which was well within the balance's measurement range of 120g. The balance had a precision up to 0.0001g. By zeroing the balance at this point, the lift generated by the wings while spinning could be measured. Lift measurements were taken at least 30 seconds after starting the spinner, which allowed the wing wake to develop and reach a steady state (Usherwood & Ellington, 2002a).

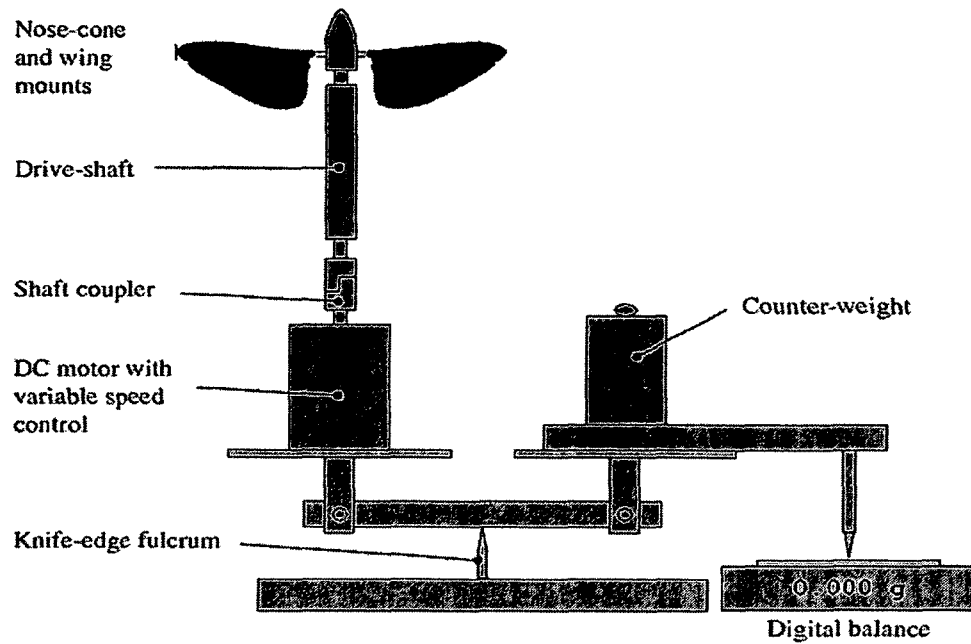


Figure 10-1. Schematic of spin test set-up (Schnackenburg, 2007)

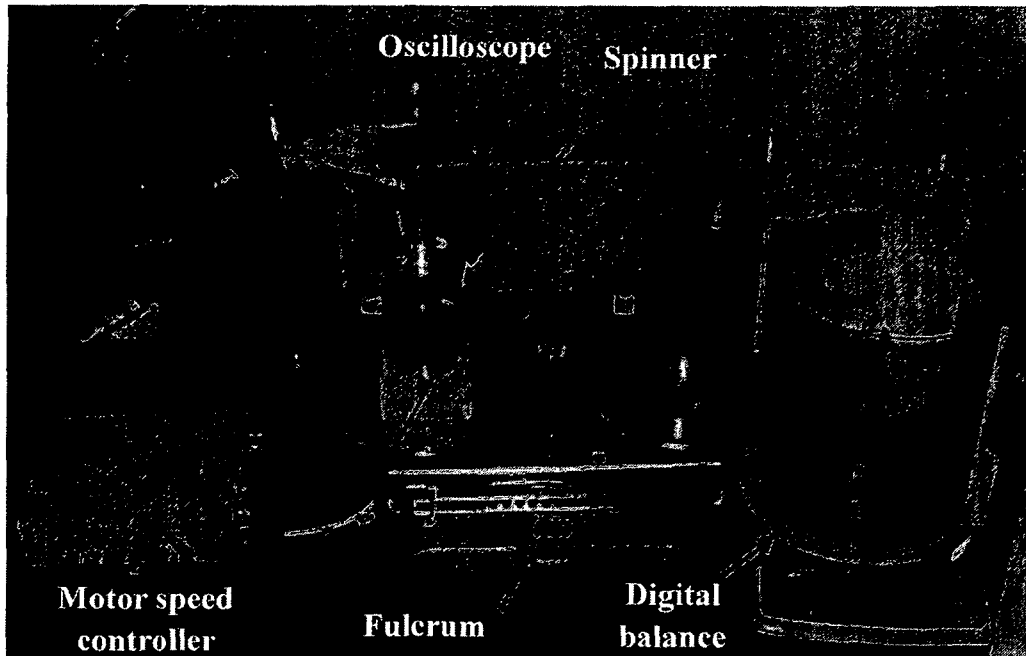


Figure 10-2. Spin test set-up

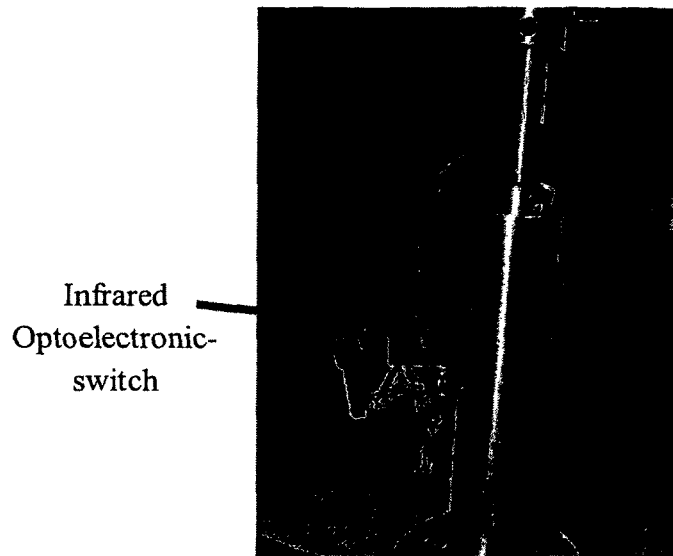


Figure 10-3. Spinner with optoelectronic-switch for frequency measurement



Figure 10-4. Screenshot of oscilloscope showing frequency measurement

10.1.3 Modifications to the test setup

Since the calculation of the coefficient of vertical lift is proportional to the square of the rotational speed (Equation 10.2), it was important to measure the spinner's rotation speed as accurately as possible. In the original design of the spin apparatus, as received from Carleton University's Insect Flight Group, the test procedure was as follows:

1. Attach an adapter to the top of the shaft which contains a small piece of stiff wire protruding perpendicularly from the shaft.
2. Using the optoelectronic-switch, measure the rotation frequency of the shaft. Adjust the motor speed using the speed controller until the desired rotation frequency is achieved.
3. Stop the motor and replace the adapter with the protruding wire with the wing-mount adapter.
4. Perform spin testing without further adjustment to the motor speed.

However, it was observed during initial testing that the motor speed did not remain constant. A test was performed to quantify the fluctuation in motor speed by monitoring the rotational speed of the motor over time. The motor was started at room temperature (approximately 22°C, 72°F) and allowed to run continuously for 50 minutes. The starting frequency was set at 8 Hz and was not manually adjusted for the remainder of the test. At the end of the test, the spinner's outer casing temperature was 24.4°C (75.9°F), measured with an infrared thermometer.

The results of the test are shown in Figure 10-5. The motor speed increases over time, likely due to the heating of the motor and reduction in oil viscosity and friction within the bearings. The frequency was relatively constant after approximately 25 minutes, with an overall increase of over 2 Hz. If not accounted for, a change in frequency of 2 Hz can introduce a 55% error in the calculation of C_V . In order to address this issue, a stiff wire was added to the spinner to allow frequency measurements to be taken while the wings are spinning. Consequently, both lift force and the corresponding rotation frequency can be more accurately measured and compared.

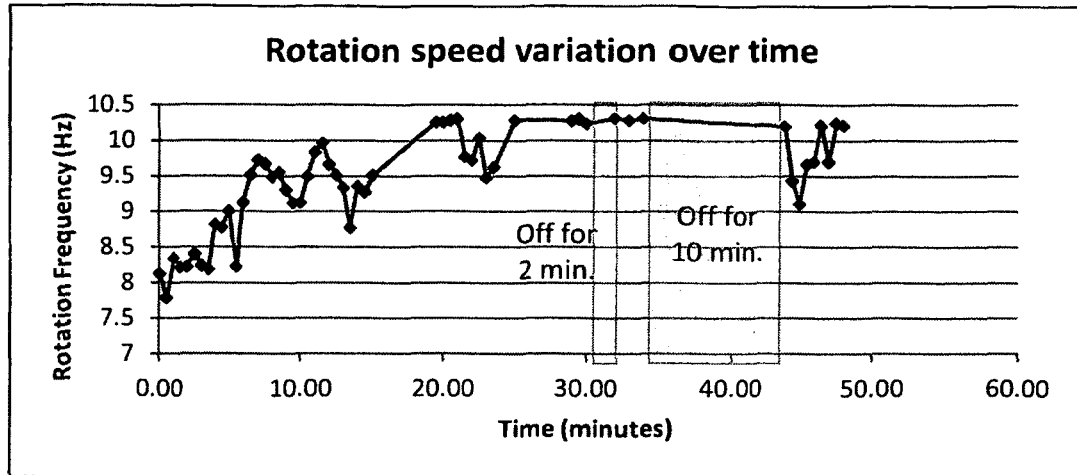


Figure 10-5. Variation in motor rotation frequency over time

Another change to the test procedure included mounting of the wings inverted on the spinner, such that the lift force vector pointed downwards, rather than upwards. This not only provided the necessary clearance to allow frequency measurements to be taken during the test with the optoelectronic-switch, but it also reduced the “ground effect” induced by the interaction between the downward wing airflow and the spinner housing, fulcrum platform, and table top on which the apparatus was mounted. In this configuration, the force resulted in a negative load value on the digital balance rather than a positive value. The effect of gravity on the inverted wings was assumed to be negligible compared to aerodynamic and inertial loads on the wings. However, it should be noted that for large and very flexible wings this assumption may not hold, since the weight of the wing itself would have an effect on the wing deformation and would therefore affect the aerodynamic performance.

10.1.4 Effect of rotational frequency

During spin testing, it was difficult to maintain the motor speed at a specific rotational frequency, which fluctuated by approximately 0.5 Hz during testing. These fluctuations

may be attributed to vibrations due to unbalanced spinning mass or friction within the spinner assembly. Therefore, it was important to evaluate the effect of rotational frequency on the performance of the wings. A wing was tested with a constant angle of attack of 40° at rotational speeds ranging from 6 Hz to approximately 14 Hz. This corresponded to a Reynolds number range of approximately 4,000 to 10,000. The measured lift force was converted to lift coefficient based on the frequency at which it was measured. The coefficient of lift values are plotted against rotational frequency in Figure 10-6, while the increase in lift force with increasing Reynolds number is shown in Figure 10-7.

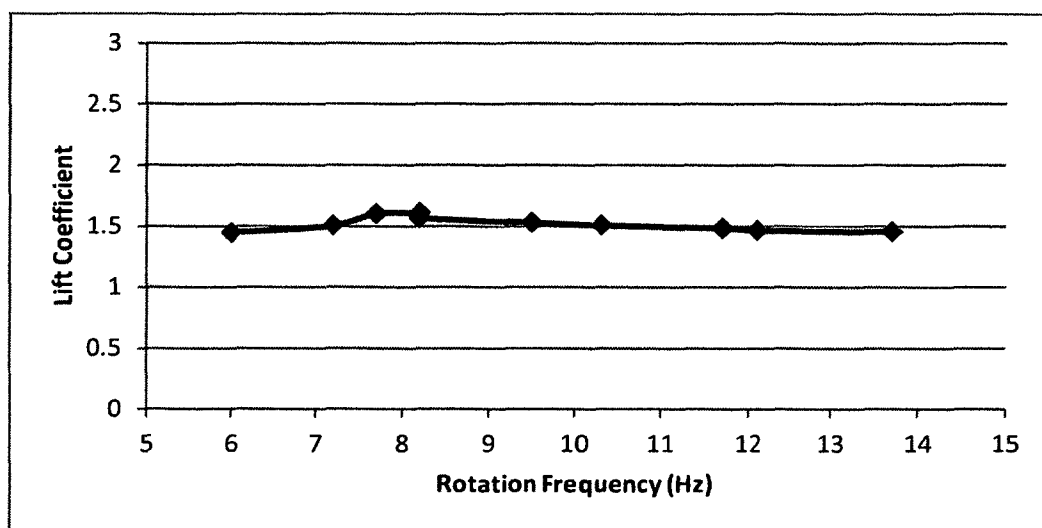


Figure 10-6. Lift coefficient over a range of spin frequencies at constant angle of attack

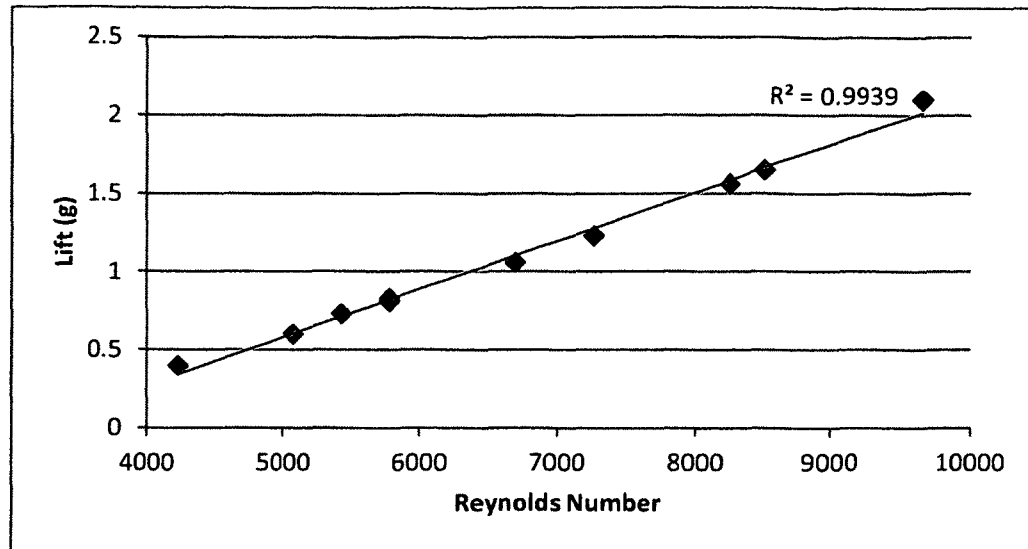


Figure 10-7. Lift generated over a range of Reynolds numbers

The results showed that there was very little variation in lift coefficient over the range of frequencies, which implies that the results are not significantly affected by small variations in frequency, and thus Reynolds number. However, the test showed that the overall lift force increases linearly with Reynolds number. Nevertheless, it is important that the error in the frequency measurement be as small as possible, since the calculated lift coefficient is proportional to the square of frequency.

10.1.5 Error analysis

During spin testing, there are various potential sources of error. In each test, three measurements are recorded, and each has its own precision and sources of error. These error sources are described in the following subsections. In order to reduce error in the results, at least two data points were taken for each test case (i.e. at each angle of attack) and the average value was used when presenting the data.

10.1.5.1 Angle of attack

The angle of attack of the wing is set by rotating the wing about its attachment to the spinner adapter and securing it in place with a grub screw inside the adaptor. The angle is measured with a protractor, using a vertical line on the adapter and the trailing edge of the wing as references. This method for setting the wing angle of attack may introduce errors in angle of attack of approximately $\pm 1^\circ$ due to the potential misalignment of the protractor with the wing and/or the vertical axis of the spinner. For curved or twisted wings, such as the locust wings or cambered wings, it is more difficult to accurately set the angle of attack of the wing, and may result in potential error of $\pm 2^\circ$.

Any error in the angle of attack could result in slightly increased or decreased lift. Based on the tests performed, the coefficient of lift, C_V , can increase by approximately 0.04 per degree of change in angle of attack. Therefore, an angular error of $\pm 2^\circ$ can result in a C_V error of up to ± 0.08 .

10.1.5.2 Rotational speed

During testing, it is often difficult to achieve a steady rotational frequency due to heating of the motor and variations in applied torque due to wing drag. It was observed that frequency measurements tend to constantly fluctuate by approximately ± 0.1 Hz. The recorded measurement was taken as the average value over approximately 5 seconds, with the lift and frequency being measured concurrently for each data point.

A fluctuation of ± 0.1 Hz results in a potential calculation error in C_V of approximately $\pm 5\%$ at 8 Hz, since the calculated lift coefficient is proportional to the square of the

rotational speed. However, as shown in Figure 10-6, small variations in rotational speed do not significantly affect the coefficient of vertical lift.

10.1.5.3 Lift measurement

During testing, the lift force measured by the digital balance varied by as much as 0.01g during a given test, even after the wake was developed and the wing rotation achieved steady state. Similar to rotational speed measurements, the average value over approximately 5 seconds was taken as the recorded value. While the precision of the digital balance was as high as 0.1mg, measurements were taken to a precision of only 0.01 grams, since values with higher precision showed a great deal of fluctuation.

10.1.5.4 Other sources of error

Other potential sources of error in the experimental set-up include the vibration of the spinner, which can affect the digital balance and cause error in the lift measurement. Furthermore, the high sensitivity of the digital balance can make it susceptible to minute air currents (including breathing), as well as vibration or loads placed on the work surface, such as leaning on the table or writing notes during a test. The effect of air currents was reduced by blocking as much air flow around digital balance as possible.

10.1.5.5 Repeatability

In order to evaluate the repeatability and reliability of the experimental set-up, a single 3-D printed wing was tested four times at various angles of attack, with the wing removed and re-installed onto the test apparatus for each data point. The results in Figure 10-8 show the data points for each tests, as well as the average lift coefficient at each angle of attack and error bars corresponding to one standard deviation, σ . The largest standard

deviation of 0.053 occurred at an angle of attack of 70°, which equals only 5% of the average value for that data set, while all data points fell within two standard deviations. Therefore, the experimental test set-up can be considered reliable since the overall random error was small.

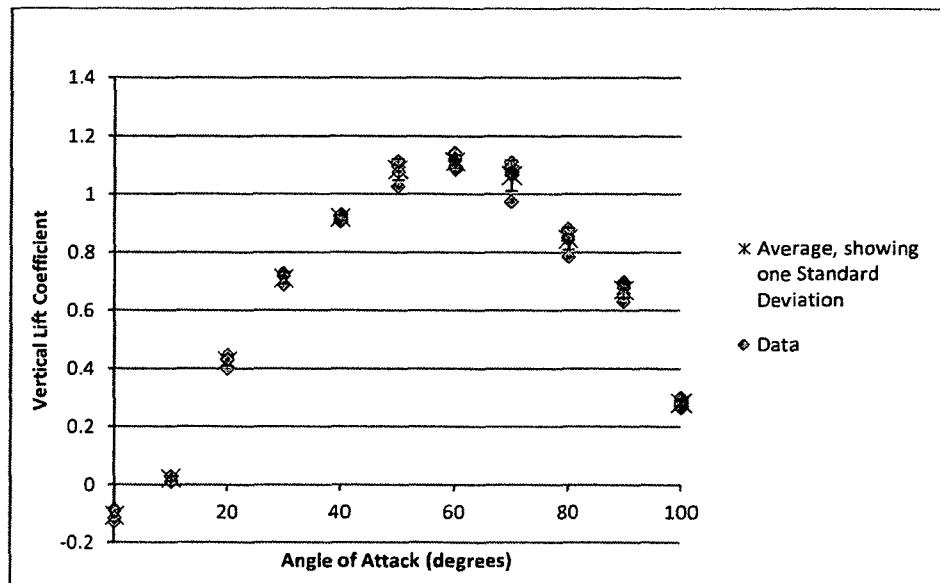


Figure 10-8. Repeatability of experimental set-up

10.1.6 Locust wings

In order to provide a basis for evaluating the performance the 3-D printed prototype wings, spin tests were performed on the hind wings of the African migratory locust (*locusta migratoria*). The morphology of the locust hind wing and the reasoning behind selecting it as a model is given in Chapter 4. The locust wings were acquired from desert locusts in a colony of live insects located at the Carleton University Biology Department. Wings were taken from two mature female locusts of approximately identical size. Two locusts are required because either two right wings or two left wings are required for spin testing. The wings were carefully cut from the locust at the root of the wing without harming the insect – insect wings do not contain any muscle or nervous tissue. Although

the locust has both fore wings and hind wings, only the hind wings were tested. A qualitative comparison of the left and right wings for each insect showed that the left and right wing of the same insect are nearly identical in shape, vein pattern, and even damage pattern. However, the wings from locust A were slightly larger than the wings from locust B, as shown in Figure 10-9. The damage to the wing tips, as shown in Figure 10-10, was similar in area and shape on all four wings, and may cause aerodynamic effects that are not representative of “typical” locusts.

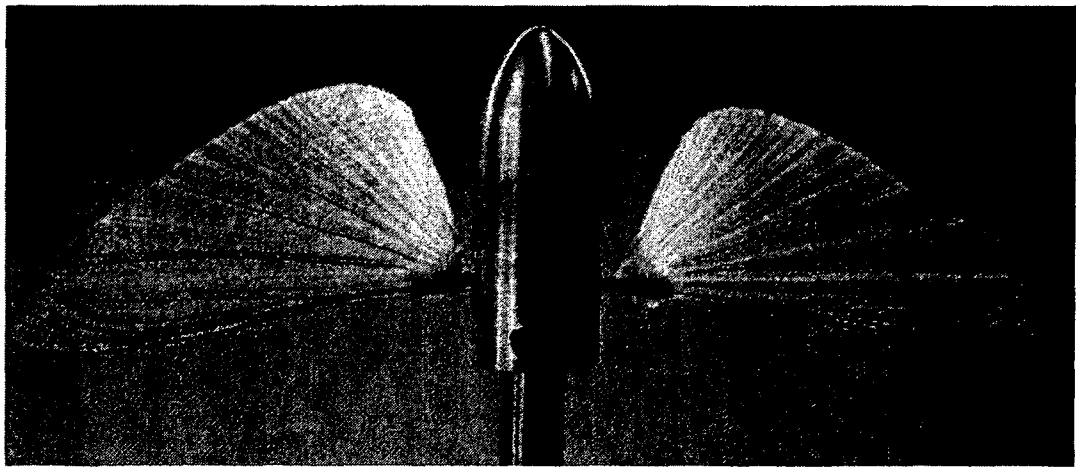


Figure 10-9. Comparison of locust A (left) and locust B (right) wing size

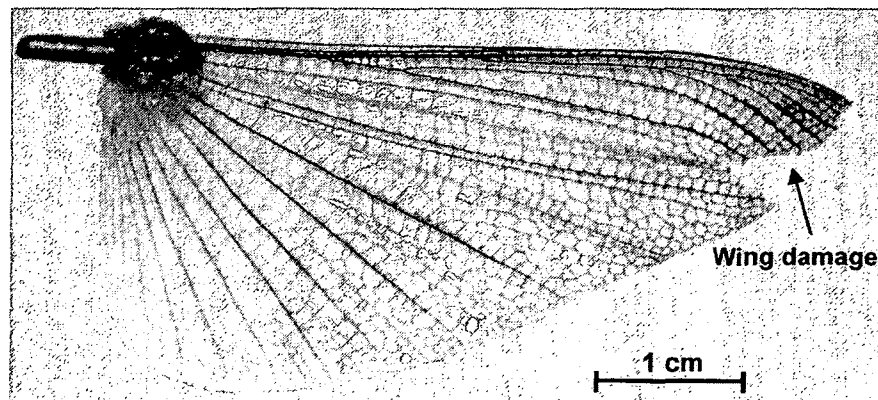


Figure 10-10. Wing tip damage to locust hind wing

Once the wings were removed from the locust, all testing was performed within 8 hours, since the wings dry out and become increasingly brittle over time. As the wings dry, the properties change and the results cannot be considered as representative of real flight. Tests were performed on each individual single wing, as well as in pairs made up of two left wings and two right wings respectively.

One of the challenges in testing the real locust wings was mounting them onto the spin apparatus. Locust wings have a natural tendency to fold up, as they would when the insect is not flying (Figure 10-11 and Figure 10-12). Therefore, the wings must be manually spread out and held in place while bonding the wing mount to the root of the wing. Once the epoxy adhesive is cured, the wing remains fully extended. However, this process can result in variance in the wing's camber between each wing if the wing is not fully extended. Furthermore, it was difficult to set the angle of attack due to the twist and camber of the wings, and because there is not an easily distinguishable chord line. For each test, the angle of attack was measured in reference to the chord line along the medial edge of the wing.

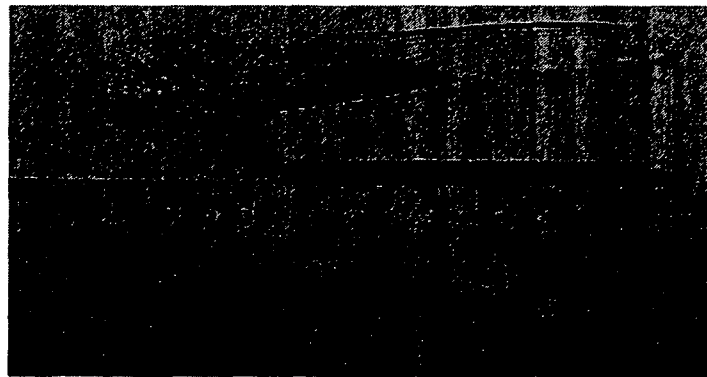


Figure 10-11. Folded locust hind wing



Figure 10-12. Close up of folded hind wing with trailing edge highlighted

The rotational frequency used during the test was 14 Hz, which was calculated based on the desired Reynolds number of 5600, an average wing chord of 19 mm (0.75 in) and an average wingspan of 50 mm (1.97 in). This frequency was maintained throughout the tests by manually adjusting the motor speed by varying the pulse-width modulated (PWM) signal via the motor controller.

Table 10-1. Locust wing dimensions

	Locust A	Locust B	Average
Span	54 mm	46 mm	50 mm
Average chord	20 mm	18 mm	19 mm
Area mm²	790 mm ²	646 mm ²	718 mm ²
Second moment of area - Single wing	70.5 cm ⁴	45.1 cm ⁴	57.8 cm ⁴
Second moment of area - Pair of wings	141 cm ⁴	90.2 cm ⁴	115.6 cm ⁴
Re @ 14 Hz	6333	4856	5571

The results of the spin tests for real locust wings are shown in Figure 10-13 and Figure 10-14. The peak lift coefficients ranged from 1.26 to 1.78, which are achieved at angles of attack between 40 and 60 degrees. The variation in lift values between each wing may be attributed to the variation in camber resulting from the attachment of the wing mount. Each wing showed a gradual loss of lift at high angles of attack, as compared to many conventional airfoils which generally stall at much lower angles, between 15 and 20

degrees. While the locust A wings produced higher lift than those of locust B, the locust B produced higher lift coefficients. The difference may be attributed to the amount of camber of in each wing, which may be different due to the bonding of the wing mount. A higher lift coefficient for the smaller Locust B wings implies that it is generating more lift for its size than the larger Locust A wings.

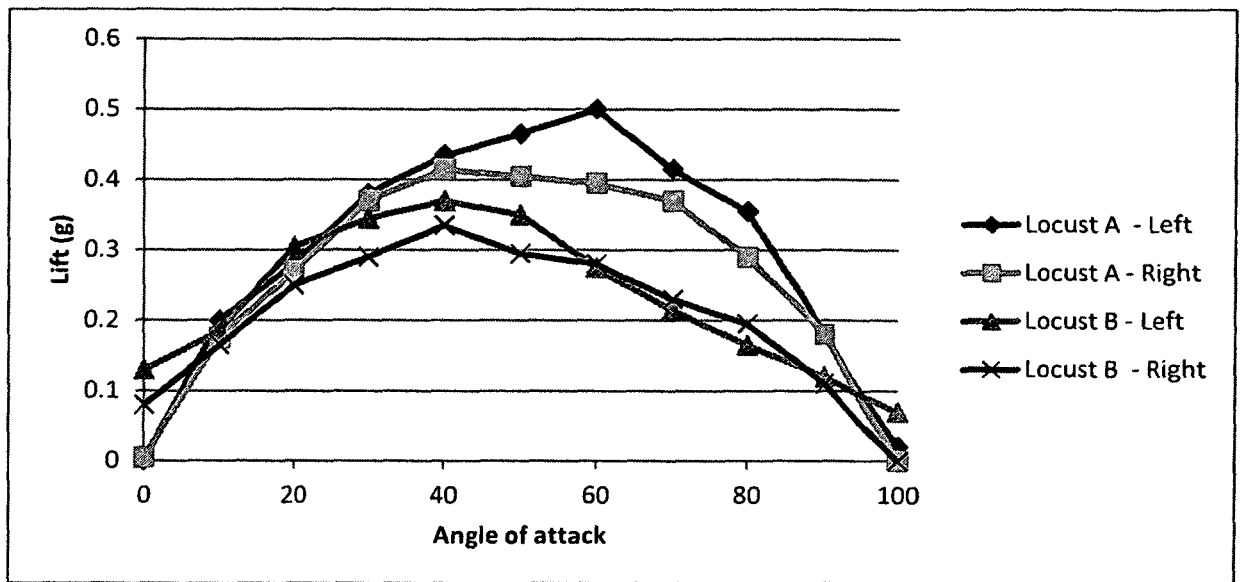


Figure 10-13. Lift generated by individual locust wings

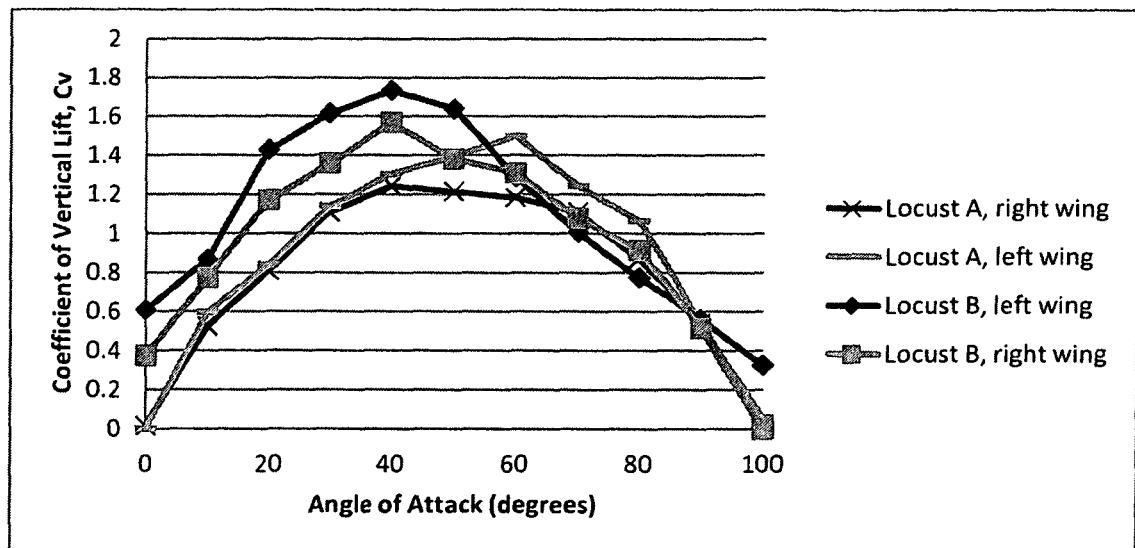


Figure 10-14. Coefficient of vertical lift results for individual locust wings

The results obtained from the locust wings follow the same trend and are similar in value to wings tested by Usherwood & Ellington (2002a), as shown in Figure 10-15.

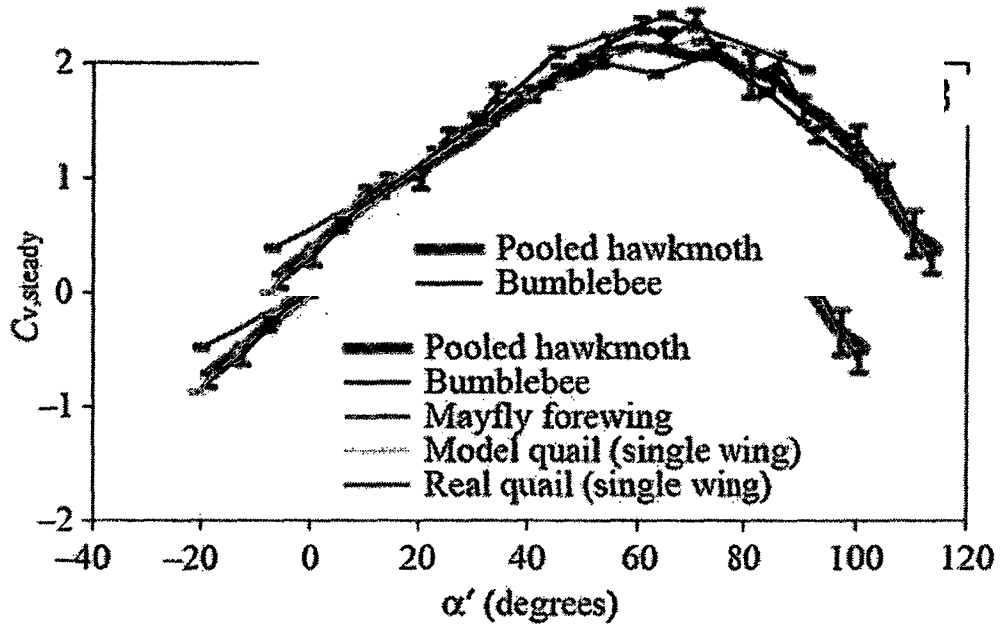


Figure 10-15. Vertical lift coefficients for various wings tested by Usherwood & Ellington (2002a)

The locust wings were then tested in pairs. The spin test requires either two right wings or two left wings to be tested together. As such, the right wings of locusts A and B were tested together, and the left wings of locusts A and B were tested together. Since the wings are of different size, the calculation of the lift coefficient took into account the second moment of area of each individual wing by summing the lift coefficient contribution from each wing.

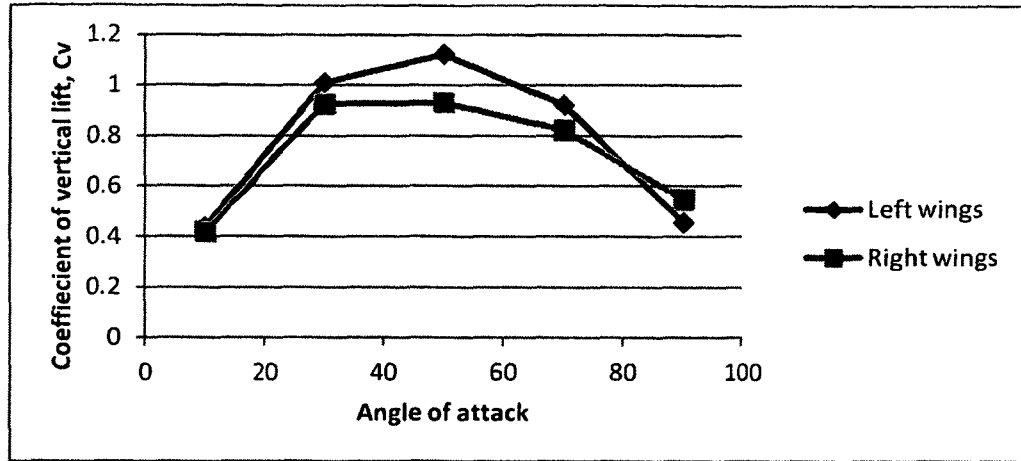


Figure 10-16. Coefficient of vertical lift for locust wing pairs

Results in Figure 10-16 show that the left and right wings together produce a lower overall lift coefficient than a single wing. This is due to a loss in efficiency likely resulting from the wake of the opposite wing. Similarly, if one considers the propeller in a fixed wing aircraft, an increased number of propeller blades generally reduces a propeller's propulsive efficiency. However, this may not apply to flapping flight, since the wake interactions would likely be different for flapping wings than for revolving wings. Furthermore, the wake will have less of an effect since the insect, or MAV, or steadily moving forward.

10.1.7 3D printed prototype wings

Since the 3-printed wings are larger than the real locust wings, the rotational frequency was set to 8 Hz in order to achieve approximately the same Reynolds number of 5600, as shown in section 10.1.1. During the testing, it was difficult to achieve exactly 8 Hz, however the motor tended to settle at 8.4 Hz consistently, which corresponded to a Reynolds number of 5922. Nevertheless, the calculation of C_V at each data point uses the frequency measured at the time of each lift measurement in order to account for any variation in frequency.

10.1.7.1 Effect of vein angle

The lift performance of single wings with different vein configurations is shown in Figure 10-20, while peak vertical lift coefficient values ($C_{v, \max}$) are given in Table 10-2. The configurations tested included wings with no veins, single veins at 10° , 20° , and 30° to the leading edge respectively, and multiple veins at both 10° and 40° (see Chapter 9 for details).

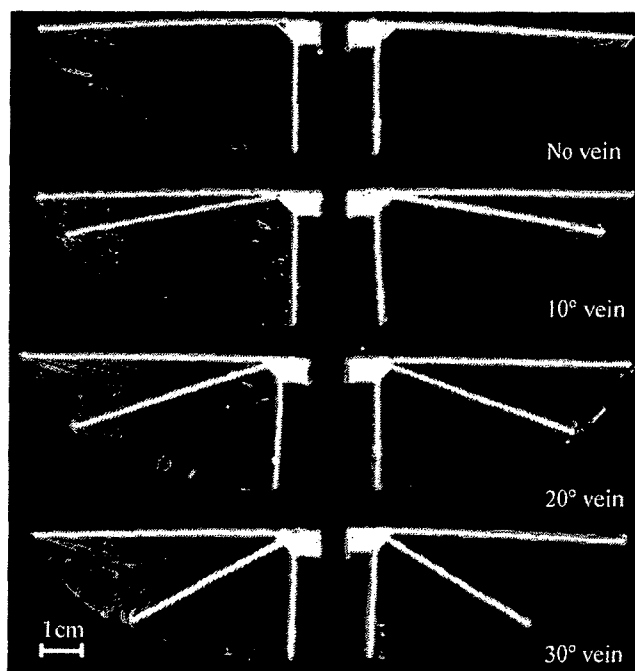


Figure 10-17. Examples of 3-D printed wing prototypes tested, showing various vein angles

Results given in Table 10-2, Figure 10-18, and Figure 10-19, showed that peak lift values are achieved with veins at 20° and 30° , with comparable results, while wings with no veins produced the least amount of lift. Wings with no veins or a single vein at 10° produced positive lift at angles of attack as high as 100° . This is most likely due to these wings being sufficiently flexible to twist into a positive angle of attack under aerodynamic loads, resulting in positive lift generation. In most cases, maximum lift is generated between 40° and 50° angle of attack. The peak lift coefficients also exceeded

that of the real locust wings at high angles of attack; however, the real locust wings produced a higher vertical lift coefficient at angles of attack below 30°. The locust wings likely outperform the artificial wings due to their cambered airfoil shape, while the artificial wings are relatively flat.

Table 10-2. Peak vertical lift coefficient values and stall angles for artificial wings with various vein configurations

Vein angle	$C_{v, \max}$	AoA at $C_{v, \max}$
0°	1.15	40°
10°	1.54	50°
20°	1.77	50°
30°	1.75	50°
10° and 40°	1.66	50°

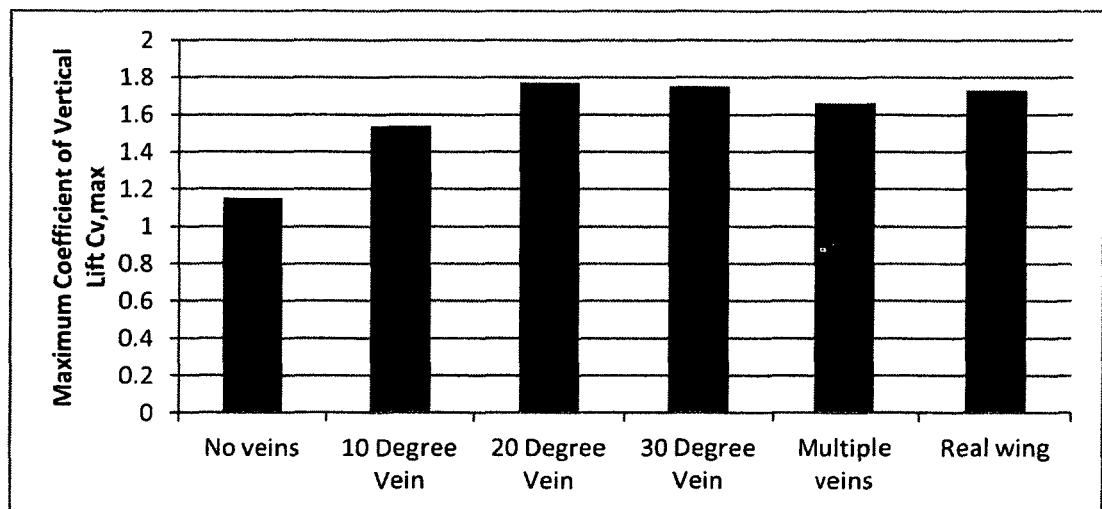


Figure 10-18. Comparison of peak vertical lift coefficient for each wing design

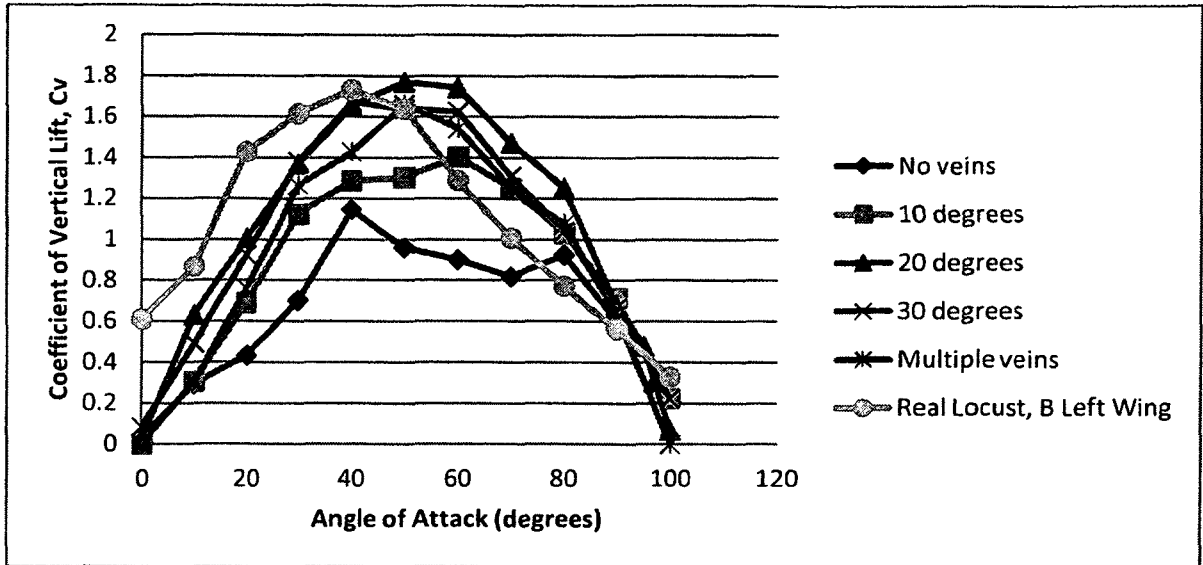


Figure 10-19. Comparison of single artificial wings versus real locust wings

Lift performance of wing pairs in each vein configuration are shown in Figure 10-19. Similar to the insect wings, when spun in pairs, the wings produce a lower overall lift coefficient. Wings with veins at 20° and 30° both achieved the highest lift coefficients, while the wings with no veins were able to sustain higher lift at high angles of attack.

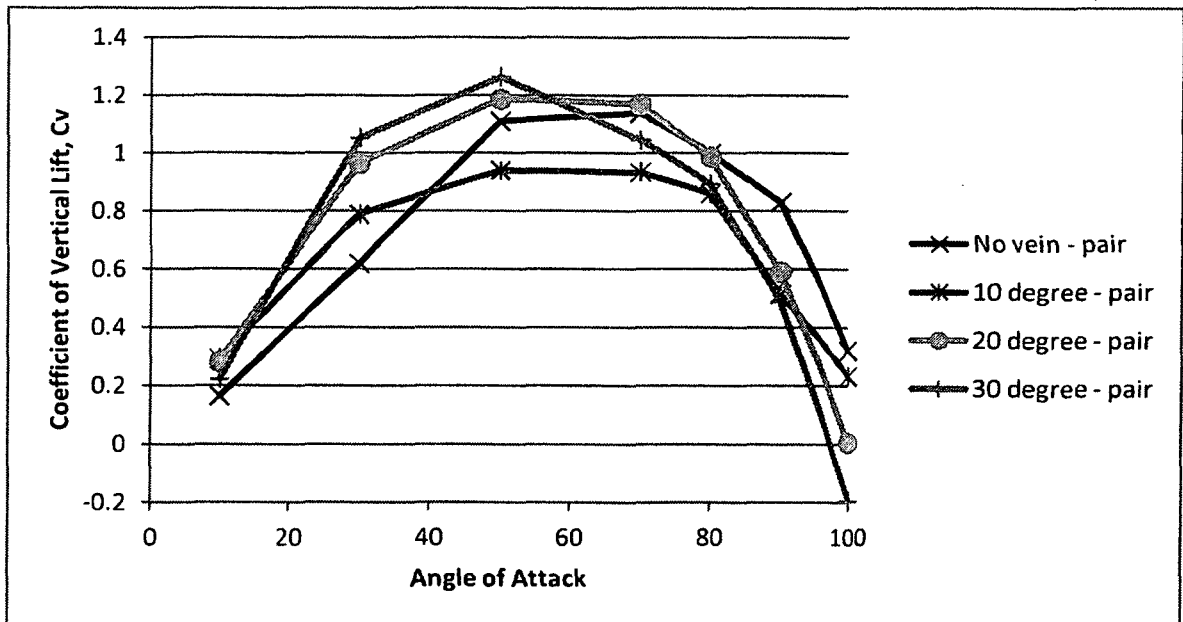


Figure 10-20. Lift coefficient versus angle of attack for wing pairs with various vein configurations

10.1.7.2 Repeatability of the fabrication process

In order to test the repeatability of both the test method and the manufacturing process, multiple wings in each configuration were tested. Figure 10-21 and Figure 10-22 show the results of tests on wings with single veins at 10° and 30° respectively. In each case, all wings of a given planform were fabricated in the same batch. The tests showed that the wings of the same configuration perform comparably, with all data points falling nearly within one standard deviation. The average standard deviation among the different wings ($\sigma_{\text{avg}} = 0.081$) was larger than that of the experimental test set-up ($\sigma_{\text{avg}} = 0.024$), suggesting that the variance in performance between each wing is due to the fabrication process, and not due to error in the testing method. Despite the reasonable correlation in lift performance between each wing, repeatability of the fabrication process will need to be improved as the wing design becomes more optimized.

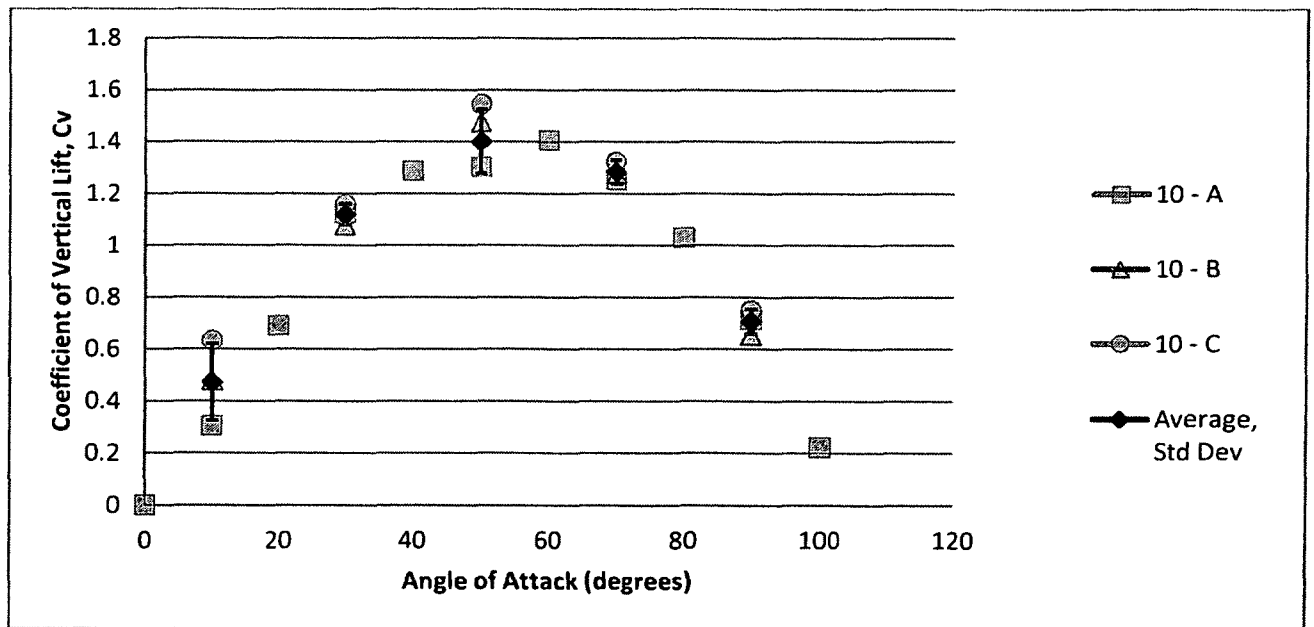


Figure 10-21. Results for wings with veins at 10°

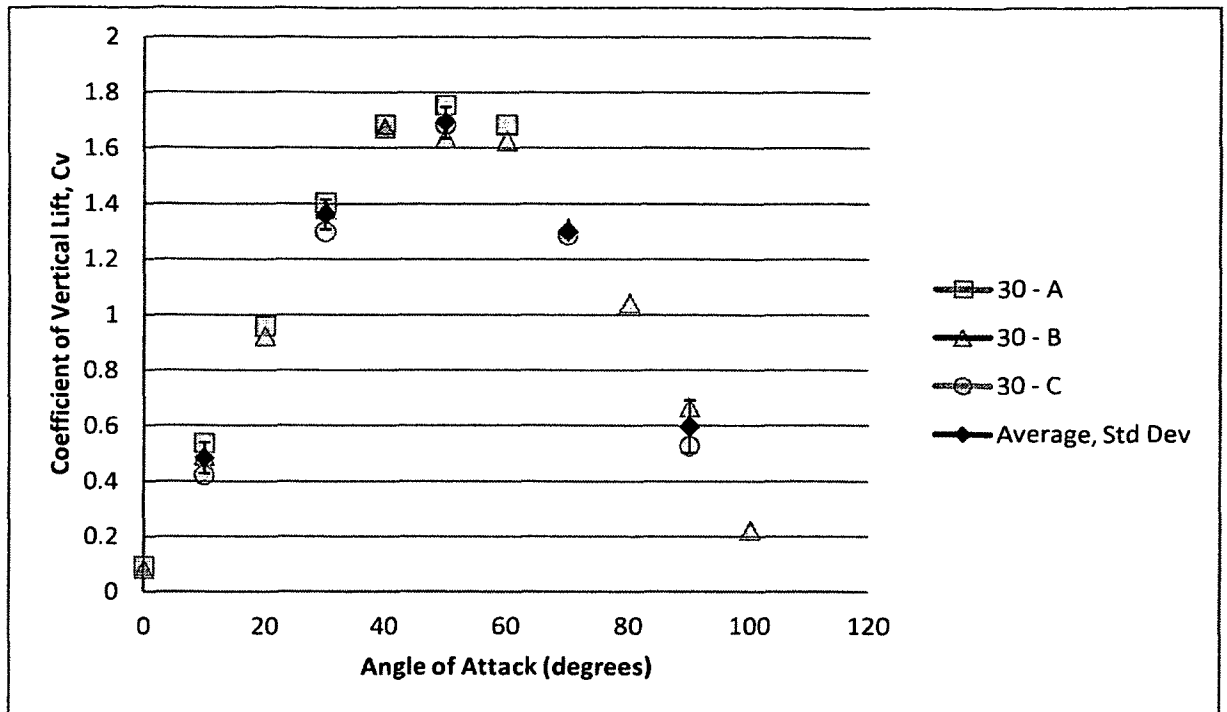


Figure 10-22. Results for wings with veins at 30°

10.1.7.3 Single versus pair of wings

In the testing of the locust wings, it was observed that a single wing produced a higher overall coefficient of vertical lift than a pair of wings at the same angle of attack, when taking into consideration the added wing area. While a loss in efficiency is to be expected with two revolving wings versus a single revolving wing due to the interaction of the wake from the preceding wing. Tests were performed for each wing configuration in order to quantify this difference and to determine if the wing design has any effect on the wing efficiency in wake interactions. Results are shown in Figure 10-23 through Figure 10-26.

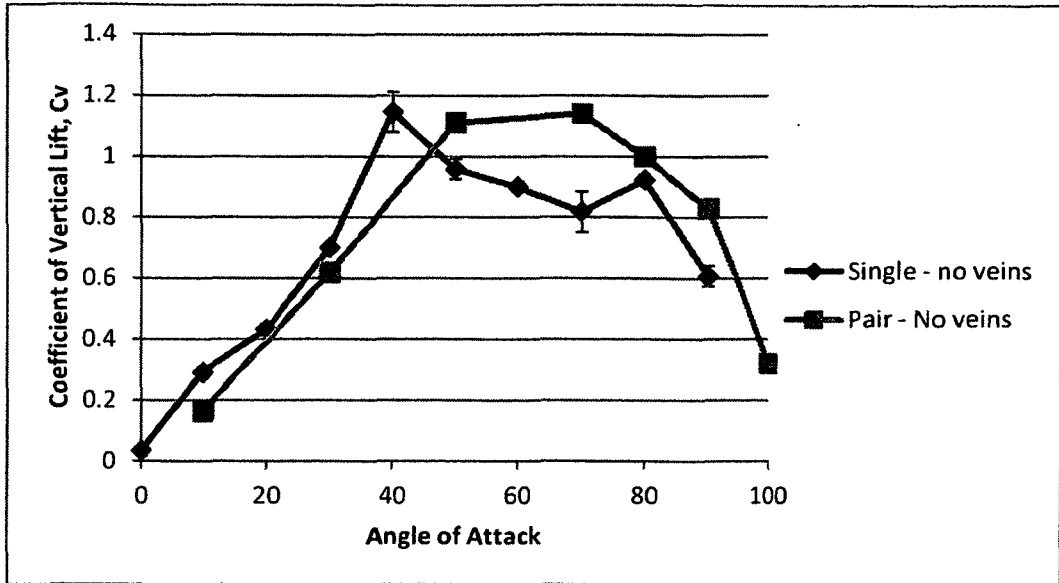


Figure 10-23. Comparison of single vs pair of wings - no veins

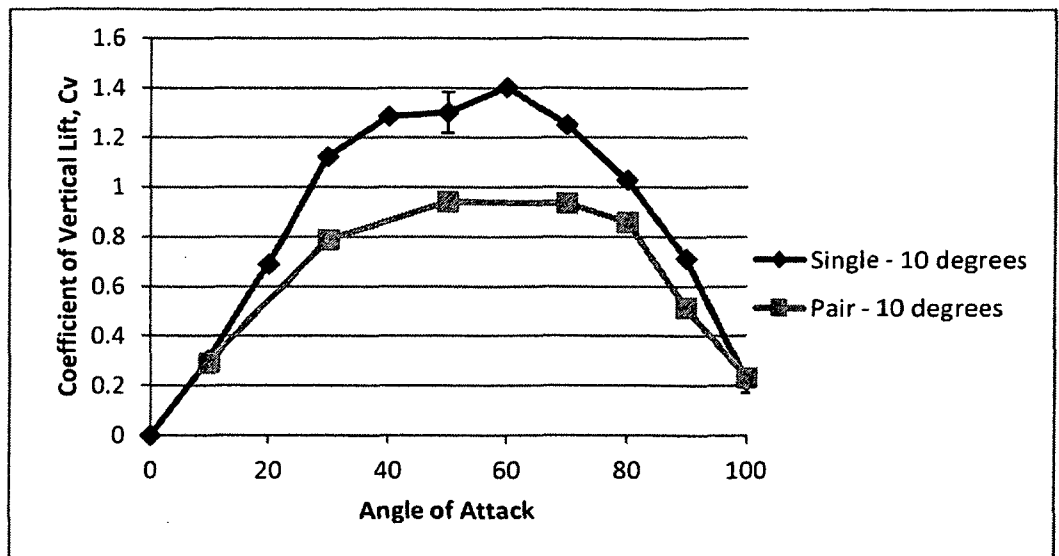


Figure 10-24. Comparison of single vs pair of wings -10 degree vein

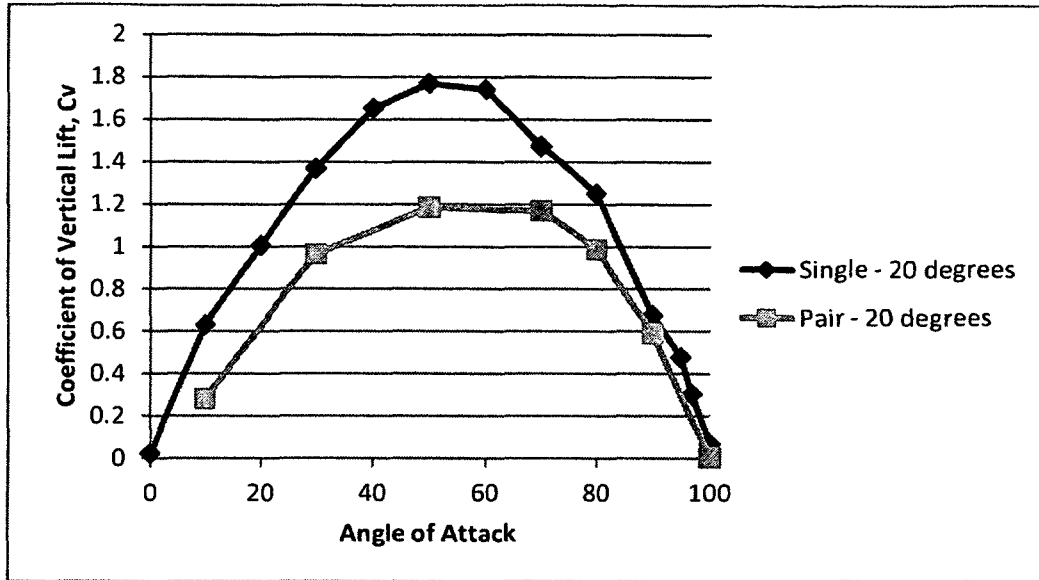


Figure 10-25. Comparison of single vs pair of wings - 20 degree vein

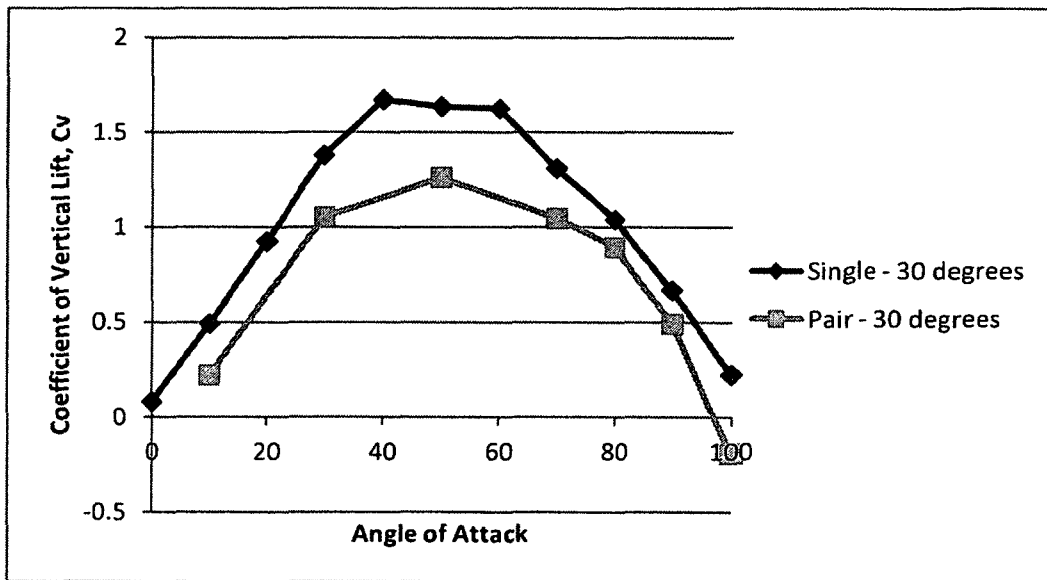


Figure 10-26. Comparison of single vs pair of wings - 30 degree vein

The percent difference in vertical lift coefficient between single and pairs of wings for each wing configuration is shown in Figure 10-27. Most of the wing designs showed a 20-40% difference in lift between a single wing and a pair of wings at angles of attack between 30° and 70° angle of attack. However, wings with no veins showed the greatest difference between spinning a single wing and a pair of wings, where the pair of wings

actually produced a higher overall lift coefficient. This may be due to the highly flexible membrane which produces less severe wing wake, while the flexibility of the following wing may make it less susceptible to loss of lift due to turbulent flow, as demonstrated by flexible wing MAVs described in Chapter 2. This data is based on only one data set, and further testing is recommended to determine the effect on wing flexibility on aerodynamic efficiency in turbulent flow.

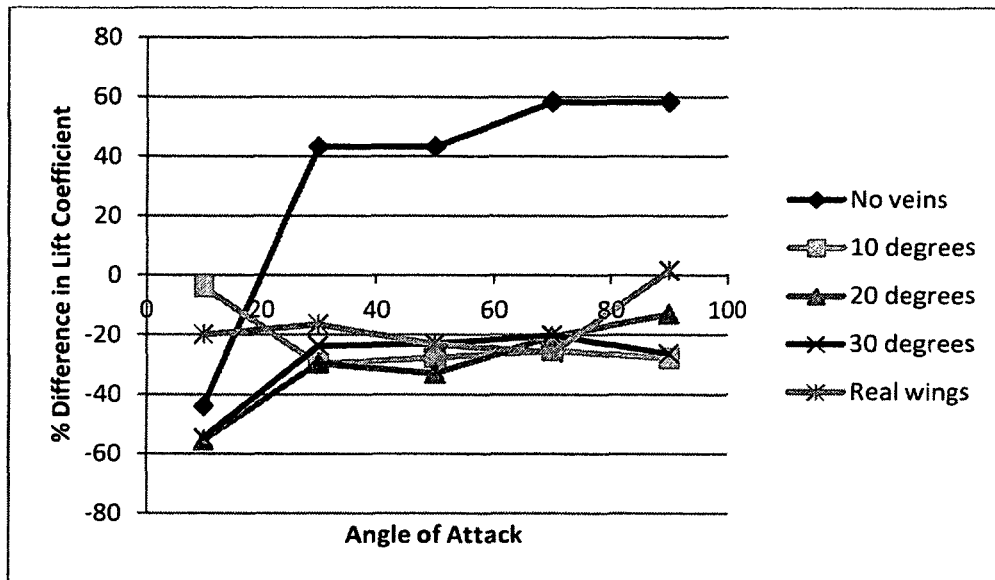


Figure 10-27. Percent difference in lift between single and pair of wings

10.1.7.4 Effect of camber

During initial printing trials of the prototype wings, warping of the wings occurred due to the asymmetric cooling of the wing. While this warping was remedied by heating the build platform and evenly cooling the wings between two flat surfaces, it was hypothesized that this curvature and camber of the wing during fabrication may provide an aerodynamic benefit, in the same way that camber increases lifting performance in traditional rigid airfoils.

In order to further increase the camber and flexibility of the wings, the radial wing veins in the centre of the wing were cut at the root (Figure 10-28), allowing the vein to hinge at the wing root and promote the “umbrella effect” of the wing. This affect was also evaluated through a series of tests, with results shown in Figure 10-29 through Figure 10-31. Each test was performed with a single wing.

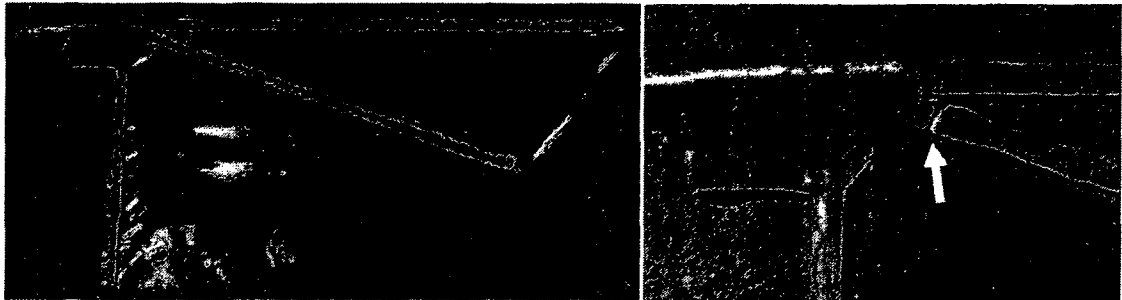


Figure 10-28. Vein clipped at wing root for increased flexibility

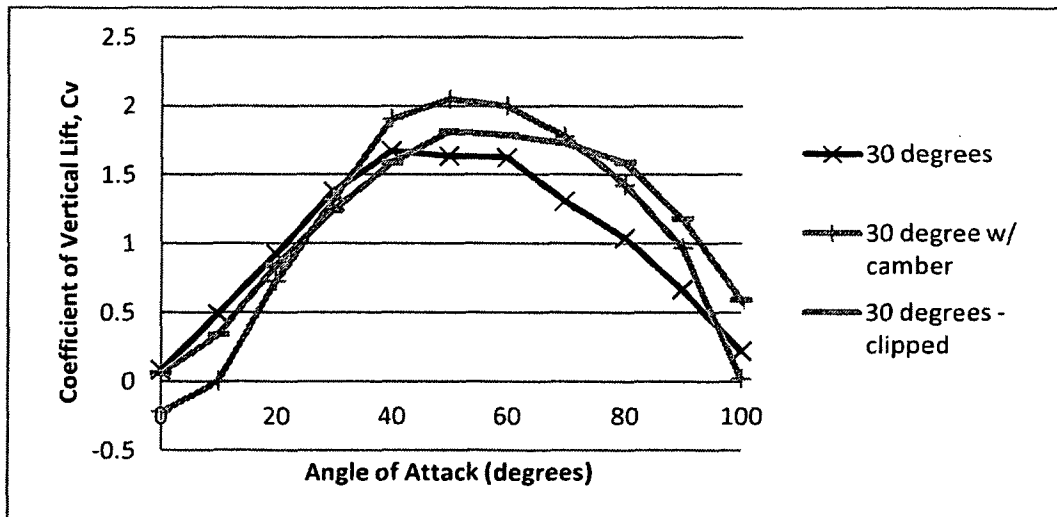


Figure 10-29. Effect of wing camber on wings with 30° vein angle

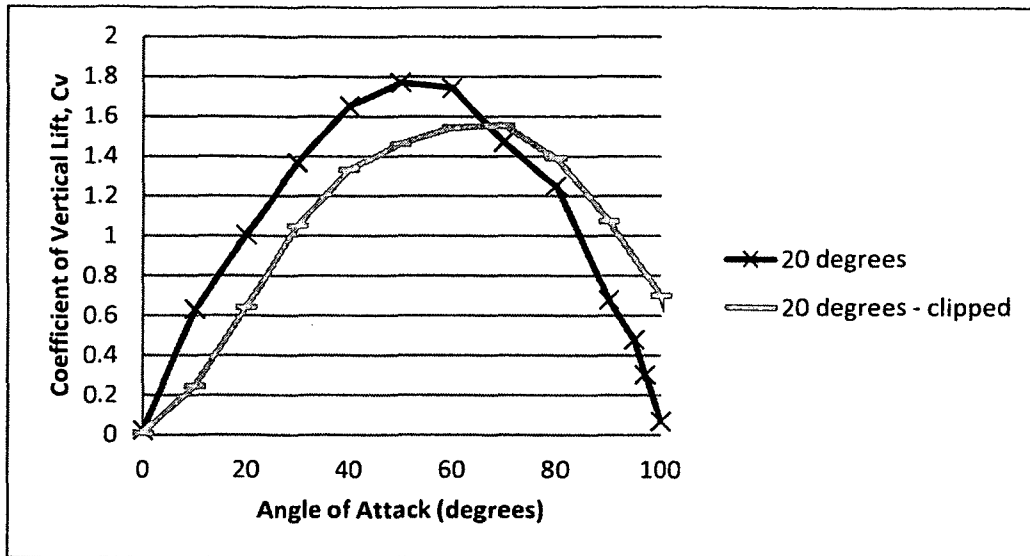


Figure 10-30. Effect of wing camber on wings with 20° vein angle

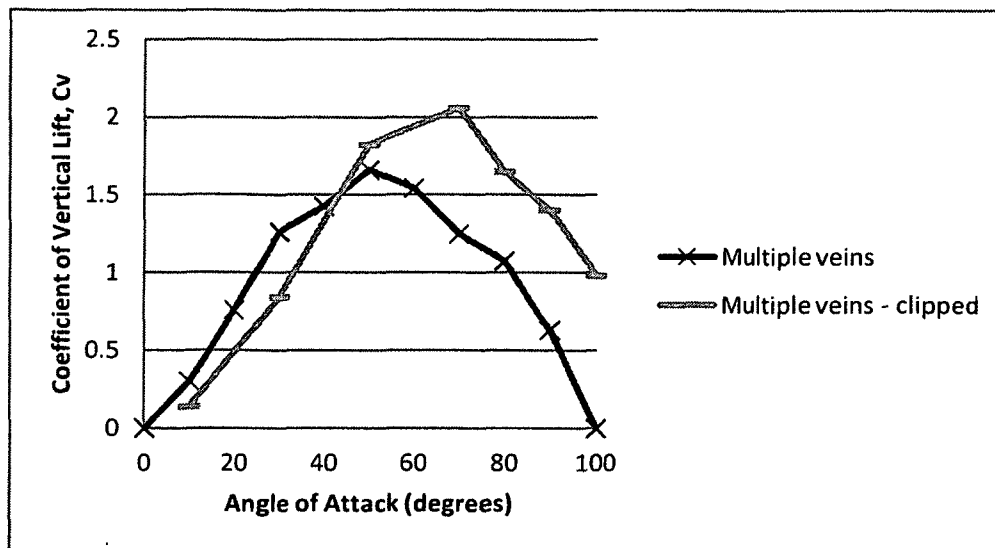


Figure 10-31. Effect of wing camber on wings with multiple veins

Results show that the cambered wings show an overall increase in lift coefficient at higher angles of attack, but lower lift coefficients at angles of attack below approximately 40°. Both a cambered wing with a single vein at 30° and the wing with multiple clipped veins achieved C_v values greater than 2.0. In the latter case, lift coefficient values greater than 1.0 were achieved even at angles of attack up to 100°. The clipped vein allows the vein to hinge at the wing root and increase the wing camber, as shown in Figure 10-32.

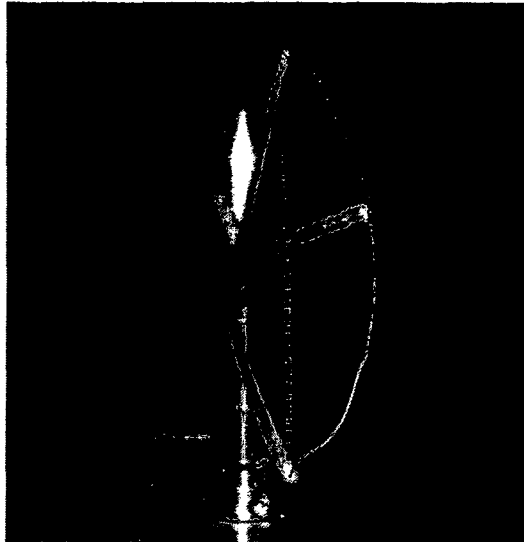


Figure 10-32. Wing with clipped wing vein, with trailing edge highlighted to show camber

10.1.7.5 Effect of surface roughness

As shown in chapter 4, surface roughness plays an important role in unsteady aerodynamics and flapping wing flight. The 3-D printing fabrication process introduces surface roughness where veins are applied. The effect of the roughness provided by the veins on the lifting performance is of interest since the fabrication process itself may provide inherent aerodynamic advantages by creating this roughness on the top side of the wing in order to delay stall and increase lift at high angles of attack, while maintaining a smooth bottom (high pressure) surface to reduce drag. This may present an advantage over corrugated airfoils, which are rough on both the top and bottom surfaces.

For wings with no radial veins in the centre of the wing, surface roughness was added by applying small amounts of cyanoacrylate (CA) adhesive to the membrane, which dries to a thin, brittle coating in a few seconds. The CA was applied in radial lines to more accurately mimic the corrugation pattern of a real wing (see Figure 10-12). The application of the adhesive caused some distortion of the membrane due to chemical reaction between the CA and the PVDC, while the deposited CA added additional

roughness. The roughened wing is shown in Figure 10-33, while the corrugation in a locust hind wing is shown for comparison in Figure 10-34.

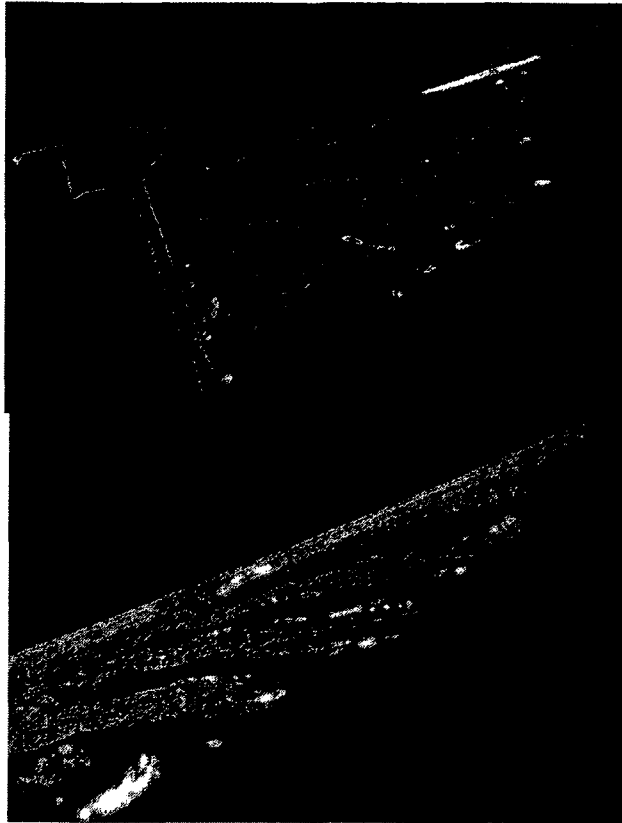


Figure 10-33. Rough texture applied to wing membrane using cyanoacrylate



Figure 10-34. Corrugation in the locust hind wing (Schnackenburg, 2007)

The results of tests conducted on wings single veins at 30° and multiple veins at 10° and 40° are shown in Figure 10-35 through Figure 10-37. These tests showed that having the veins on the upper surface of the wing results in increased lift at higher angles of attack and delayed stall, however unlike with adding camber or additional flexibility, lift values at lower angles of attack are maintained. Furthermore, the roughness added to the wing with no veins also increased lift at high angles of attack.

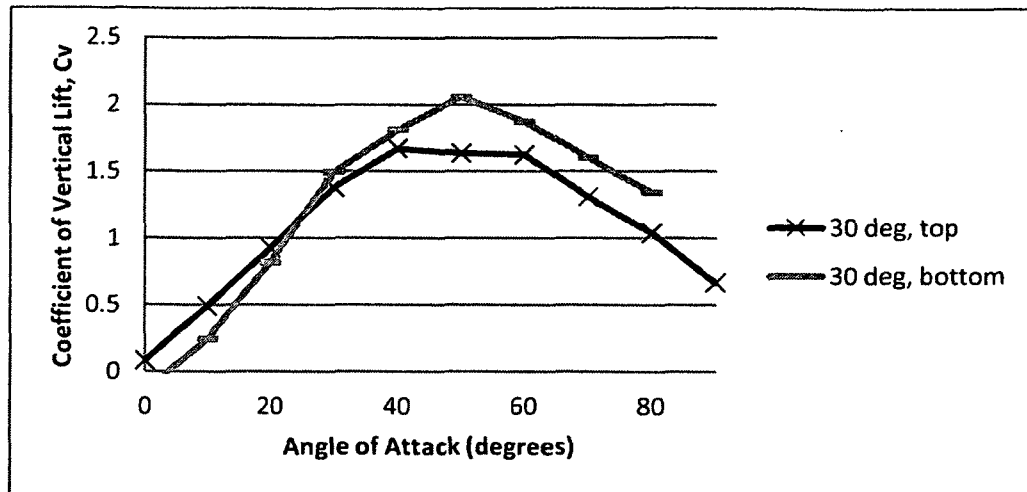


Figure 10-35. Effect of vein orientation and roughness - 30 degree vein

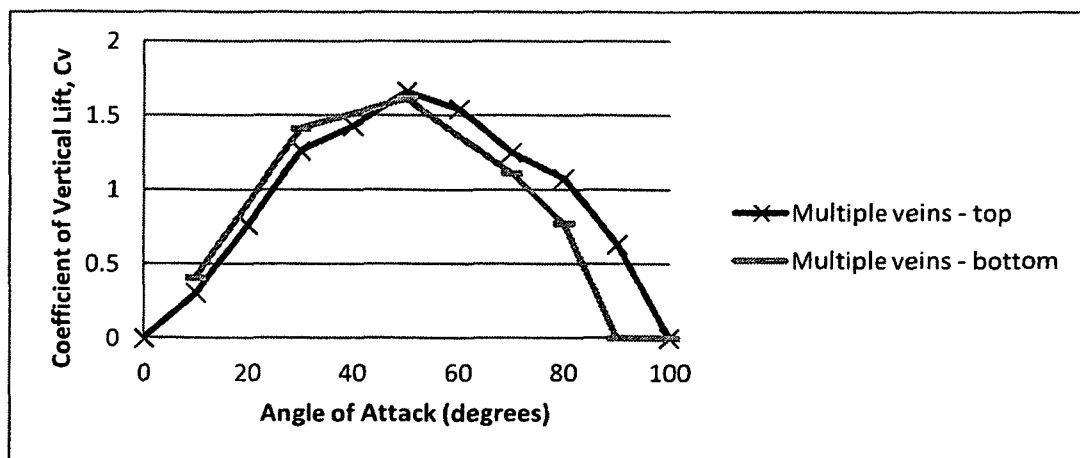


Figure 10-36. Effect of vein orientation and roughness - multiple veins

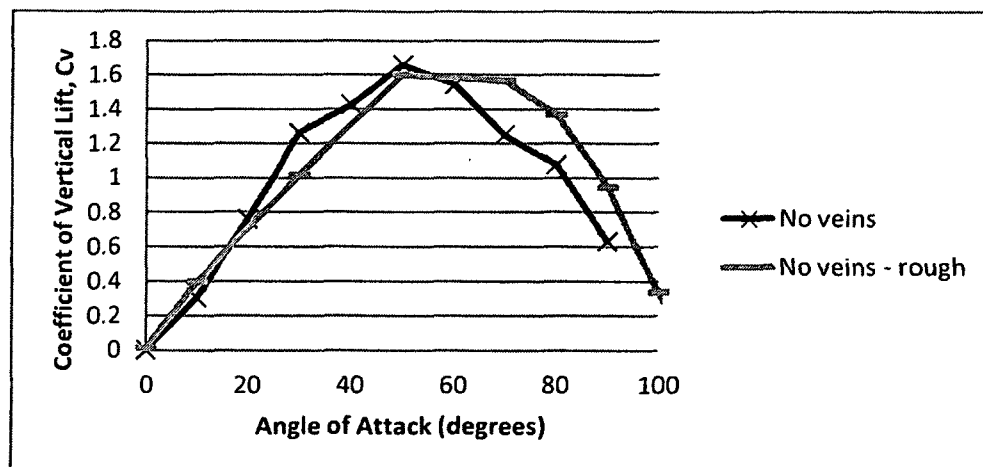


Figure 10-37. Effect of roughness on wing with no veins

The effect of surface roughness was evaluated further by analyzing the change in lift coefficient at various Reynolds numbers. As shown in Figure 10-38, smooth wings showed little change in lift across a range of angles of attack and Reynolds numbers. Rough wings also showed little change in lift at angles of attack of 20° and 45° across various Reynolds numbers; however at an angle of attack of 80°, the rough wing showed a significant increase in lift coefficient of 0.36 between Reynolds numbers of 4,440 to 10,715, equating to an increase in lift of 30%.

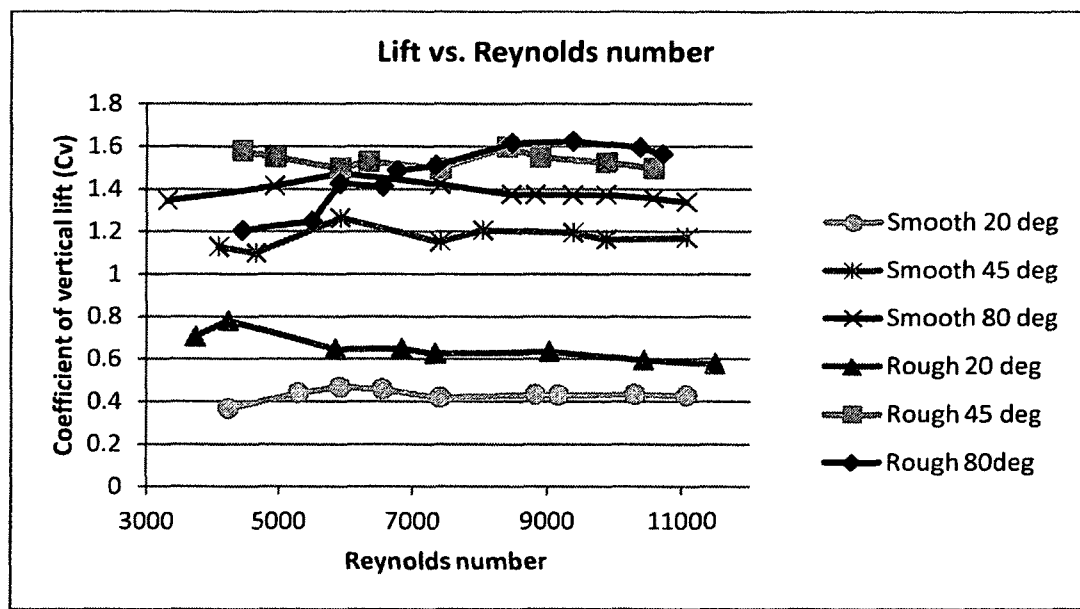


Figure 10-38. Effect of surface roughness on lift performance at various Reynolds numbers. (Angles represent angle of attack)

10.1.8 Scaled wings

The calculation of coefficient of vertical lift, C_v , allows for the comparison of the 3-D printed “artificial” wing prototypes with real locust wings, there is potential for error due to the difference in scale between the real and fabricated wings. Therefore, a set of locust-scale wing prototypes was fabricated in order for a direct comparison to be made. These wing prototypes were scaled to match the average wing length and chord of the

locust wings tested in this chapter, while following the same planform shape and vein configurations as the wing prototypes tested in the previous sections.

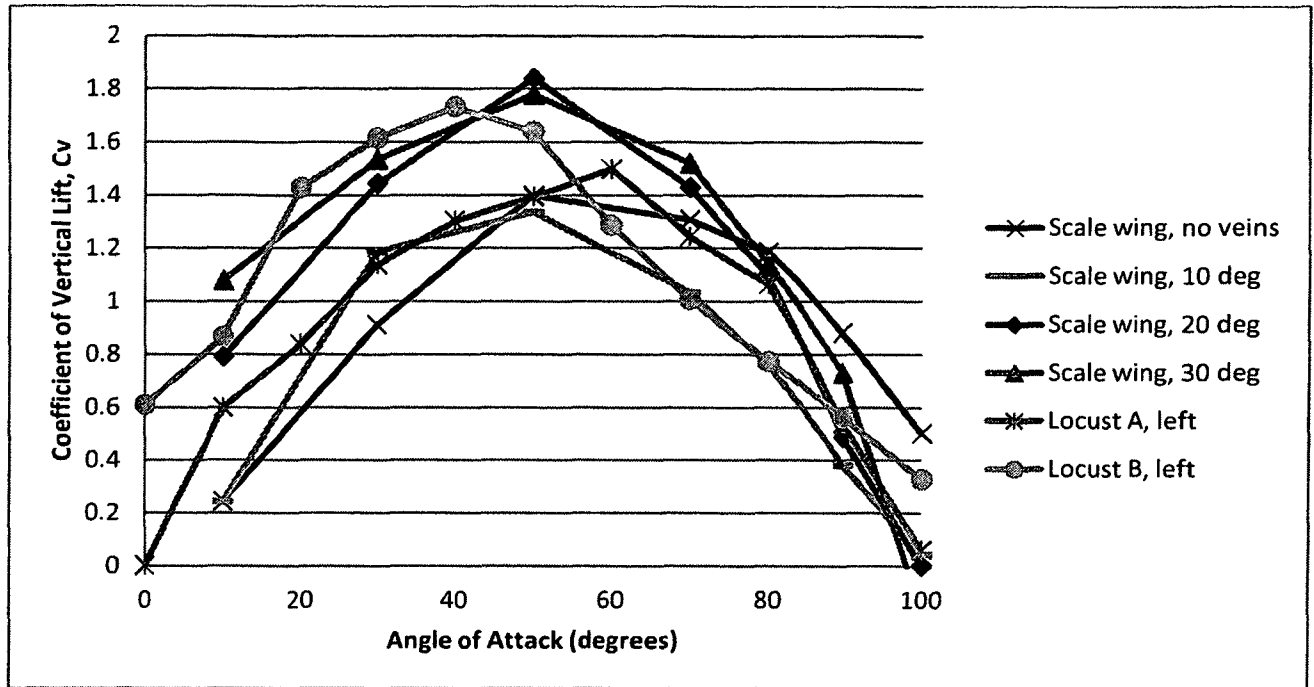


Figure 10-39. Lift coefficient values for insect-scale printed wings and real locust wings

As shown in Figure 10-39, the 3-D printed wings exceed lift values for the locust wings at angles of attack greater than 40°. As seen in other tests, wings with single veins at 20° and 30° respectively provided the highest lift coefficient values, which are in fact close to the same values as for the larger scale wings.

10.2 Stiffness distribution

Flexural stiffness tests were performed in order to compare the stiffness of the 3-D printed prototype wings with trends found in nature, as well as to quantitatively compare the spanwise and chordwise stiffness distributions of the different wing designs. Wing stiffness was measured by installing the wing onto the spin rig such that it was flat (0° angle of attack) and tightened such that it could not rotate. The spin rig was mounted on

the knife edge fulcrum, which in turn pressed on the digital balance in the same manner as in the spin testing. Digital calipers were mounted to a stationary stand and were used to apply a bending force to the wing. The calipers were zeroed at the point where they were touching the wing, but not exerting and force on the wing (as measured by the digital balance). The caliper was subsequently moved a prescribed distance, applying force to the ventral (bottom) surface of the wing, and bending the wing upward. The reaction force was obtained from the digital balance.

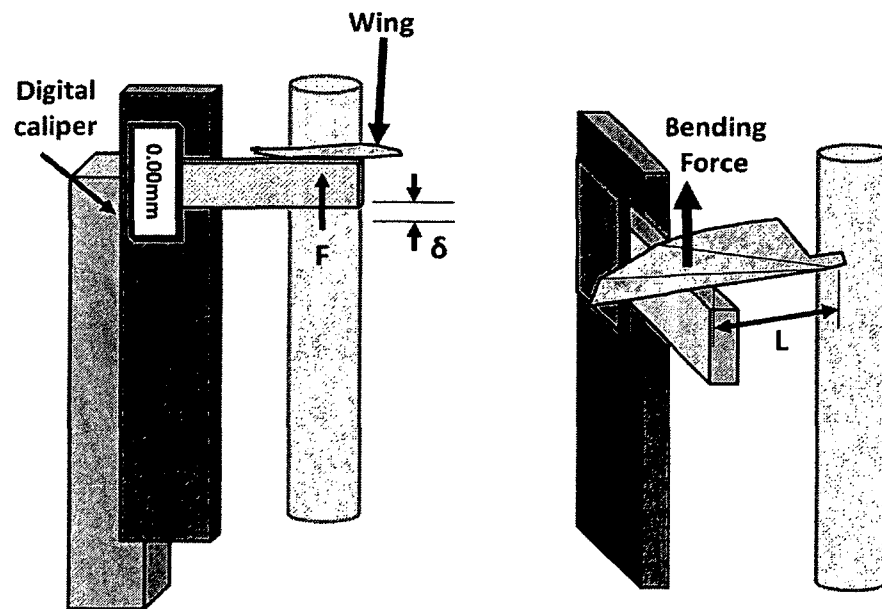


Figure 10-40. Schematic of bending test setup

Flexural bending stiffness, EI , was calculated by

$$EI = \frac{FL^3}{3\delta} \quad (10.6)$$

where F is the applied bending force, L is the beam length, and δ is the displacement. The bending stiffness EI is a function of both the wing's material properties (modulus of elasticity, E) as well as geometric properties (second moment of area, I). For each wing

design, the bending load was applied at 75% of the span and at 75% of the chord. Displacements ranged from 1 mm (0.04 in) to 6 mm (0.24 in), with the reaction force measured at each displacement value. However, the bending stiffness relationship given by equation 10.6 is only valid for small displacements (Combes & Daniel, 2003), therefore deflections that exceed $\delta > 0.05*L$ were disregarded. The average bending stiffness for each wing is listed in Table 10-3.

Table 10-3. Spanwise and chordwise stiffness measurements

	Spanwise EI ($N\ m^2$) $\times 10^4$	Chordwise EI ($N\ m^2$) $\times 10^4$
No veins	1.663	1.289
10 degrees	1.737	1.017
20 degrees	2.370	0.497
30 degrees	2.017	0.846
Multiple veins	1.477	0.608
Multiple veins - clipped	0.967	1.636

As discussed in Chapter 4, a study by Combes and Daniel (2003) showed that a relationship exists between wing span and stiffness, as well as wing chord and stiffness, that holds across many different wing species. This relationship is shown in Figure 10-41. The results from spanwise and chordwise bending stiffness measurements in the present study are shown in Figure 10-42 and Figure 10-43 respectively for each wing type, with the trend lines for spanwise and chordwise stiffness relationships superimposed. The results show that the spanwise stiffness of the 3-D printed wings is only slightly lower than what is predicted by the trend shown in Figure 10-41. However, the chordwise stiffness of the 3-D printed wings is much higher than what is predicted.

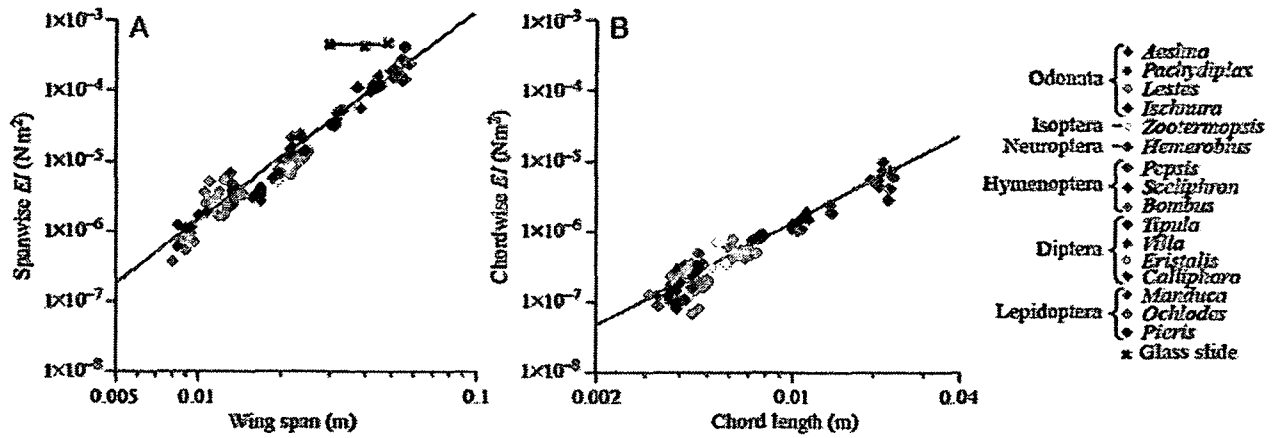


Figure 10-41. Relationship between spanwise and chordwise stiffness with wing span and chord length (Combes & Daniel, 2003)

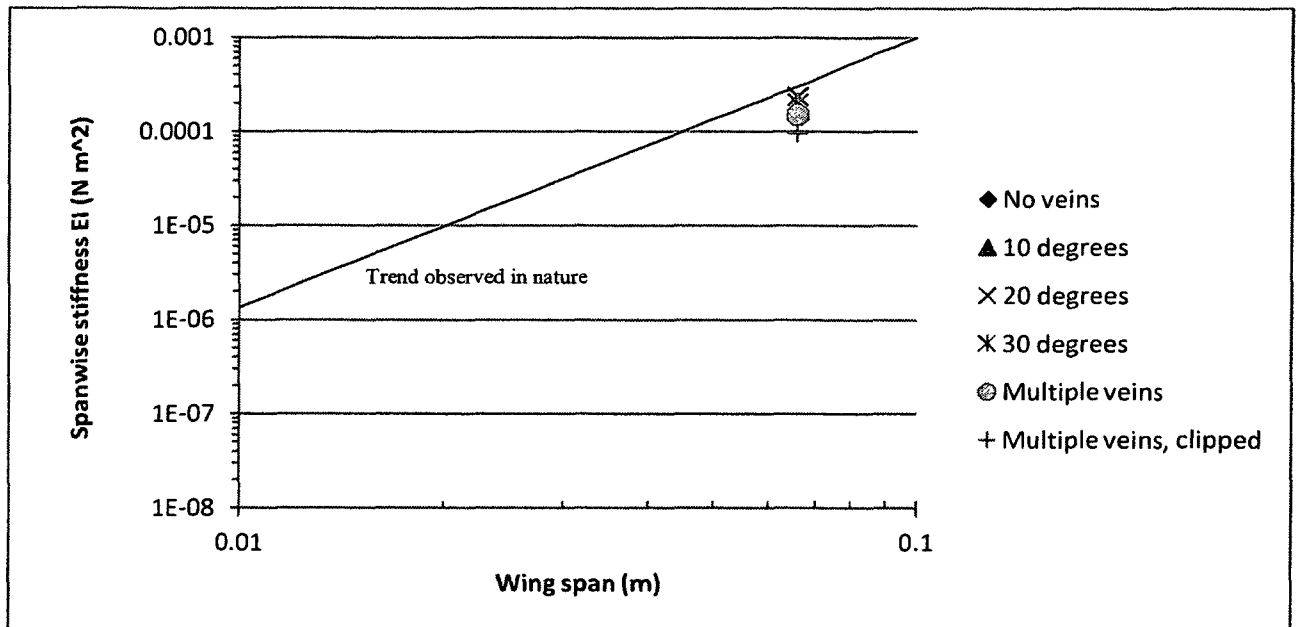


Figure 10-42. Spanwise stiffness versus wing span for 3-D printed wing prototypes, showing trendline observed in nature (Combes & Daniel, 2003)

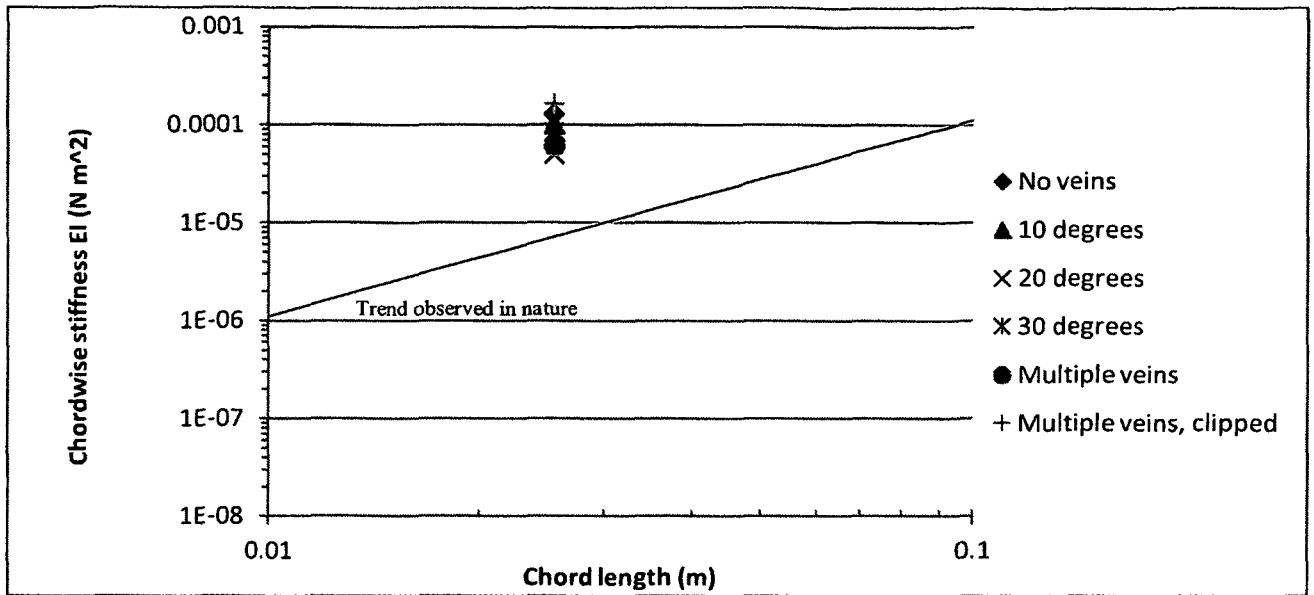


Figure 10-43. Chordwise stiffness versus chord length for 3-D printed wing prototypes, showing trendline observed in nature (Combes & Daniel, 2003)

The study by Combes and Daniel (2008) also showed that spanwise stiffness is 1-2 orders of magnitude larger than the chordwise flexural stiffness. A comparison of the spanwise and chordwise stiffness is shown for each prototype wing type in Figure 10-44. Spanwise stiffness is highest for wings with a vein angle of 20°, while also having the lowest chordwise stiffness. It is to be expected that as spanwise stiffness increases, the chordwise stiffness decreases, with smaller vein angles contributing to a higher spanwise stiffness. As shown in section 9.1.7.1, wings with vein angles of 20° and 30° produce the highest overall lift performance, which suggests that a higher spanwise stiffness produces higher lift.

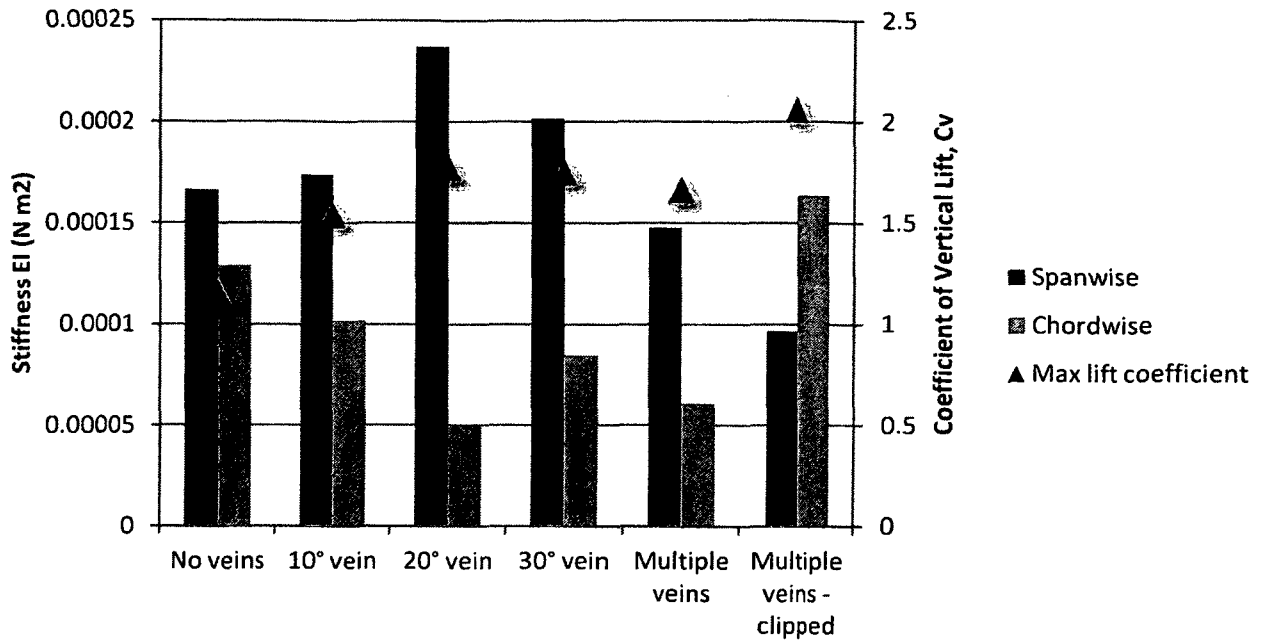


Figure 10-44. Comparison of chordwise and spanwise stiffness for each wing design. Maximum vertical lift coefficient is also shown for each wing design

The bending force was also applied dorsally (from the upper surface) in order to compare the bending stiffness in both the upward and downward directions. It was hypothesized that the membrane on the lower surface of the wing may shift neutral axis of wings, resulting in a lower downward bending stiffness similar to “peanut” shaped leading edge veins found in insect wings shown in Figure 10-45.

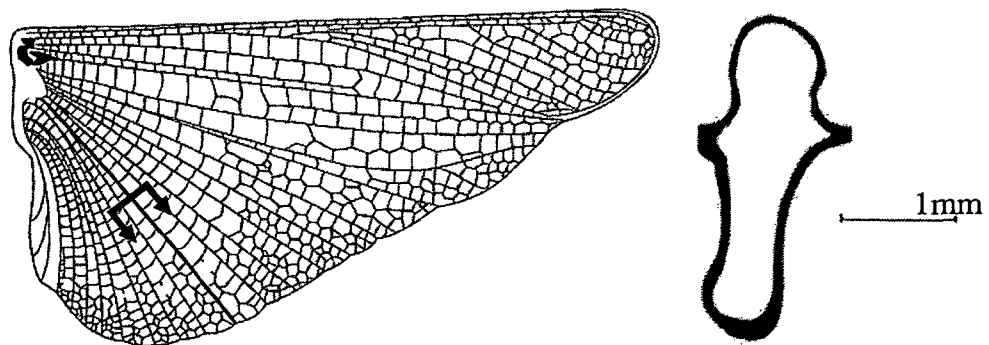


Figure 10-45. Cross sectional view of a locust wing vein, which is more resistant to upward bending than downward bending (Herbert, Young, Smith, Wootton, & Evans, 2000)

As shown in Figure 10-46, wings with no veins and wings with a vein at a 10° angle the bending stiffness in the upward and downward direction is not significantly affected by the membrane. This is likely because the membrane is very flexible and does not carry a significant portion of the bending loads at small deflections.

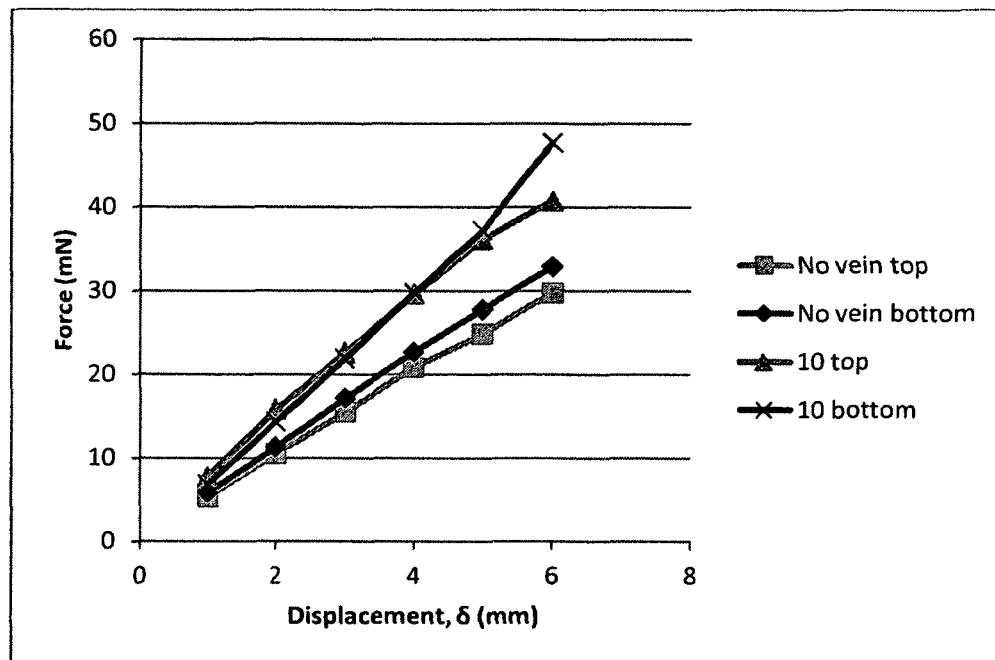


Figure 10-46. Comparison of upward and downward bending stiffness

10.3 Conclusions

The spin testing carried out in this chapter showed that 3-D printing flapping wing prototypes show promise for flapping MAV applications. The wings produced vertical lift coefficients that matched or exceeded that of real insect wings. The testing also allowed for a comparison of different wing designs, such as vein geometry, surface roughness, camber, and wing size. It was shown that wings with veins at 20° and 30° produced higher lift than other vein geometries, likely due to their relatively spanwise stiffness and lower chordwise stiffness. Surface roughness also had a significant effect on lift performance, particularly at high angles of attack. Wings with a rough surface texture

produced higher coefficients of vertical lift. Wing camber also produced higher lift at high angles of attack.

While the spin testing allowed for a quantitative analysis of different wing designs, without measurement of drag force, an evaluation of the overall net aerodynamic performance of the 3-D printed wings cannot yet be made. This, however, should be explored in future testing. Furthermore, spin testing does not fully represent the aerodynamics of a flapping wing in flight, nor does it account for the dynamic conditions of the wing during flapping flight, such as inertial deformations and wing durability. Flapping tests should be performed using a flapping apparatus to more accurately simulate these flight conditions and further evaluate each wing's aerodynamic and structural performance. Furthermore, flow visualization techniques using dye flow or particle image velocimetry (PIV) should be employed to gain a better understanding of how different wing designs affect the air flow during spinning and flapping.

Stiffness measurements performed on the wings showed that the spanwise stiffness of the wings follows the trend seen in many insects; however, chordwise stiffness was much higher than that of insect wings and may have a negative impact on aerodynamic efficiency. This can be remedied by printing a thinner medial vein, or by adding curvature to the median vein similar to insect wings.

11 Conclusions and Recommendations

The aim of this research was to develop a fabrication process for flapping MAV wings that can produce prototypes in a fast, accurate, low-cost, and repeatable manner in order to accelerate the rate of learning in the field of flapping-wing MAV design in order to more rapidly understand the underlying principles of flight at this scale. A review of the current fabrication processes used for producing MAV components showed that rapid prototyping technologies show promise for the fabrication of MAV components. Through the use of the RepRap Mendel open-source fused-deposition modeling (FDM) rapid prototyping machine, wing prototypes of various sizes, shapes, and configurations could be designed and fabricated in a matter of minutes with very little manual labour. Furthermore, both the capital cost and operating and material costs associated with this process are very low. However, there are improvements that can be made to the design cycle and the fabrication process to achieve parts with better quality more efficiently. Recommendations for improving the fabrication process are given in section 11.1.

Testing of the aerodynamic performance of both real locust wings and the 3-D printed wing prototypes was performed through axial spin testing. This testing allowed for a quantitative comparison between real insect wings and artificial wings, as well as between different wing configurations such as vein pattern. Bending stiffness measurements were also performed in order to compare the properties of the 3-D printed wings with trends found in nature. The significant observations and conclusions from this testing are given in section 11.2.

While the research presented in this thesis provide insight into the design and fabrication of flapping MAVs, and there remains much to learn about the underlying principles of flapping-wings and how to apply these to functional MAVs. Recommendations for further research are given in section 11.3. Through this research, contributions have been made to the field of MAV flapping wing design and fabrication, and these are described in section 11.4.

11.1 Manufacturing process

The use of the RepRap Mendel fused-deposition modeling 3-D printer has proven itself as a useful tool for rapid and low-cost fabrication of flapping wings. Used in conjunction with the OpenSCAD script-based modeling program, wing models with varying parameters can be designed and fabricated very quickly. As a result, the total design, fabrication and testing cycle can be accomplished in less than an hour. This rapid design and fabrication process achieves the primary goal of this research: to develop a fabrication process that will accelerate the evolution of flapping wing design in a low-cost manner. However, potential improvements to this design and fabrication process are discussed below.

11.1.1 Overall process

The process for fabricating wings presented in this thesis allowed for the rapid fabrication of wing prototypes. While the FDM process cannot produce parts with features smaller than approximately 1 mm (0.04 in), the wings do not necessarily require a higher level of detail than what is possible with the current process in order to achieve the desired performance.

One of the most significant advantages to using rapid prototyping for fabricating wing prototypes was that very little manual labour was required. However, the wings needed to be manually cut from the membrane material after being printed. In order to further automate the manufacturing process, a laser mounted to the extruder assembly could be used automatically cut the wings from membrane material. This, however, would significantly increase the weight of the extruder assembly, increase the system cost, and present a safety hazard due to laser radiation.

The methods used in this research segregated each step of the design and fabrication process, which consisted of part design, conversion to machine code (G-code), upload to the printer software, and printing of the part. The overall process could be streamlined by integrating the part design, g-code generation, and printing process into one software package. Furthermore, a dedicated program for printing wings should be developed, potentially leveraging existing open-source software. This would eliminate the issues faced with printing thin features using G-code generating software such as Skeinforge, which limits the minimum vein thickness to approximately twice the deposited filament diameter.

The overall design process may be further improved by completely closing the design cycle. For example, a wing design could be printed directly from an analytical or finite element model and subsequently tested either structurally or aerodynamically. The results from this testing may be input back into the model and an optimized wing design can be automatically generated and printed. The wing design can then more quickly converge, or *evolve*, towards a design that meets the design requirements.

11.1.2 Hardware

The current RepRap Mendel configuration was adequate for printing relatively simple flapping-wing prototypes; however there are several improvements to the printer hardware that can be made. First, a reduction in nozzle diameter would increase part resolution and allow thinner veins to be printed. As a result, the stiffness distribution in the wing may be more precisely tailored. Next, spin testing of wings fabricated from the same batch showed that the repeatability of the fabrication process was good, but could be improved. Better accuracy and repeatability may be achieved by modifying each axis' drive system such that each axis has a higher stepper motor resolution (i.e. higher number of motor steps per distance of travel).

Mechanical adjustment of both the z-axis end stop height and the build platform was tedious and difficult to achieve precise and accurate positions. The addition of an electronic range finder for precisely and accurately determining the z-axis position is recommended. The measured distance can be sent to the graphical user interface (GUI) through the motherboard in order to adjust the extruder-platform gap, and thus the z-axis home position, through the user interface.

Process efficiency may be gained by performing a thorough analysis of the extrusion process in order to optimize the extruder design. This would reduce power consumption, provide more efficient melting of the filament within the extruder, reduce pre-heating time, and improve reliability.

Finally, the addition of multiple extruders to the 3-D printer would allow wings and other components to be fabricated from materials with different mechanical properties. For

example, the leading edge may be printed from a high stiffness material, while the medial vein and radial veins may be printed from a more flexible material.

11.1.3 Materials

Acrylonitrile butadiene styrene (ABS) plastic was the primary vein material used in this research, since it showed good reliability in the printing process, while offering suitable material properties for MAV applications, such as stiffness and durability. The ABS thermoplastic also fused well with the polyvinylidene chloride (PVDC) membrane material. This fusion process was the key to fabricating lightweight and flexible wing prototypes with minimal labour. The PVDC film demonstrates excellent flexibility and durability in a thin and lightweight film. However, the film used in this research is intended for use as a consumer “cling-wrap”, and the static cling nature of the film often made it difficult to work with. Alternate forms of this film material should be investigated. Furthermore, alternative flexible membrane films should also be tested for compatibility with the 3-D printing process.

The use of the biodegradable thermoplastics is attractive for MAV applications, since these aircraft are intended to be expendable. Biodegradable materials would decrease the environmental impact of these aircraft. While the thermoplastic polylactic acid (PLA) was tested in this research with good reliability as a material for 3-D printing using FDM, it did not fuse well to the PVDC membrane material and was therefore not used in any tested wing prototypes. Investigation into other biodegradable or more environmentally friendly materials is recommended. Furthermore, investigation into the use of PLA with alternate membrane materials is recommended.

The addition of soluble support material extrusion capabilities on the RepRap may be of benefit for printing the fuselage or other components of the MAV; however, soluble support material is not strictly necessary for the fabrication of wings. While a soluble support material may allow for camber and/or twist to be incorporated into the wings during printing, these features may be more effectively produced by heating the wing past the vein material's glass transition temperature and forming the wing into the desired shape.

11.1.4 Alternative manufacturing processes

While this research focused on the use of fused deposition modeling for the fabrication of MAV wings, other rapid prototyping technologies should be investigated. While more expensive, photopolymer-based processes can achieve very high part resolutions and could allow for highly tailored wing structures with fine details that are not possible with the FDM process. The laminated object manufacturing (LOM) process may also be well-suited for fabricating thin wings and components quickly and affordably, since only a few layers of material would be required. The use high-strength and low density polymer films and composites may be possible. Each layer of composite material could be oriented as required to tailor strength and stiffness. Furthermore, layers of different materials may be possible, such as conducting outer layers and a piezoelectric inner layer such as polyvinylidene fluoride (PVDF), or a stiff outer wing frame with a continuous flexible inner membrane.

11.2 Wing testing

The primary objective of this research was to develop a fabrication process that would allow wing prototypes to be quickly fabricated and testing. This objective was achieved

by using the RepRap Mendel to quickly print various wing designs in order to test the performance of wing prototypes versus real insect wings, and to compare parametric design changes. The aerodynamic performance of the various wing designs were assessed through axial spin testing, which simulated the downstroke of a typical flapping cycle. Real locust wings were also tested to serve as a basis for comparison. Aerodynamic performance was evaluated based on coefficient of vertical lift, a dimensionless parameter that allows wings of different sizes to be compared.

Wings were tested at a range of rotational speeds, corresponding to different Reynolds numbers. Results showed that the vertical lift coefficient showed no change over a range of Reynolds numbers between 4,000 and 10,000. However, wings with surface roughness showed a 30% increase in maximum vertical lift coefficient at an angle of attack of 80° over the same Reynolds number range, while smooth wings at the same angle of attack showed no change in lift coefficient. This suggests that roughness plays a more significant role in lift generation at high angles of attack, and this is dependent on Reynolds number.

Tests on wings with different radial vein angles showed that wings with veins at 20° and 30° showed the highest peak vertical lift coefficients. In fact, the peak lift coefficients exceed those of the real locust wings. The locust wings, however, produced higher lift at angles of attack below 40° , while the 3-D printed wings sustained high lift at angles of attack between 40° and 100° . This is likely due to the naturally cambered shape of the locust wings. The 3-D printed wings generally only produce camber due to air loads are higher angles of attack, and were flat at low angles of attack. Wings with a single vein at 20° showed the best overall performance, with high lift throughout the range of angles of

attack. Wings with no veins generally performed poorly compared to the other wing designs. The vertical lift coefficient values and trends compared well with those given in literature for other flying insects, suggesting that the 3-D printed wings show promise for flapping wing MAVs.

Comparison of vertical lift coefficients between a single wing and a pair of wings generally showed a loss in lift of approximately 20% when spun as a pair. However, artificial wings with no radial veins showed higher lift coefficients when spun as a pair. This may suggest that the highly flexible membrane of these wings is less susceptible, or even benefits from, turbulent wing wake; or, that the flexible wing membrane produces less severe wing wake than the stiffer wings with radial veins. This observation is based only upon one data set, and further testing is required to verify these observations.

Wings with camber produced higher lift than wings without camber, as expected. However, the increase in lift came only at angles of attack greater than 30° . As previously mentioned, the camber is induced only at higher angles of attack upon deformation due to air loads, and therefore the wings do not benefit from camber at low angles of attack since the wing is flat. The most significant increase in lift was observed for wings with multiple veins, where the radial veins were clipped at the root to allow them to hinge and promote an “umbrella effect” of the wing. This wing produce a peak vertical lift coefficient above 2.0, while maintaining a lift coefficient above 1.0 even at a 100° angle of attack. The high flexibility of this wing allowed it to generate a large camber and thus produce high lift. However, while not measured, this wing also likely experienced very high drag.

Roughness also played a role in lift generation. High lift coefficients were measured on wings with veins on the upper surface rather than the lower surface, particularly at high angles of attack, as expected. This means that the 3-D printing process inherently adds an aerodynamic benefit to the wing by printing the veins on the upper surface of the membrane. Measurements of drag force should be conducted to confirm whether roughness on the bottom surface of the wing affects drag and efficiency of the wing.

Wings printed at a smaller scale to those previously tested showed the same lift distribution over the range of angles of attack, and produced similar vertical lift coefficients. This suggests that the testing method is not affected by wing size.

Flexural stiffness measurements performed on the wings showed that the spanwise wing stiffness correlates well with trends found in nature; however, the chordwise stiffness of all wings was found to be much higher than in nature. Stiffness measurements also showed that the wings with the highest lift generation also had the highest spanwise stiffness, as well as the highest ratio between spanwise and chordwise stiffness. This agrees well with the literature, in that spanwise stiffness and chordwise flexibility is important in flapping wings.

Without a measurement of drag force, a comparison of the overall net aerodynamic performance of the artificial wings versus real locust wings cannot be made. This, however, should be explored in future testing. Furthermore, spin testing does not fully represent the aerodynamics of a flapping wing in flight, nor does it account for the dynamic conditions of the wing during flapping flight, such as inertial deformations and wing durability. Flapping tests should be performed using a flapping apparatus to more

accurately simulate these flight conditions and further evaluate each wing's aerodynamic and structural performance. Further testing of the wings' structural properties is also recommended, including determination the material and geometric properties of the wings.

11.3 Recommendations for further research

In the long term, further research into alternative materials, including biodegradable polymers, should be explored. Furthermore, other low-cost rapid prototyping methods should be investigated. The integration of smart materials such as piezoelectric materials for energy harvesting, sensing, and/or actuation may allow for improvement upon nature's design. This may include actively changing the wing's stiffness for modification of flapping frequency in order to provide stability and control, or for active deployment of wing camber during the downstroke and retraction during the upstroke. Finally, investigation into the suitability of rapid prototyping for other MAV components such as fuselage and even electronic components should be explored.

12 Contributions

The aim of this research was to lay a foundation for future micro air vehicle (MAV) research by identifying and developing a process for MAV prototype development, while at the same time gaining insight into the design of flapping wings. Overall, this goal has been met through the application of the open-source RepRap Mendel fused-deposition modeling (FDM) rapid prototyping machine. This unique approach to MAV wing manufacturing has resulted in a low-cost process that can be used to rapidly manufacture customized wing prototypes that show promising aerodynamic performance as compared to real insect wings. By using this process, wing designs can be more quickly evaluated and convergence upon the optimal design can be achieved sooner. It has been demonstrated that a prototype design cycle, including manufacturing and testing, can be completed in as little as one hour. The use of this process will facilitate faster and more efficient study of not only MAV wings, but other components as well.

As part of this fabrication process, a novel method for fusing the vein and membrane materials has also been presented. This film-filament fusion process produces durable, flexible, and lightweight wings, while significantly reducing manual labour requirements and eliminating the need for additional adhesives.

Through the testing of the fabricated wings, this thesis has also contributed knowledge on the principles of flapping wing design. These contributions include further understanding on the role of wing vein orientation, wing camber, and surface roughness on the wing's aerodynamic performance. Axial spin tests showed that radial veins at 20-30° from the

leading edge generate higher lift than other vein angles, while camber and surface roughness can further increase lift, particularly at high angles of attack.

This work has been presented to a range of audiences in various forums, such as conferences and seminars in Canada and the United States:

- 1) Unmanned Systems Canada conference; Montreal, Quebec, 2010
- 2) Canadian Aeronautics and Space Institute AERO'11 conference; Montreal, Quebec, 2011
- 3) Institute for Engineering and Technology (IET) Present Around the World Competition – Regional Final; Ottawa, Ontario, 2011
- 4) Institute for Engineering and Technology (IET) Present Around the World Competition – Americas Final; Boston, Massachusetts, 2011
- 5) Department of Mechanical and Aerospace Engineering Seminar Series; Carleton University, Ottawa, Ontario, 2011.

In conclusion, the capabilities of current flapping and non-flapping wing MAVs do not yet have sufficient capabilities to perform useful missions. This progress is limited both by technological limitations in the size and weight of power sources and electronic hardware, but also by our lack of a complete understanding of the principles of flight at this scale. However, it can be expected that hardware will continue to decrease in size, while research such as that presented in this thesis will continue to advance our understanding of MAV design and fabrication towards the ultimate goal of a practical, low cost MAV platform.

References

- ActiveKB Knowledge Management System. (n.d.). *Objet General Purpose – FullCure 720*. Retrieved November 6, 2011, from Stereolithography.com website:
<http://knowledge.stereolithography.com/activekb/questions/121/Objet+General+Purpose+%96+FullCure+720+>
- Advanced Model of World's Smallest Flying Microrobot from Epson*. (2004, August 22). Retrieved October 22, 2011, from PhysOrg.com: <http://www.physorg.com/news888.html>
- Aerovironment, Inc. (2011). *Nano Hummingbird*. Retrieved April 25, 2011, from Aerovironment Inc. Website: <http://www.avinc.com/nano>
- Aerovironment Inc. (2011a). *AeroVironment Develops World's First Fully Operational Life-Size Hummingbird-Like Unmanned Aircraft for DARPA*. Retrieved October 23, 2011, from Aerovironment Website:
http://www.avinc.com/resources/press_release/aerovironment_develops_worlds_first_fully_operational_life-size_hummingbird
- Aerovironment Inc. (2011b). *UAS Advanced Development: Wasp*. Retrieved October 3, 2011, from Aerovironment Inc. Website: <http://www.avinc.com/uas/adc/wasp/>
- Aerovironment Inc. (2011c). *UAS Advanced Development: Hornet*. Retrieved October 3, 2011, from Aerovironment Website: <http://www.avinc.com/uas/adc/hornet/>
- Aerovironment Inc. (2010). Retrieved October 14, 2010, from Aerovironment Inc. Website:
http://www.avinc.com/img/media_gallery/UAS_Raven_prodshot_lg.jpg
- Aerovironment Inc. (2009). *Press Release: DARPA Awards AeroVironment Phase II Contract Extension for Nano Air Vehicle Development Program*. Retrieved October 22, 2011, from Aerovironment Website:
<http://www.avinc.com/downloads/NAVPRLongDARPAV4.doc.pdf>
- Aerovironment Inc. (2008). *USAF Approves BATMAV System with AeroVironment's Wasp III Micro Air Vehicle for Full Rate Production*. Retrieved July 27, 2009, from
http://www.avinc.com/resources/press_release/usaf_approves_batmav_system_with_avinc_wasp
- AFRL Air Vehicles Directorate. (2010, July 22). *Micro Air Vehicle Integration and Application Research Institute*. Retrieved October 30, 2011, from Wright-Patterson Air Force Base website:
<http://www.wpafb.af.mil/library/factsheets/factsheet.asp?id=17006>
- Ahn, S.-H., Montero, M., Odell, D., Roundy, S., & Wright, P. K. (2002). Anisotropic Material Properties of Fused Deposition Modeling ABS. *Rapid Prototyping*, 8 (4), 248-247.
- Arduino. (2011). Retrieved from Arduino website: <http://www.arduino.cc/>
- Astrobiology Magazine. (2009, February 13). *Entomopter: Extreme Explorer's Hall of Fame*. (H. Mastos, Editor) Retrieved October 30, 2011, from Astrobiology Magazine website:
<http://www.astrobio.net/pressrelease/271/entomopter-extreme-explorers-hall-of-fame>

- Bijlmakers, H. (2009). *Schistocerca gregaria* (Forsk.). Retrieved November 28, 2011, from Insect pests of cereals in Ethiopia: http://ethiopia.ipm-info.org/insect_pests_ethiopia/Schistocerca_gregaria.htm
- Bilodeau, P.-R., Wong, F. C. (2011). Extreme Agility Micro Aerial Vehicle - Control of hovering maneuvers for a mini-aerial vehicle with an onboard autopilot system. *Technical Report TR 2010-144*, Defence Research and Development Canada - Valcartier
- Bumiller, E., & Shanker, T. (2011, June 19). *War Evolves With Drones, Some Tiny as Bugs*. Retrieved from New York Times website: http://www.nytimes.com/2011/06/20/world/20drones.html?_r=1
- California Institute of Technology. (2001). *MicroBat*. Retrieved October 22, 2011, from Caltech Micromachining Laboratory website: <http://touch.caltech.edu/research/bat/bat.htm>
- Combes, S. A., & Daniel, T. L. (2003). Flexural stiffness in insect wings I. Scaling and the influence of wing venation. *Journal of Experimental Biology*, 206, 2979-2987.
- Combes, S. A., & Daniel, T. L. (2003). Into thin air: contributions of aerodynamic and inertial-elastic forces to wing bending in the hawkmoth *Manduca sexta*. *Journal of Experimental Biology*, 206, 2999-3006.
- Cooper, K. G. (2001). *Rapid Prototyping Technology*. New York: Marcel Dekker, Inc.
- CustomPartNet. (2009). *Manufacturing Cost Estimation*. Retrieved August 17, 2009, from CustomPartNet web site: www.custompartnet.com/
- De Clercq, K., de Kat, R., Remes, B., van Oudheusden, B., & Bijl, H. (2009). Aerodynamic Experiments on DelFly II: Unsteady Lift Enhancement. *International Journal of Micro Air Vehicles*, 1 (4), 255-262.
- de Croon, G. C., de Weerd, E., de Wagter, C., & Remes, B. D. (2011). The appearance variation cue for obstacle avoidance. *IEEE Transactions on Robotics*
- de Croon, G., de Clercq, K., Ruijsink, R., Remes, B., & de Wagter, C. (2009). Design, aerodynamics, and vision-based control of the DelFly. *International Journal of Micro Air Vehicles*, 1 (2), 71-97.
- Defense Advanced Research Projects Agency. (n.d.). *Nano Air Vehicle (NAV)*. Retrieved October 22, 2011, from DARPA Defense Sciences Office website: [http://www.darpa.mil/Our_Work/DSO/Programs/Nano_Air_Vehicle_\(NAV\).aspx](http://www.darpa.mil/Our_Work/DSO/Programs/Nano_Air_Vehicle_(NAV).aspx)
- Defence Research and Development Canada (2009). Flapping wing aerodynamics for insect-sized drones. *Soldier Systems Vision and Future Capabilities Workshop*. Gatineau.
- DeLaurier, J. D. (1999). The Development and Testing of a Full-Scale Piloted Ornithopter. *Canadian Aeronautics and Space Journal*, 45 (2) 72-82.
- DiLeo, C., & Deng, X. (2009). Design of and Experiments on a Dragonfly-Inspired Robot. *Advanced Robotics*, 23, 1003-1021.
- Ellington, C. P. (1999). The Novel Aerodynamics of Insect Flight: Applications to Micro-Air Vehicles. *Journal of Experimental Biology*, 202, 3439-3448.
- Ellsworth Adhesives. (2010). *Dymax Ultra Light-Weld 3099 UV Curing Adhesive Clear*. Retrieved November 27, 2011, from Ellsworth Adhesives web site: <http://www.ellsworth.com/display/productdetail.html?productid=2192&Tab=Vendors>

- Ettinger, S., Nechyba, M., Ifju, P., & Waszak, M. (2002). Vision-guided flight stability and control for micro air vehicles. *IEEE/RSJ International Conference on Intelligent Robots and Systems*, 3, pp. 2134-2140.
- Fleming CNC. (2010). Retrieved from Fleming CNC website: <http://flemingcnc.com/>
- Free Software Foundation. (2010, September 8). *GNU General Public License, version 2*. Retrieved August 6, 2011, from GNU Operating System: <http://www.gnu.org/licenses/old-licenses/gpl-2.0.html>
- Grasmeyer, J. M., & Keennon, M. T. (2001). Development of the Black Widow Micro Air Vehicle. *American Institute of Aeronautics and Astronautics (AIAA)* .
- Harvard University. (2011). Retrieved from Harvard Microrobotics Laboratory: <http://micro.seas.harvard.edu/>
- Heathcote, S., Wang, Z., & Gursul, I. (2008). Effect of spanwise flexibility on flapping wing propulsion. *Journal of Fluids and Structures* , 24, 183–199.
- Herbert, R. C., Young, P., Smith, C. W., Wootton, R. J., & Evans, K. E. (2000). The Hund Wing of the Desert Locust (*Schistocera Gregaria* Forskal) III. A Finite Element Analysis of a Deployable Structure. *Journal of Experimental Biology* , 203, 2945-2955.
- Hodgson, G. (2011) *Wade's Geared Extruder – Visual Instructions*. Retrieved December 10, 2011, from Gary Hodgson's web log: <http://garyhodgson.com/reprap/>
- Hornung, J (2005). *Wanderheuschrecke-01.jpg*. Retrieved January 14, 2012, from Wikipedia: <http://pl.wikipedia.org/wiki/Locusta>
- Human Powered Ornithopter Project (2010). Retrieved January 14, 2012, from <http://hpo.ornithopter.net>
- Ifju, P. G., Jenkins, D. A., & Martinex, L. (2001). Composite Materials for Micro Air Vehicles. *Proc. SAMPE Annual Conference*. Long Beach.
- Ifju, P. G., Jenkins, D. A., Ettinger, S., Lian, Y., Shyy, W., & Waszak, M. R. (2002). *Flexible-Wing-Based Micro Air Vehicles*. American Institute of Aeronautics and Astronautics.
- Jensen, M. (1956). Biology and physics of locust flight. III. The aerodynamics of locust flight. *Philosophical Transactions of the Royal Society of London B*, 245, 511-552.
- Jensen, M., & Weis-Fogh, T. (1962). Biology and physics of locust flight. V. Strength and elasticity of locust cuticle. *Philosophical Transactions of the Royal Society of London B*, 245, 137-169.
- Jones, R., Haufe, P., Sells, E., Irvani, P., Olliver, V., Palmer, C., et al. (2011). RepRap - the replicating rapid prototyper. *Robotica*, 29, 177-191.
- Jongerius, S., & Lentink, D. (2010). Structural Analysis of a Dragonfly Wing. *Journal of Experimental Mechanics* , 50 (9), 1323-1334.
- Karpelson, M., Whitney, J. P., Wei, G.-Y., & Wood, R. J. (2010). Energetics of Flapping-Wing Robotic Insects: Towards Autonomous Hovering Flight. *IEE/RSJ International Conference on Intelligent Robots and Systems*, (pp. 1630-1637). Taipei.

- Kellogg, J., Bovais, C., Dahlburg, J., Foch, R., Gardner, J., Gordon, D., et al. (2001). The NRL MITE Air Vehicle. *Proceedings of Bristol RPV/AUV Systems Conference*. Bristol, UK.
- Kroo, I., & Prinz, F. B. (2009). *The Mesicopter: A Meso-scale Flight Vehicle*. NIAC Phase I Final Report, Stanford University.
- Lentink, D., Jongerius, S. R., & Bradshaw, N. L. (2009). The scalable Design of Flapping Micro-Air Vehicles Inspired by Insect Flight. In D. Floreano, J.-C. Zufferey, & M. V. Srinivasan, *Flying Insects and Robotics* (pp. 185-205). Berlin Heidelberg: Springer-Verlag.
- Lesage, F., Hamel, N., Huang, X., Yuan, W., Khalid, M., Zdunich, P. (2008). Initial investigation on the aerodynamic performance of flapping wings for nano air vehicles. *Technical Memorandum TM 2007-550*, Defence Research and Development Canada - Valcartier.
- Liou, F. W. (2008). *Rapid prototyping and engineering applications: a toolbox for prototype development*. CRC Press, Taylor & Francis Group.
- Lung-Jieh, Y. (2007). Flapping MAV micro aerial vehicle with PVDF-parylene composite skin. *Journal of Aeronautics, Astronautics and Aviation*, 39 (3), 195-202.
- MakerBot Industries. (2011). Retrieved from MakerBot Industries website: www.makerbot.com
- Marks, P. (2011, August 01). *3D printing: The world's first printed plane*. (Reed Business Information Ltd.) Retrieved August 2, 2011, from New Scientist: Tech: <http://www.newscientist.com/article/dn20737-3d-printing-the-worlds-first-printed-plane.html>
- McIver, J. (2003). *Cessa Skyhawk II/100 Performance Assessment*. Temporal Images.
- Michelson, R. C. (2004). Novel approaches to miniature flight platforms. *Journal of Aerospace Engineering, Proceedings of the Institution of Mechanical Engineers Vol. 218 Part G*.
- Michelson, R. C., & Naqvi, M. A. (2003). Beyond Biologically Inspired Insect Flight. *RTO-AVT von Karman Institute for Fluid Dynamics Lecture Series*.
- Michelson, R. C., & Naqvi, M. A. (2003). Beyond Biologically Inspired Insect Flight. *RTO-AVT von Karman Institute for Fluid Dynamics Lecture Series*.
- Mols, B. (2005). Flapping micro plane watches where it goes. *Delft Outlook*.
- Morris, S. J., & Holden, M. (2000). Design of Micro Air Vehicles and Flight Test Validation. *Proceedings of the Fixed, Flapping and Rotary Wing Vehicles at Very Low Reynolds Numbers*, 153-176.
- Mortimer, G. (2010, August 15). *Prioria win Canadian defence contract with Maveric MAV*. Retrieved October 22, 2011, from sUAS News: <http://www.suasnews.com/2010/08/583/prioria-win-canadian-defence-contract-with-maveric-mav/>
- Mueller, T. J. (2006). Overview of Micro-Air-Vehicle Development. In T. J. Mueller, P. G. Ifju, & S. V. Shkarayev, *Introduction to the Design of Fixed-Wing Micro Air Vehicles* (pp. 1-38). Reston, Virginia: American Institute of Aeronautics and Astronautics, Inc.
- Muren, P. (2005). Retrieved October 22, 2011, from Proxflyer website: <http://www.proxflyer.com/>

- Murphy, J. T. (2008). *Experimental investigation of biomimetic wing configurations for Micro Air Vehicle applications*. M.Sc. Thesis, Iowa State University, Ames, Iowa.
- Murphy, J. T. (2008). *Experimental investigation of biomimetic wing configurations for Micro Air Vehicle applications*. M.Sc. Thesis, Iowa State University, Ames, Iowa.
- Nachtigall, W. (1981). Der Vorderflügel grosser Heuschrecken als Luftkraftezeuger. I. Modellmessungen zur aerodynamischen Wirkung unter schiedlicher Flügel profile. *Journal of Comparative Physiology*, 142. (pp. 127-135). [Locust wing models in parallel and rotating flow]
- Pines, D. J. (2006). Challenges Facing Future Micro-Air-Vehicle Development. *Journal of Aircraft*, 43 (2), 290-305.
- Pixelito: Even Lighter Helicopter*. (2004). Retrieved October 22, 2011, from Gizmodo: <http://gizmodo.com/019918/pixelito-even-lighter-helicopter>
- Pornsirak, T. N., Tai, Y., Nassef, H., & Ho, C. (2001). Titanium-alloy MEMS wing technology for a micro aerial vehicle application. *Sensors and Actuators A* 89 (2001) 95-103.
- Pornsirak, T. N., Tai, Y.-C., Ho, C.-M., & Keennon, M. (2001). Microbat: A Palm-Sized Electrically Powered Ornithopter. *NASA/JPL Workshop on Biomimetic Robotics*. Pasadena.
- Prioria Robotics Inc. (2011) *Maveric UAS*. Retrieved on 3 December 2011 from Prioria Robotics Inc. website: www.prioria.com
- Proto3000. (2008). *Polyjet advantages*. Retrieved from Proto3000 website: <http://www.proto3000.com/rapid-prototyping.aspx?topidcol=11>
- Prox Dynamics, Inc. (2009). Retrieved October 22, 2011, from Prox Dynamics Website: www.proxdynamics.com
- Rechtenwald, T., Krauß, H.-J., Pohle, D., & Schmidt, M. (2007). Small scale and micro featured functional prototypes generated by lasersintering of polyetheretherketone. *Micromachining Technology for Micro-Optics and Nano-Optics V and Microfabrication Process Technology XII*, 6462 (646203).
- RepRap.org. (2011). Retrieved from RepRap Wiki: <http://reprap.org>
- Richter, C., & Lipson, H. (2010). Hovering Flapping Flight of a 3D-Printed Mechanical Insect. *Alife XII Conference*. Odense, Denmark.
- RJM Rapid Prototyping. (n.d.). *Stereolithography*. Retrieved August 11, 2009, from RJM Rapid Prototyping Web Site: http://www.rjmrp.com/main/index.php?option=com_content&view=article&id=44:sla-process&catid=7:faqmain&Itemid=25
- Roos, W. (n.d.). *DelFly Micro*. Retrieved 10 30, 2011, from Delfly website: <http://www.delfly.nl/?site=DIII&menu=&lang=en>
- Schnackenburg, K. (2007). Towards better Artificial Insect Wings for Flow Visualization and Micro-Air Vehicles. *International Conference on Adaptive Structures and Technologies*. Ottawa, Canada.

- Sluis, F. (2001). *Using finite element method for the heat transfer analysis of a fused deposition 3-dimensional printer*. Report, Carleton University.
- Smith, C. W., Herbert, R., Wootton, R. J., & Evans, K. E. (2000). The Hind Wing of the Desert Locust (*Schistocerca Gregaria*) II. Mechanical Properties and Functioning of the Membrane. *Journal of Experimental Biology*, 203, 2933-2943.
- Stratasys, Inc. (2009). *Dimension 1200es Series: Product Specifications*. Retrieved August 11, 2009, from Dimension Printing Web Site: <http://www.dimensionprinting.com/3d-printers/printing-productspeccs1200series.aspx>
- Stratasys, Inc. (2009). *News Release: Dimension 3D Printing Group Introduces the uPrint(TM) Personal 3D Printer*. Retrieved August 11, 2009, from Stratasys, Inc. Web Site: <http://www.stratasys.com/investors.aspx?irp=news&nyo=0>
- TechZoneCommunications.com LLC. (n.d.). Retrieved from TechZoneCommunications.com website: <http://www.techzonecom.com/index.php>
- TNO. (n.d.). *Improved micro-stereo lithography: Faster and more accurate 3D printing*. Retrieved August 12, 2009, from TNO Web Site: http://www.tno.nl/downloads/TNO_micro_stereo_lithography.pdf
- Usherwood, J. R., & Ellington, C. P. (2002). The Aerodynamics of Revolving Wings; I. Model hawkmoth wings. *Journal of Experimental Biology* (205), 1547–1564.
- Usherwood, J. R., & Ellington, C. P. (2002a). The Aerodynamics of Revolving Wings II. Propeller force constants from mayfly to quail. *Journal of Experimental Biology*, 205, 1565-1576.
- Van de Rostyne, A. (2003, December 15). *6.9 grams flying robots*. Retrieved October 22, 2011, from RCGroups.com: <http://www.rcgroups.com/forums/showthread.php?t=179128>
- van Dijk, T. (2008). Born under a stereo microscope: Detective dragonfly. *Delft Outlook* (3), pp. 13-16.
- Wang, Z. J. (2005). Dissecting Insect Flight. *Annual Review of Fluid Mechanics*, 37, 183-210.
- Weis-Fogh, T. (1956). Biology and physics of locust flight II. Flight performance of the desert locust. *Philosophical Transactions of the Royal Society of London B*, 239, 459-510.
- Weis-Fogh, T. (1956a). Biology and physics of locust flight. IV. Notes on sensory mechanisms in locust flight. *Philosophical Transactions of the Royal Society of London B*, 239, 553-584.
- Weis-Fogh, T. (1964). Biology and physics of locust flight. VIII. Lift and metabolic rate of flying insects. *Journal of Experimental Biology*, 41, 257-271.
- Weis-Fogh, T. (1973). Quick estimates of flight fitness in hovering including novel mechanisms for lift production. *Journal of Experimental Biology*, 59, 169-230.
- Weis-Fogh, T., & Jenson, M. (1956). Biology and physics of locust flight. I. Basic principles in insect flight. A critical review. *Philosophical Transactions of the Royal Society of London B*, 239, 415-458.
- Wood, R. J. *Aerial, terrestrial, and aquatic microrobots*. Presentation, Harvard University, School of Engineering and Applied Sciences.

Wood, R. J. (2008). The First Takeoff of a Biologically Inspired At-Scale Robotic Insect. *IEEE Transactions on Robotics*, 24 (2), 341-347.

Wootton, R. J., Evans, K. E., Herbert, R., & Smith, C. W. (2000). The Hind Wing of the Desert Locust (*Schistocera Gregaria* Forskal) I. Functional Morphology and Mode of Operation. *Journal of Experimental Biology*, 203, 2921-2931.

Yang, L.-J. (2007). A Flapping MAV Micro Aerial Vehicle with PVDF-Parylene Composite Skin. *Journal of Aeronautics, Astronautics and Aviation*, 39 (3), 195-202.

Yang, L.-J., Hsu, C.-K., Ho, J.-Y., & Feng, C.-K. (2007). Flapping wings with PVDF sensors to modify the aerodynamic forces of a micro aerial vehicle. *Sensors and Actuators A*, 139, 95-103.

Zdunich, P., Bilyk, D., MacMaster, M., Leowen, D., DeLaurier, J., Kornbluh, R., et al. (2007). Development and Testing of the Mentor Flapping-Wing Micro Air Vehicle. *Journal of Aircraft*, 44 (5), 1701-1711.